

Kristian Mikkelsen

# Three-dimensional Experimental Investigation of Hydrodynamic Forces and Wake Interaction between Two Square Cylinders in Large-amplitude Oscillatory Flow

Master's thesis in Marine Technology

Supervisor: Trygve Kristiansen

June 2023



Kristian Mikkelsen

# **Three-dimensional Experimental Investigation of Hydrodynamic Forces and Wake Interaction between Two Square Cylinders in Large-amplitude Oscillatory Flow**

Master's thesis in Marine Technology  
Supervisor: Trygve Kristiansen  
June 2023

Norwegian University of Science and Technology  
Faculty of Engineering  
Department of Marine Technology



Norwegian University of  
Science and Technology





DEPARTMENT OF MARINE TECHNOLOGY

MASTER'S THESIS

---

**Three-dimensional Experimental  
Investigation of Hydrodynamic Forces  
and Wake Interaction between Two  
Square Cylinders in Large-amplitude  
Oscillatory Flow**

---

*Author:*  
Kristian Mikkelsen

June 2023

---

## Preface

This thesis is the finishing work of my five-year Master of Science degree in Marine Hydrodynamics. The specialization is part of the study of Marine Technology at the Department of Marine Technology (IMT) at the Norwegian University of Science and Technology (NTNU).

The thesis explores the hydrodynamic interaction loads between square 3D cylinders in forced harmonic oscillatory flow. Its motivation is directly tied to its industrial relevance, specifically a multi-modular PV concept developed by Equinor and Moss Maritime. The study holds significance, particularly in the context of multi-modular solar islands, where the hydrodynamic interaction between the pontoons in waves and currents is expected. The overarching objective is to leverage the available ocean space for sustainable green energy production. Solar energy possesses a large potential to make substantial contributions to the future energy portfolio. To ensure success, it is crucial to investigate the environmental loads that the structure will encounter.

This study builds upon the master's thesis by Reiten in 2022. The study has been a part of a multi-disciplinary collaborative effort between several master's and Ph.D. students studying multi-modular PV plants. Collaboration and knowledge sharing between the different group members have been emphasized. It is expected that the reader possesses a certain level of pre-existing knowledge about hydrodynamics, fluid mechanics, and data post-processing.

---

## Acknowledgements

The successful completion of this thesis has been made possible due to the invaluable contributions of several individuals. I would therefore like to extend my gratitude to the key collaborators and partners of my work.

I would first and foremost like to express my gratitude to my supervisor, Trygve Kristiansen. He was able to craft a stimulating and fulfilling task suited to my abilities. The thesis owes its successful completion to his dedication, extensive experience, and profound expertise on the topic of hydrodynamics. The standard achieved for the thesis would not have been possible without his invaluable guidance hours and email correspondence. Additionally, I would like to thank Erin Bachynski-Polić for her help with the Wadam model.

I would also like to express my appreciation to Trond Innset and Ole Erik Vinje who played a crucial role in cutting and manufacturing the plates and cylinders, which were essential components of our experiments. I am immensely grateful to Robert Opland and Terje Rosten for their invaluable support in setting up the experimental rig and instrumentation. Robert in particular has been a steadfast presence, offering assistance with, and overseeing the smooth execution of the experiments. Their collective efforts have significantly contributed to the success of our research endeavors.

Furthermore, I would like to express my gratitude to my lab partner and fellow master's student Petter Grudt Hals. Petter provided invaluable assistance during the post-processing and presentation stages of the data, further enhancing the overall quality of our findings. I am grateful for Petter's collaboration, dedication, and valuable contributions throughout this project as a sparring partner. The same is true for Vilde Solberg, who accompanied me during the staggered experiments. I would also like to thank my good friends and office partners for their support during the last year.

Lastly, I like to express my appreciation to the reviewers of my thesis. Their evaluation and feedback have greatly contributed to the refinement and overall quality of this work. I am grateful for their time and valuable input, which have enhanced the scholarly rigor of my research. A special thanks to Emilia O'Brien, who also helped with the presentation of my sketches.

---

## Abstract

The present work investigates hydrodynamic interaction forces and effects between three-dimensional square cylinders in a large Keulegan-Carpenter (KC) flow. This is primarily done experimentally, with some features from the potential flow solver Wadam. Two experiments spanning both the fall and spring semesters have been conducted to capture the effects of both tandem and staggered arrangements. Additionally, a mesh refinement analysis and numerical simulation have been performed using the Sesam suite.

The thesis is introduced with a brief description of its motivation, driven by the aspiration to explore the potentially far-reaching impact of green energy and offshore solar islands. A diligent effort is made to provide a comprehensive literature review despite the somewhat limited topic.

The experiments took place in Ladertanken, located at the Marine Technology Center in Trondheim. It is a narrow wave flume tank equipped with an actuator, allowing for the examination of models in oscillatory motion. A custom rig is designed to facilitate force measurements. This enables a detailed comparison between the forces exerted by the cylinders, allowing for a comprehensive assessment. In total, seven different configurations were tested in tandem across a range of KC numbers up until  $KC = 22$ . Staggered arrangement were tested for inflow angles between  $90^\circ$  and  $35^\circ$ . The experiments yielded substantial rig forces, which introduce uncertainty to the measurements. Consequently, significant attention was dedicated to synchronizing and subtracting the empty rig from the measurements. This enabled the isolation and acquisition of hydrodynamic damping and added mass forces exclusively attributed to the cylinders.

Numerical simulations have been performed on the same experimental cases to extract added mass coefficients from the potential flow solver. These coefficients are compared to their experimental counterparts, along with features from strip theory and DNV-RP-C205. Additionally, they were used in a modified KC dependent Morison inertial term to evaluate the applicability of the potential flow solver and to compare this inertial force with the experimental added mass forces.

These efforts showed clear KC number, inflow angle, and spacing ratio dependencies on the forces. The nondimensionalized results seemed largely independent of cylinder lengths when in tandem, with slightly more scatter for the smallest lengths. Unlike tandem configuration, staggered configuration showed a dependency on cylinder length and large stochasticity for higher frequencies. A load formulation based on a rewritten and nondimensionalized Morison equation with KC dependency was proposed. This model incorporates the simplified velocity reduction proposed by Kristiansen, but implements a continuous sine function on each half-cycle instead of a constant velocity reduction factor. While capturing the essence of the  $2\omega$  difference force, the model underestimates the reduced peaks. Furthermore, experimental results are compared with Hals' CFD results, providing recommendations to improve simulation strategies and enhance compatibility with the experiments.

Further investigations are needed to develop an accurate load formulation, warranting additional experiments and CFD simulations.



---

## Sammendrag

Dette arbeidet undersøker hydrodynamiske interaksjonskrefter og effekter mellom tredimensjonale kvadratiske sylindre i stor Keulegan-Carpenter-strøm (KC). Dette gjøres primært eksperimentelt, med noen innslag fra den potensielle strømningsløseren Wadam. To eksperimenter som spenner over både høst- og våsemesteret er utført for å fange effektene av både tandem- og forskjøvede konfigurasjoner. I tillegg er det utført en mesh-analyse og numerisk simulering ved bruk av Sesam-pakken.

Opgaven introduseres med en kort beskrivelse av motivasjonen, drevet av ambisjonen om å utforske den potensielle vidtrekkende virkningen av grønn energi og offshore solarøyer. Det gjøres en iherdig innsats for å gi en omfattende litteraturgjennomgang til tross for det begrensede temaet.

Forsøkene fant sted i Ladertanken, som ligger ved Marinteknisk senter i Trondheim. Det er en smal bølgesjakt utstyrt med en aktuator, som gjør det mulig å undersøke modeller i oscillerende bevegelse. En spesialtilpasset rigg er designet for å lette kraftmålingene. Dette muliggjør en detaljert sammenligning og vurdering av kreftene som utøves av sylindrene. Totalt ble syv forskjellige modellkonfigurasjoner testet over en rekke KC-tall frem til  $KC = 22$ . Forskjøvet arrangement ble testet for vinkler mellom  $90^\circ$  og  $35^\circ$ . Eksperimentene gav betydelige riggkrefter, som introduserer usikkerhet til målingene. Følgelig er betydelig oppmerksomhet dedikert til å synkronisere og trekke den tomme riggen fra kraftmålingene. Dette muliggjorde isolering og anskaffelse av hydrodynamisk demping og tilleggsmasse som utelukkende tilskrives sylindrene.

Numeriske simuleringer er utført på de samme eksperimentelle tilfellene for å trekke ut massekoeffisienter fra den potensielle strømningsløseren. Disse koeffisientene sammenlignes med deres eksperimentelle motstykker, sammen med innslag fra stripeteori og DNV-RP-C205. I tillegg ble de brukt i en modifisert KC avhengig Morison treghetsledd for å evaluere anvendeligheten til den potensielle strømningsløseren, og for å sammenligne denne treghetskraften med de eksperimentelle tilleggsmasse kreftene.

Forsøkene viste tydelige KC-tall, innstrømningsvinkel og avstandsforholdsavhengigheter av kreftene. De ikke-dimensjonaliserte resultatene virket stort sett uavhengige av sylindrelengder i tandem, med litt mer spredning for de minste lengdene. I motsetning til tandemkonfigurasjon, viste forskjøvet konfigurasjon avhengighet av sylindrelengde og stor stokastisitet for høyere frekvenser. En lastformulering basert på en omskrevet og ikke-dimensjonalisert Morison-ligning med KC-avhengighet er foreslått. Modellen inkorporerer den forenklete hastighetsreduksjonen foreslått av Kristiansen, men implementerer en kontinuerlig sinusfunksjon på hver halvsyklus framfor en konstant hastighetsreduksjonsfaktor. Mens den fanger essensen av  $2\omega$  forskjellskraften, undervurderer modellen de reduserte toppene. Videre sammenlignes eksperimentelle resultater med Hals sine CFD-resultater, og gir anbefalinger for forbedrede simuleringstrategier og kompatibiliteten med eksperimentene.

Ytterligere undersøkelser er nødvendig for å utvikle en mer nøyaktig lastformulering, noe som nødvendiggjør ytterligere eksperimenter og CFD-simuleringer.

## List of Abbreviations

2D	Two dimensional
3D	Three dimensional
CFD	Computational Fluid Dynamics
DAQ	Data Acquisition
OF	OpenFOAM
PV	Photovoltaic
RES	Renewable Energy Source
WP	Wave probe
VIV	Vortex induced vibration

## List of Symbols

$\Delta F$	Force difference
$\eta$	Vertical position
$\eta_a$	Oscillatory motion amplitude
$\dot{\eta}$	Vertical velocity
$\ddot{\eta}$	Vertical acceleration
$\zeta_a$	Incident wave amplitude
$\nu$	Kinematic viscosity
$\rho$	Water density
$\omega$	Oscillation/harmonic frequency
$\theta$	Inflow angle
$A$	Added mass
$A_0$	Reference added mass
$a(t)$	Acceleration
$B$	Damping
$B_q$	Quadratic damping
$C_a$	Added mass coefficient
$C_b$	Damping coefficient
$C_D$	Drag coefficient
$C_M$	Inertia coefficient
$D$	Characteristic length (width)
$S$	Spacing between cylinders
$L$	Characteristic length (Length)
$m$	Mass
$U$	Total fluid inflow velocity
$u$	Fluid flow in x-direction
$w$	Fluid flow in z-direction
KC	Keulegan-Carpenter number
Re	Reynolds number
$T$	Oscillation period

# Table of Contents

<b>1</b>	<b>Introduction</b>	<b>1</b>
1.1	Preproject Work - TMR4520 . . . . .	1
1.2	Scope of Work . . . . .	2
1.3	Motivation . . . . .	3
1.4	Literature Review . . . . .	4
<b>2</b>	<b>Theory</b>	<b>9</b>
2.1	Dynamic Equilibrium . . . . .	9
2.2	Wave Excitation Forces . . . . .	10
2.3	Hydrodynamic Force . . . . .	11
2.4	Hydrodynamic Damping Forces . . . . .	13
2.5	Reynolds Number . . . . .	13
2.6	Keulegan-Carpenter Number . . . . .	14
2.7	Morison's Equation . . . . .	14
<b>3</b>	<b>Experimental Setup</b>	<b>17</b>
3.1	Facilities . . . . .	17
3.2	Apparatus and Equipment . . . . .	18
3.3	Test Configurations . . . . .	19
3.3.1	Tandem Arrangement . . . . .	20
3.3.2	Staggered Arrangement . . . . .	21
3.4	Hammer Tests . . . . .	21
3.5	Sources of Error . . . . .	24

<b>4</b>	<b>Experimental Post-Processing</b>	<b>26</b>
4.1	Locate KC Number . . . . .	26
4.2	Synchronization . . . . .	27
4.3	Rig and Acceleration Subtraction . . . . .	28
4.4	Band-Pass Filtering . . . . .	28
4.5	Harmonic Component Extraction . . . . .	30
4.6	Nondimensionalization . . . . .	30
<b>5</b>	<b>Potential Flow Analysis - Wadam</b>	<b>31</b>
5.1	Panel Model Setup . . . . .	31
5.2	Wadam Setup . . . . .	32
5.3	Mesh Refinement Analysis . . . . .	33
5.4	Added Mass . . . . .	34
5.5	Excitation Loads . . . . .	35
5.6	Presentation of Numerical Results . . . . .	35
<b>6</b>	<b>Results and Discussions</b>	<b>37</b>
6.1	Tandem Arrangement . . . . .	37
6.1.1	Case 1 . . . . .	37
6.1.2	Case 2 . . . . .	42
6.1.3	Experiments and Potential theory . . . . .	47
6.1.4	Higher Order Force Coefficients . . . . .	50
6.2	Staggered Arrangement . . . . .	53
6.2.1	$1\omega$ Force Components . . . . .	53
6.2.2	Higher Order Force Components . . . . .	55
6.2.3	Damping Forces - Staggered Arrangement . . . . .	57
6.3	A Discussion on $2\omega$ Forces . . . . .	59
6.4	Qualitative Comparison to 2D CFD . . . . .	62
6.5	Comparison to the Morison Equation . . . . .	65
6.6	Summarizing Comments and Load Formulation . . . . .	70
<b>7</b>	<b>Conclusions and Further Work</b>	<b>72</b>
7.1	Conclusions . . . . .	72

7.2 Further Work . . . . .	73
<b>References</b>	<b>76</b>
<b>Appendices</b>	<b>77</b>
<b>A DNV-RP-C205</b>	<b>77</b>
<b>B Force Plots and Results</b>	<b>78</b>
B.1 Harmonic Forces - Small and Medium . . . . .	78
B.2 Force Coefficients for Case 1 . . . . .	80
B.3 Force Coefficients for Case 2 . . . . .	81
B.4 Time Series - Case 1 ( $\frac{S}{D} = 1$ ) . . . . .	82
B.5 Time Series - Case 1 ( $\frac{S}{D} = 2$ ) . . . . .	83
B.6 Time Series - Case 1 ( $\frac{S}{D} = 3$ ) . . . . .	84
B.7 Time Series - Case 2 ( $\frac{S}{D} = 1$ ) . . . . .	85
B.8 Time Series - Case 2 ( $\frac{S}{D} = 2$ ) . . . . .	86
B.9 Time Series - Case 2 ( $\frac{S}{D} = 3$ ) . . . . .	87
<b>C Miscellaneous</b>	<b>88</b>
C.1 $1\omega$ Viscous Forces for Staggered flow . . . . .	88
C.2 Harmonic Forces - Case 3 . . . . .	89
C.3 Example of Velocity Reduction Factor Implementation . . . . .	90
<b>D Python Routines - Post-Processing</b>	<b>91</b>
D.1 Data Extraction from Wadam . . . . .	91
D.2 Synchronization . . . . .	95
D.3 Experimental Sub-routines . . . . .	96
D.4 Analyze Script for Tandem Arrangement . . . . .	98
D.5 Analyze Script for Staggered Arrangement . . . . .	104

# Introduction

This thesis is on the topic of hydrodynamic forces and interaction effects on three-dimensional (3D) cylinders in close proximity and in forced oscillation. The research primarily employs experimental methods, conducting two experiments to examine both tandem and staggered cylinder arrangements. Complementing the experimental findings, numerical results from Wadam are utilized to evaluate the accuracy of potential flow solvers. The experimental setup is specifically designed to investigate the influence of various parameters. Tandem configuration primarily deals with the KC number, spacing ratio ( $S/D$ ), and cylinder lengths ( $L$ ), while staggered configuration investigates the inflow angle ( $\theta$ ) effects. A primary objective has been to investigate the force's dependency on the KC number, which can be written as

$$KC = \frac{UT}{D} = \frac{2\pi\eta_a}{D}, \quad (1.1)$$

where  $\eta_a$  is the motion amplitude,  $U$  is the oscillation velocity amplitude,  $T$  is the oscillation period and  $D$  is the characteristic body length. The KC number can be considered the relative importance of drag and inertial forces and will be discussed in more detail in Section 2.6.

The work has been a part of a collaborative effort between several master's and Ph.D. prospects writing about multi-modular PV plants. Aas-Hansen and Fagerbakke created a simulator to investigate hinge optimization and Solberg conducted similar experiments with catamaran models. Additionally, Hals simulated two-dimensional cases of the aforementioned experiments using OpenFOAM. The main objective has been to create the basis of a Morison-type load formulation that accounts for 3D effects and wake interaction. Collaboration between Hals and Mikkelsen has been emphasized throughout the work to bridge the gap between the experimental results and numerical simulations and verify their accuracy.

## 1.1 Preproject Work - TMR4520

The work presented in this thesis is a direct continuation of the work conducted during the fall of 2022. This pre-project focused on building a solid theoretical background,

codes for post-processing procedures, and a preliminary understanding of the experiments. Experiments for the investigation of tandem cylinders were run in relation to this work. Much of the information in the first four chapters is therefore repurposed for this thesis, although expanded upon and improved [16].

## 1.2 Scope of Work

The primary objective of this thesis is to explore the hydrodynamic interaction between cylinders in close proximity and identify key factors that warrant further investigation. By delving into these factors, this research aims to provide a deeper understanding of the complex dynamics of fluid flow and hydrodynamic interaction. The obtained results will undergo thorough analysis to pinpoint crucial factors that necessitate additional investigation. These identified factors will hopefully serve as the foundation for future work focused on developing a Morison-type load formulation that adequately integrates hydrodynamic interaction. A comprehensive understanding of the fluid behavior in different configurations and under varying conditions is required for this endeavor.

To achieve this goal, a set of sub-objectives are created to properly delineate the scope of this thesis:

1. Perform a literary review and provide relevant theory and information on:
  - Hydrodynamic forces.
  - Turbulence and wake interaction in oscillatory flow.
  - Large KC numbers.
  - Morrison equation and load formulations.
2. Perform laboratory work:
  - Calibration.
  - Conduct experiments for tandem arrangement.
  - Conduct experiments for staggered arrangement.
  - Post-processing of results.
3. Perform numerical simulations:
  - Create FEM models using GeniE.
  - Do a mesh refinement analysis.
  - Create environments in HydroD.
4. Present the results in a good and comprehensible manner.
5. Compare the numerical and experimental results to assess their validity. This should be done for both the Wadam results, and complementary CFD results provided by Hals.
6. Provide recommendations on getting compliance between experimental and numerical results in further studies.
7. Provide guidance on the creation of a Morison-type load formulation.
8. Provide a solid foundation for future research on the topic of hydrodynamic interaction.



### 1.3 Motivation

Most greenhouse gases that trap the sun's heat are produced during the burning of fossil fuels, such as oil, gas, and coal, which contribute to over 70% of global greenhouse emissions and 90% of carbon dioxide emissions [25]. Energy demand is projected to increase in the coming years, resulting in a significant challenge for reducing greenhouse gas emissions. Traditional reliance on fossil fuels for meeting this growing energy demand poses a threat to the environment. Fossil-fuel alternatives are needed in order to meet the requirements of the green shift. Of these alternatives, photovoltaic power (PV) is projected to become the leading non-fossil fuel source by 2050 [3].

The growth of the PV sector has driven the increase in installed clean energy in recent years [21]. This rapid growth of the PV sector, as well as its expected continued growth, is the result of several factors. In short, a PV plant can be considered:

- Simple to install.
- Reliable to operate.
- Easy to scale.
- Of low cost.

Additionally, PV power is accessible worldwide at a low environmental impact and can be produced in near-settlement areas. However, two main limitations are hindering the growth of PV power [21]. These are because:

- PV plants are area demanding.
- Incentives for PV plants are declining.

A solution to these problems might already be proposed with a RES relative to PV power, the wind energy sector. Investments have been made to ensure that the wind energy sector can go offshore. If PV power were also deployed offshore, it would address the first limitation of limited space for PV installations. New incentives would likely be offered for the use of ocean space for offshore PV plants. Floating PV power may be the key to revitalizing PV growth. In addition, offshore PV production may improve power efficiency due to cooler temperatures. Research conducted on the working temperatures of partially floating PV plants in windy conditions found a working temperature reduction of 11.60°C, which subsequently rose the output efficiency to 20.28% [5]. This shows good correspondence with the writings of Rosa-Clot and Tina [21], who wrote that the power efficiency of PV panels increases by 0.5% for every degree drop in panel temperature.

Several concepts for floating PV plants are already in development and may contain floating membranes, multi-torus or modular structures. This thesis focuses on the hydrodynamic interaction between the pontoons of multi-modular PV structures.

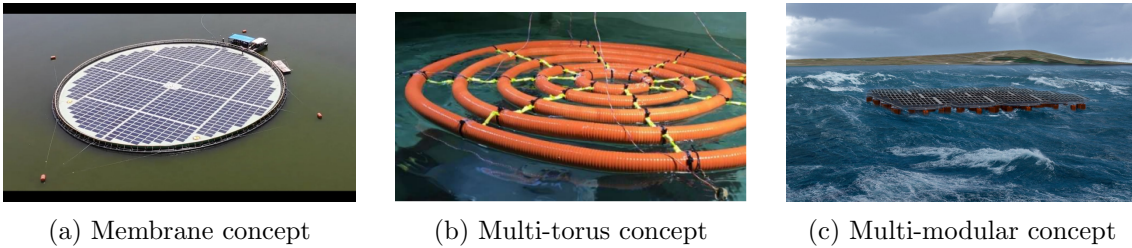


Figure 1.1: Three different concepts for floating PV structures.

Source: [24], [11] and [6]

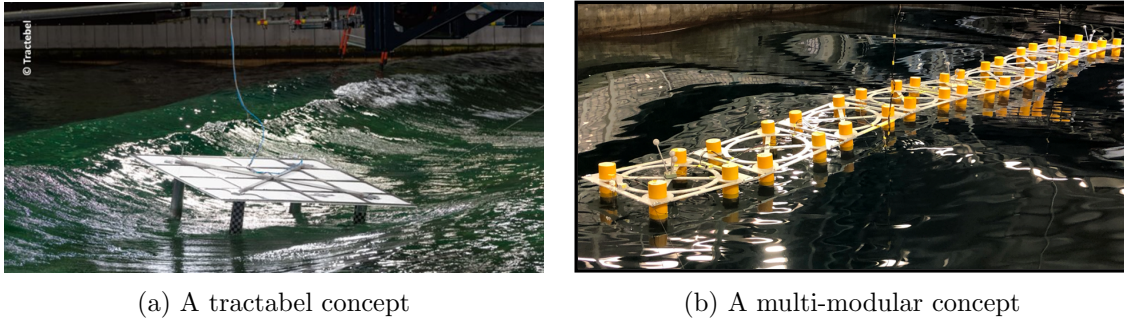


Figure 1.2: Two different solutions for modular PV structures.

Source: [10]

A concern associated with multi-modular PV concepts is the hydrodynamic interaction that occurs between cylindrical pontoons in close proximity. Previous experiments demonstrated substantial nonlinear effects, which can result in significant loads on the pontoons. The difference forces between two cylinders in particular have been identified as problematic. A large difference force must either be taken up in the hinges or in the mooring system. These forces are therefore important in the design of such systems. Furthermore, conventional use of the Morison equation is unsuitable to estimate some of these forces and detect some of the phenomena.

The main motivation behind this thesis has been to contextualize the force observations from experimental and numerical results in order to create a Morison-type load formulation. This research is part of SFI BLUES and is considered to be of high industrial relevance.

## 1.4 Literature Review

There are limited studies on the topic of hydrodynamic interaction on cylinders in tandem and staggered arrangement subjected to forced oscillatory flow. Furthermore, almost no research on the topic of square cylinders subjected to forced oscillatory flow, except for Reiten's master thesis from 2022 was found [19]. This is in contrast to the extensive research on dynamic interaction loads between circular cylinders in a steady flow. As outlined in 1977, wake interaction between two cylinders in steady flow has been studied extensively due to its relevance to the aerospace and offshore oil industries [26]. A multi-modular concept for a floating PV plant may be supported by 4 or more circular or quadratic cylinders. It is therefore reasonable to believe that hydrodynamic interaction between

the pontoons from both tandem and side-by-side arrangement is present. Therefore, the topic of two or more cylinders in forced oscillatory flow is of great importance for further research to support the transition to RES.

Zdravkovich wrote a review paper in 1977 outlining the flow interference between two circular cylinders in various arrangements. He distinguished between two distinct arrangements of cylinders; tandem arrangement and side-by-side arrangement. Every variation between these two is considered a staggered arrangement. His findings show two different flow patterns can be identified in the case of two cylinders in tandem arrangement. The first pattern does not produce vortex shedding behind the upstream cylinder, while the second flow pattern produces vortex shedding behind both cylinders. Moreover, he identified five different flow regimes for tandem arrangement, all dependent on the distance-diameter ratio.

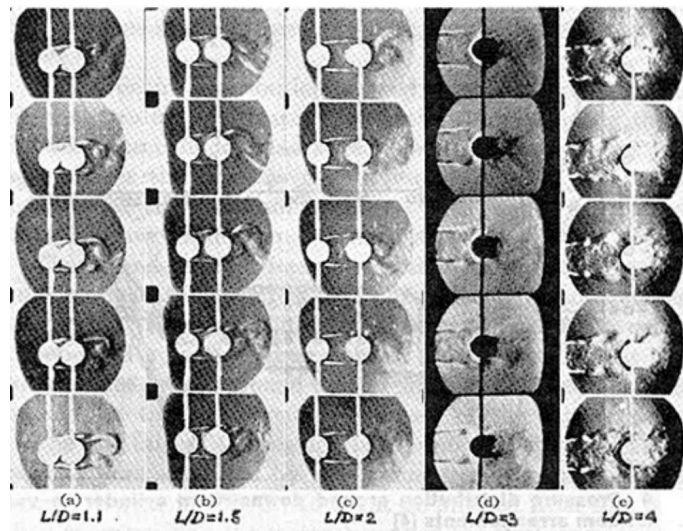
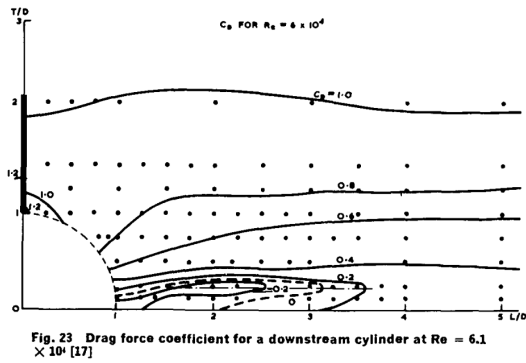


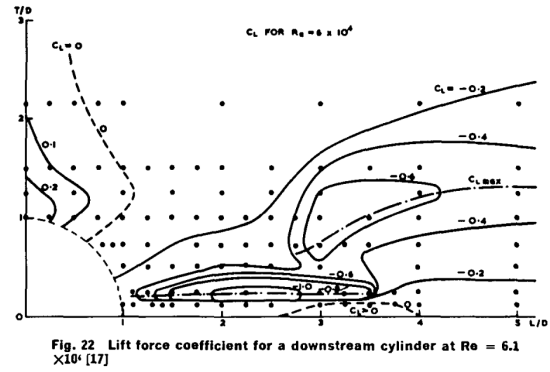
Figure 1.3: The five different flow regimes identified by Zdravkovich and the distance-diameter ratio they occur for. A distance-diameter ratio below and equal to two gives the first flow pattern.

Source: [26]

The first flow regime is when the shear layer separated from the upstream cylinder surpasses the second one. This happens when the two cylinders are located close to each other. The second regime occurs when the shear layer is reattached to the downstream cylinder, and the reattachment is synchronous with the shedding. A quasi-steady reattachment happens in the third flow regime, which will lead to highly irregular pressure distributions and shedding patterns. At the fourth regime, the distance-diameter ratio is large enough for the downstream cylinder to be hit by the wake recirculation. The fifth and final regime is when the distance-diameter ratio is large enough for the vortex shedding of the two cylinders to no longer be synchronous. All the five flow regimes of tandem arrangement can be seen in Figure 1.3 [26].



(a) Drag coefficients



(b) Lift coefficients

Figure 1.4: Contour plots by Zdravkovich for drag and lift coefficients for staggered arrangements as a function of both transverse and longitudinal spacing ratios.

Source: [26]

Zdravkovich also studied the drag and lift coefficients of the downstream cylinder for different inflow angles. The results are presented as contour plots in Figure 1.4. He identified five additional flow regimes for staggered arrangements. These are characterized by negligible lift and reduced drag, small repulsive lift and reduced drag, repulsive lift and increased drag, negligible lift and increased drag, and negative lift and decreased drag. The upstream cylinder can belong to any of the first three, while the downstream cylinder can also belong to the last two. More importantly, Zdravkovich noted that the two cylinders usually belong to different regimes at the same time.

One of the sources used in the review by Zdravkovich was the work by Biermann in 1933. He introduced interference drag, which is defined as the drag of the bodies in combination minus the drag of the bodies tested separately. His findings show that when two circular cylinders are placed in tandem arrangement the upstream cylinder drag is largely unaffected by the presence of the downstream one. However, the drag of the downstream cylinder is greatly reduced by the presence of the upstream cylinder. It was observed that this drag drop occurred rapidly for spacings smaller than 4 diameters. Biermann deduced that the probable reason for the drag force drop for the downstream cylinder was the presence of a turbulent wake from the upstream cylinder. Another observation was that both cylinder's drag becomes less than a single cylinder's drag when the spacing is less than 3.5 diameters. Probably the most interesting of Biermann's findings was that the force acting on the downstream cylinder was directed opposite the flow direction for spacings smaller than 3 diameters. This is probably because the vortices produced by the upstream cylinder partly encircle the downstream one, which might produce a sufficiently large force to create a forward response [2]. Subsequently, the interference drag coefficient showed a reduction when the spacing was less than 3 for the upstream cylinder, and an increase for the downstream cylinder when the spacing was 2.5. Zdravkovich also noted the same flow regime as Biermann, where the vortices from the upstream cylinder surpass the downstream one [26].

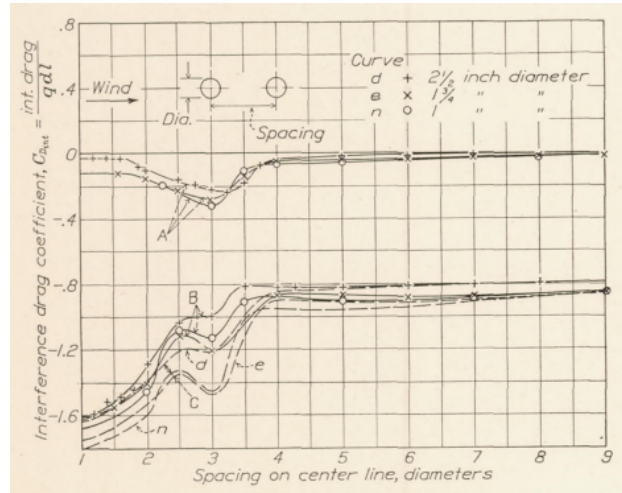


Figure 1.5: Interference drag coefficient for an upstream (A) and a downstream (B) cylinder. The results show that (A) is largely unaffected by the presence of (B), while (B) is significantly affected by (A).

Source: [2]

Reiten wrote about the topic of hydrodynamic forces and interaction between 2D square cylinders in oscillating flow in 2022. The research was conducted both experimentally and numerically using a combined effort of Mentzoni’s viscous solver and OpenFOAM (OF). Mainly, the sensitivity for the increased vertical and horizontal distance between cylinder pairs, offset, inflow angle, and the mesh was investigated. His findings showed a clear indication of hydrodynamic interaction between the pontoons. The results showed the presence of a large difference force  $\Delta F$  which was dominated by the  $2\omega$  harmonic, although the first and higher-order harmonics were also present. Due to cancellation effects, the first harmonic force was noted to be small. Interestingly,  $\Delta F$  increased as the KC number increased, which indicates good correspondence with the writings of Biermann and Zdrakovich [2][26].

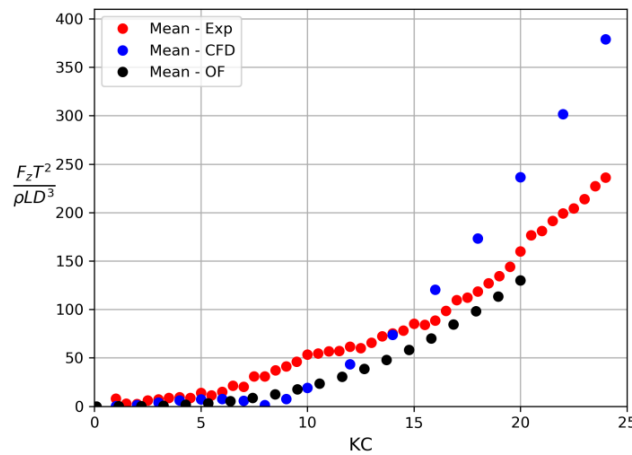


Figure 1.6: Comparison of mean  $\Delta F$  from experimental, OpenFOAM and Mentzoni’s viscous solver results from the Master’s thesis by Reiten.

Source: [19]

Another noteworthy fact is that Mentzoni's viscous solver consistently overestimated the cylinder forces at high  $KC$  numbers, as shown in Figure 1.6 [19]. This is explained by the solver not using a turbulence model. Wakes are turbulent by definition and wake interaction was found to be significant, which therefore explains the large discrepancies between the viscous solver and OF.

Sarpkaya, a scientist with extensive work on oscillating flow, found no correlation between the drag and inertia coefficients and the Reynolds number. However, he discovered that both coefficients correlate well with the  $KC$  number. His investigation was conducted experimentally using a large U-tank with a cylinder placed in one of the tank sides. He determined the drag, inertia, and lift coefficients by the use of a Fourier analysis of the terms in the Morison equation. This analysis showed that the forces on cylinders may oscillate with several frequency components such as  $\omega$ ,  $2\omega$ ,  $3\omega$  and  $4\omega$  during a load cycle [22].

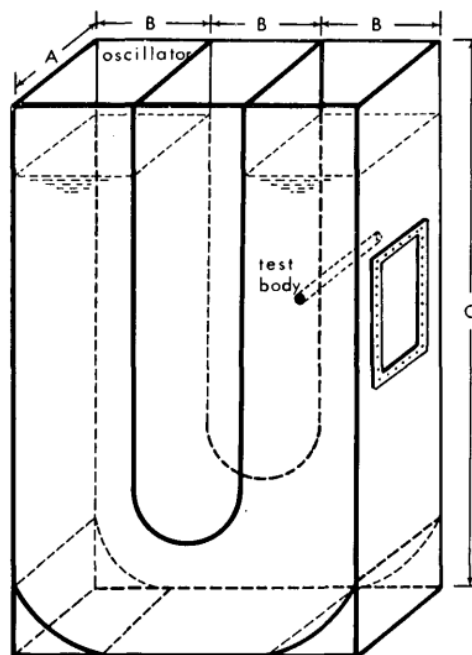


Fig. 1 Schematic drawing of the U-shaped vertical water tunnel;  $A = 46$  cm (18 in.),  $B = 51$  cm (20 in.),  $C = 254$  cm (100 in.)

Figure 1.7: Schematic of the U-tank used by Sarpkaya

Source: [22]

Li wrote his master's thesis on the topic of two finite staggered cylinders in crossflow. His findings showed that the difference in Strouhal number  $St$  between the two cylinders is larger for finite cylinders compared to infinite cylinders. Furthermore, the  $St$  power spectra indicated clear and pronounced peaks at the mid-height of the cylinders, while broader spectra with weak or no peaks were observed at the base and ends. This indicates that the vortex-shedding frequency changes along the height of the cylinders, and that higher-order frequencies are expected to be more prevalent at the base ends. He also found that moderately spaced cylinders are likely to experience different  $St$  numbers, and identified a large discontinuity in  $St$  at a critical inflow angle at around  $85^\circ$  to  $75^\circ$ . Overall, He Li noted a stronger interaction between finite cylinders compared to infinite [13].

# Chapter 2

## Theory

The most relevant theory for this project will be presented in this chapter. These include the fundamental governing equations, including a set of important dimensionless coefficients often used in a marine setting.

### 2.1 Dynamic Equilibrium

We start with Newton's second law whenever we want to find the expression for the dynamic equilibrium of a system. Newton's second law states that the sum of the forces acting on a body is equal to the product of mass and acceleration. This is expressed as

$$\sum \vec{F} = m\vec{a}, \quad (2.1)$$

where  $\vec{F}$  and  $\vec{a}$  indicate the vector sum of the forces and acceleration, and  $m$  is the mass. If we consider a six-DOF system, the body position can be written as  $\eta = [\eta_1, \eta_2, \eta_3, \eta_4, \eta_5, \eta_6]^T$  with body velocity as  $\dot{\eta}$  and acceleration  $\ddot{\eta}$ . These terms are associated with stiffness, damping, and inertial force contribution respectively. Newton's second law will then evolve to

$$-B\dot{\eta}(t) - C\eta(t) + P(t) = m\ddot{\eta}(t), \quad (2.2)$$

where  $B$  is the damping matrix,  $C$  is the stiffness matrix and  $P$  is an external load vector. Note that for a six-DOF system  $m$ ,  $B$ , and  $C$  are quadratic matrices with dimensions of 6x6, while  $P$  is a six-long vector. We can reformulate Equation (2.2) by moving the damping and stiffness terms and isolating the load vector. This will yield the more popular version

$$m\ddot{\eta}(t) + B\dot{\eta}(t) + C\eta(t) = P(t). \quad (2.3)$$

There are four kinds of loads acting in this system, external load, inertial, damping, and stiffness forces. This dynamic equilibrium equation is a linear second-order differential

equation where the coefficients  $m$ ,  $B$ , and  $C$  are constant. The solution of the system will subsequently be on the form

$$\eta(t) = \eta_H(t) + \eta_P(t), \quad (2.4)$$

where  $\eta(t)$  is the time dependent displacement,  $\eta_H(t)$  is the contribution from the homogeneous solution and  $\eta_P(t)$  is the contribution from the particular solution [1].

## 2.2 Wave Excitation Forces

A floating rigid body exposed to waves will in general respond in six degrees of freedom. It will also create free-surface disturbances when it moves. These disturbances include waves, which are referred to as radiated waves or the radiation problem. By combining the radiation problem with the diffracted waves and the incident wave velocity potentials, one can express the total wave field as a linear superposition of all velocity potentials. The biggest advantage of linearised potential flow theory is that each problem can be solved separately. This will yield

$$\phi = \phi_0 + \phi_7 + \sum_{i=1}^6 \phi_i, \quad (2.5)$$

where  $\phi_0$  is the incident wave velocity potential,  $\phi_7$  is the diffracted velocity potential and the rest are the sum of all radiated velocity potentials for all six dofs. By relating Equation (2.5) to the dynamic equilibrium in Equation (2.3), all velocity potentials from the radiation problem will determine the components of the hydrodynamic mass, damping and stiffness matrices. We can then recognize that the diffraction and incident wave problems will determine the excitation loads.

We want to obtain the force acting on a body, which in the context of this work is a square cylinder. The hydrodynamic excitation forces can be found by integrating the pressure acting on the wet body surface. This pressure is found by using the linear Bernoulli equation given in Equation (2.6).

$$p = -\rho \frac{\partial \phi}{\partial t} - \frac{\rho}{2} \nabla \phi \cdot \nabla \phi - \rho g z + C(t) \quad (2.6)$$

Because we are only interested in the dynamic force contribution, all static terms will disappear. The velocity potential that gives the excitation forces will be the sum of the incident wave potential and the diffracted potential. We can also utilize that the partial derivative is a linear operator and that the two potentials  $\phi_0$  and  $\phi_7$  can subsequently be treated separately. The Bernoulli equation will then be reduced to

$$p_d = -\rho \frac{\partial(\phi_0 + \phi_7)}{\partial t} = -\rho \frac{\partial \phi_0}{\partial t} - \rho \frac{\partial \phi_7}{\partial t}. \quad (2.7)$$

By integrating Equation (2.7) over the body surface, the expression for the excitation force  $F_i^{exe}$  is obtained in Equation (2.8). This expression gives force contributions; the Froude-Kriloff force and the diffraction force [1].



$$F_i^{exe} = \int_{S_0} p_d n_i dS = \underbrace{\rho \int_{S_0} \frac{\partial \phi_0}{\partial t} n_i dS}_{\text{Froude-Kriloff}} + \underbrace{\rho \int_{S_0} \frac{\partial \phi_7}{\partial t} n_i dS}_{\text{diffraction}} \quad (2.8)$$

It can be seen that the Froude-Kriloff expression is simply an integration of the pressure in the undisturbed wave over the body surface. This integral may be solved without solving any boundary value problems related to the body. However, the second term, the diffraction problem, needs to be solved numerically. Several commercial codes such as WAMIT and DNV Wadam provide solutions to both linear and second-order problems and can be used to solve diffraction. Wadam will be used for this project.

### 2.3 Hydrodynamic Force

The added mass and damping loads acting on a body can be defined as the loads acting in phase with acceleration and velocity respectively [1].

$$F_{jk}^{hd} = -\rho \int_{S_0} \frac{\partial \phi_k}{\partial t} n_j dS \quad (2.9)$$

The forced oscillation of the actuator in this thesis can be considered harmonic, meaning we can estimate the model motion to be a simple sine or cosine function. If we assume a displacement function equal to Equation (2.10), the functions for cylinder velocity and acceleration will follow naturally to Equation (2.11) and Equation (2.12) respectively.

$$\eta_2(t) = \eta_{2a} \cos(\omega t) \quad (2.10)$$

$$\dot{\eta}_2(t) = -\omega \eta_{2a} \sin(\omega t) \quad (2.11)$$

$$\ddot{\eta}_2(t) = -\omega^2 \eta_{2a} \cos(\omega t) \quad (2.12)$$

Here,  $\eta_a$  represents the amplitude of the oscillation and  $\omega$  is the oscillation radial frequency. Because we have assumed a linearized problem with incident wave frequencies of  $\omega$ , all the responses will oscillate with the same frequency. This includes both body motions and wave loads. The velocity and acceleration of the body are 90 degrees out of phase since the acceleration and the velocity are orthogonal functions. Any sinusoid may therefore be expressed as the sum of the velocity and acceleration of the body. In other words, Equation (2.9) can be rewritten to express any mode as

$$F_{jk}^{hd} = -A_{jk} \ddot{\eta}_j - B_{jk} \dot{\eta}_j, \quad (2.13)$$

where  $A_{jk}$  and  $B_{jk}$  are the added mass and damping matrices respectively. It will be beneficial to separate the added mass and damping terms from each other. We know that any integration over an arbitrary number of whole periods when the term consists of orthogonal harmonic functions will be zero. This is called Fourier averaging and is one of the possible ways to separate the damping and added mass terms. Added mass can be solved by multiplying each side of Equation (2.9) by Equation (2.12), i.e acceleration, and integrating over an arbitrary number of whole periods. This will yield

$$\int_{nT} P\ddot{\eta}_2(t)dt = \int_{nT} A_{22}\ddot{\eta}_2(t)\ddot{\eta}_2(t)dt + \underbrace{\int_{nT} B_{22}\ddot{\eta}_2(t)\dot{\eta}_2(t)dt}_{=0}, \quad (2.14)$$

where  $n$  is the number of oscillation periods. By performing the same procedure with velocity, an expression for the damping term can be found. This means to multiply Equation (2.9) by Equation (2.11) instead of acceleration. This will instead yield

$$\int_{nT} P\dot{\eta}_2(t)dt = \underbrace{\int_{nT} A_{22}\dot{\eta}_2(t)\dot{\eta}_2(t)dt}_{=0} + \int_{nT} B_{22}\dot{\eta}_2(t)\dot{\eta}_2(t)dt. \quad (2.15)$$

We can determine expressions for the added mass and damping matrices by reshuffling Equation (2.14) and Equation (2.15) and solving for the added mass and damping. The result of this operation will be as shown in Equation (2.16) and Equation (2.17).

$$A_{22} = -\frac{\int_{nT} P\ddot{\eta}_2(t)dt}{\int_{nT} \ddot{\eta}_2(t)\ddot{\eta}_2(t)dt} \quad (2.16)$$

$$B_{22} = -\frac{\int_{nT} P(t)\dot{\eta}_2(t)dt}{\int_{nT} \dot{\eta}_2(t)\dot{\eta}_2(t)dt} \quad (2.17)$$

It is beneficial to present the added mass and damping as non-dimensional values, and a reference added mass value is therefore introduced. This reference added mass is specifically chosen to be the analytical added mass for a flat plate and circular cylinder of equal width of the body. The expression is

$$A_0 = \rho \frac{\pi}{4} D^2 L, \quad (2.18)$$

where  $\rho$  is the water density,  $D$  is the cylinder width and  $L$  is the cylinder length. By using this reference along with Equation (2.11) and Equation (2.12), assuming harmonic oscillation, Equation (2.13) can be non-dimensionalized and rewritten as

$$\frac{F}{\omega^2 \eta_a A_0} = \frac{A_{22}}{A_0} \cos \omega t + \frac{B_{22}}{\omega A_0} \sin \omega t \quad (2.19)$$

Note that by using this reference, the non-dimensional added mass and damping coefficients can be written as  $C_a = \frac{A}{A_0}$  and  $C_b = \frac{B}{\omega A_0}$  respectively.  $C_a$  and  $C_b$  then coincide with the convention typically used in the literature. It is possible to further simplify Equation (2.19) by merging the two terms to a single sinusoid and using  $C_a$  and  $C_b$ . Equation (2.19) then becomes

$$\frac{F}{\omega^2 \eta_a A_0} = \sqrt{\left(\frac{A_{22}}{A_0}\right)^2 + \left(\frac{B_{22}}{\omega A_0}\right)^2} \sin(\omega t + \phi) = \sqrt{C_a^2 + C_b^2} \sin(\omega t + \phi). \quad (2.20)$$

Here,  $\phi$  is the phase between the velocity and the non-dimensional force, while  $\sqrt{C_a^2 + C_b^2}$  becomes the amplitude. The non-dimensional force amplitude is a function of the squared

added mass and damping coefficients. If one is larger than the other, the amplitude may quickly become dominated by the larger term due to being squared. They can either be evaluated as a ratio relative to each other, or as the percentwise contribution to the force amplitude. The ratio can be defined as

$$\frac{C_b}{C_a} = \frac{B}{\omega A}. \quad (2.21)$$

A ratio larger than 1 indicates that damping dominates the force amplitude, while a lower than 1 indicates that added mass dominates. Alternatively, the percentwise contribution of  $C_b$  to the amplitude can be evaluated. This may be written as

$$\frac{\sqrt{C_b^2}}{\sqrt{C_a^2 + C_b^2}} = \frac{\frac{B}{\omega A}}{\sqrt{1 + \left(\frac{B}{\omega A}\right)^2}}. \quad (2.22)$$

Likewise, the added mass can also dominate if  $C_a$  is larger than  $C_b$ . Both sides of Equation (2.22) can be used, but the left side is used for this thesis as  $C_a$  and  $C_b$  is extracted automatically from the experiments [15].

## 2.4 Hydrodynamic Damping Forces

The damping loads of a marine system are the load terms that are dependent on the relative body and water particle velocity. However, it is known that damping loads of a system may have both linear and nonlinear characteristics. Common practice is therefore to split the damping term into one term proportional to the velocity, and one term proportional to the velocity squared. In other words, the damping term in Equation (2.13) can be rewritten as

$$B_{jk}\dot{\eta}_j = B_{jk}^{(1)}\dot{\eta}_j + B_{jk}^{(2)}\dot{\eta}_j|\dot{\eta}_j|, \quad (2.23)$$

where (1) and (2) denotes the linear and quadratic damping terms respectively. Typically, the first-order term is associated with a linear wave-radiation force, while the second-order term is associated with viscous drag forces.

## 2.5 Reynolds Number

In 1883, Osborne Reynolds conducted experiments investigating what determines if the motion of water particles is direct or sinuous. His findings showed that the ratio between inertial forces and viscous shear forces is important in determining the fluid motion behavior [20]. This ratio was later named the Reynolds number by Sommerfeld in 1908 [23], a name that stuck ever since. The Reynolds number is defined as

$$\text{Re} = \frac{UL}{\nu}, \quad (2.24)$$

where  $U$  is the mean inflow speed,  $L$  is the characteristic linear dimension and  $\nu$  is the kinematic viscosity. The Reynolds number is an important quantity in marine technology due to its influence on many important hydrodynamic coefficients. One famous example is the Re-dependent drag coefficient  $C_D$ , which is a factor in the drag and Morison equations.

## 2.6 Keulegan-Carpenter Number

The Keulegan-Carpenter number is a dimensionless quantity formulated by Garbis H. Keulegan and Lloyd H. Carpenter in 1950. It describes the relative importance between drag forces and inertial forces that is experienced by a blunt body in oscillating flow [9]. A large Keulegan-Carpenter number will therefore indicate that drag forces dominate, while small numbers indicate that inertial forces dominate. The Keulegan-Carpenter number  $KC$  is defined as

$$KC = \frac{UT}{D}, \quad (2.25)$$

where  $U$  is the amplitude of the relative flow velocity oscillation,  $T$  is the oscillation period and  $D$  is the characteristic length scale of the body. Oscillating water particle flow and still water body oscillation are synchronous in this case. The laboratory setup for this thesis is a harmonically oscillating body. It can be shown that

$$KC = \frac{2\pi\eta_a}{D} \quad (2.26)$$

by combining Equation (2.25) with the fact that  $\omega = \frac{2\pi}{T}$  and  $U = \omega\eta_a$  for an harmonically oscillating body. If the body is subjected to waves, and the wave follows linear potential theory, the water particle velocity amplitude can be expressed as a function of wave height  $\zeta_a$  as described in Sea loads [7]. The expression for the  $KC$  number will then become

$$KC = \frac{2\pi\zeta_a}{D}. \quad (2.27)$$

## 2.7 Morison's Equation

In 1950, a team of master students consisting of Morison, O'Brien, Johnson, and Schaaf wrote their thesis in light of the US offshore expansion in the 50s. They stated that the force exerted from unbroken waves on a cylinder that extends from the bottom to above the crest can be summed up into two parts. These two parts are:

1. A drag force proportional to the square of the velocity which may be represented by a drag coefficient having substantially the same value as for steady flow, and
2. A virtual mass force proportional to the horizontal component of the accelerative force exerted on the mass of water displaced by the pile [17].

These relationships follow directly from fluid dynamics and linear wave theory and were verified by experiments conducted at the University of Berkley. The first of these relationships is analog to the drag equation, while the relationship for virtual mass can be derived from linear wave theory. This work resulted in a semi-empirical equation for wave loads on a circular cylinder, that could be expressed as

$$dF_M = \underbrace{\rho \frac{\pi D^2}{4} C_a a(t)}_{\text{inertial term}} + \underbrace{\frac{1}{2} \rho D C_D u(t) |u(t)|}_{\text{viscous term}}, \quad (2.28)$$

where  $a(t)$  is the water particle acceleration,  $u(t)$  the water particle velocity while  $C_a$  and  $C_D$  are the added mass and drag coefficients. The absolute value around the one  $u(t)$  term ensures that flow direction is accounted for. In other words, the wave loads experienced by a cylinder can be expressed by a superposition of an inertia force and the drag equation.

If the body is considered fixed and subjected to oscillating flow, the Froude-Kriloff force needs to be included in Equation (2.28). That is, to introduce the mass coefficient  $C_M$  expressed by  $C_M = C_a + C_f$ . Froude-Kriloff forces can be obtained by integrating the pressure gradient that accelerates the water particles in the oscillating flow [19]. The Morison equation will evolve into

$$F_M = \rho \frac{\pi D^2}{4} C_M \ddot{\eta}_3 + \frac{1}{2} \rho D C_D \dot{\eta}_3 |\dot{\eta}_3| \quad (2.29)$$

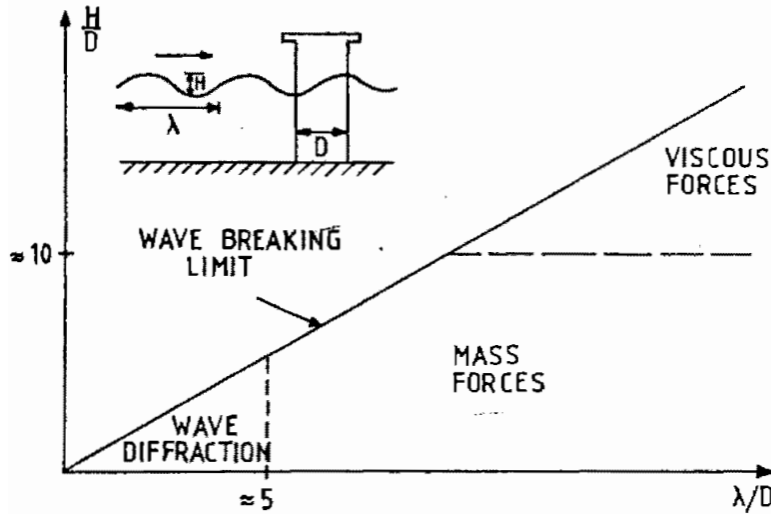


Figure 2.1: Relative importance of mass, viscous and diffraction forces on marine structures.

Source: [7]

We know that probable  $KC$  numbers for a multi-modular PV plant in offshore conditions may be as high as 15-20 or even more. Moreover, a realistic characteristic length scale of the pontoons of a PV module may be of the order of 1. By using Equation (2.27) with the relative importance between different hydrodynamic loads as outlined by Faltinsen and seen in Figure 2.1, we can determine which load type is expected to dominate for a structure [7].

The experimental results are presented in accordance with the description provided in Section 2.3. The objective is to establish a connection between the results and the Morison equation. In order to achieve a consistent format for both, we will start by linearizing the viscous term and substituting one of the velocity terms with the amplitude in Equation (2.10). Consequently, Equation (2.28) is reformulated as

$$F_M = \rho \frac{\pi D^2}{4} C_a \ddot{\eta}_3(t) L + \frac{1}{2} \rho D C_D \frac{8}{3\pi} (\omega \eta_a) \dot{\eta}_3(t) L, \quad (2.30)$$

where  $\frac{8}{3\pi}$  is the first harmonic component of  $\sin(\omega t) |\sin(\omega t)|$ . Equation (2.13) is already linear, allowing a direct relationship between the two equations. By substituting  $A = C_a A_0$  and  $B = C_b \omega A_0$ , Equation (2.13) can be expressed as

$$F_{exp} = C_a A_0 \ddot{\eta}_3 + C_b \omega A_0 \dot{\eta}_3. \quad (2.31)$$

We can then equate the inertial and damping terms in Equation (2.30) and Equation (2.31). Furthermore, the reference added mass  $A_0$  is expressed using Equation (2.18). Substituting this expression for  $A_0$  and solving for  $C_a$  and  $C_D$  will yield

$$C_D^{exp} = \frac{C_b \omega \rho \frac{\pi}{4} D^2 L \dot{\eta}_3}{\frac{1}{2} \rho D \frac{8}{3\pi} (\omega \eta_a) \dot{\eta}_3 L} = \frac{3\pi^3}{8KC} C_b. \quad (2.32)$$

The experimental added mass coefficient can be used directly while the experimental drag coefficient is calculated using Equation (2.32). This allows for a comparison between traditional Morison equation and the experimental force coefficients.

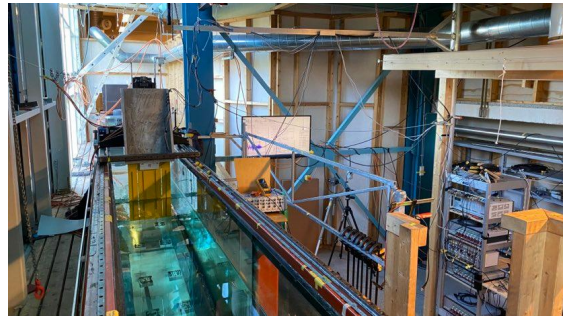
## Experimental Setup

### 3.1 Facilities

The experiments were conducted at the center of Marine Technology in the Ladertanken laboratory. This narrow wave flume tank is run by NTNU and is primarily used by students for laboratory work in MSc or Ph.D. courses. The tank is also occasionally used for research purposes as demonstrated by Pål Lader, who built the tank and used it in his Ph.D. work.



(a) Bottom-up overview of Ladertanken



(b) Top-down overview of Ladertanken

The tank holds a length and breadth of 13.5m and 0.6m respectively. It has a wave flap mounted on the far left side of the tank, which can produce waves alongside the longitudinal direction of the tank. A parabolic beach is mounted on the other end to dampen the waves and prevent reflection back to the rig. The cylinder models were forced to oscillate using a vertical actuator, so the wave flap was not used during the experiments. To access the cylinders, the tank had to be partially emptied between each run and then refilled to a depth of 1 meter with fresh water from the Sea pool run by SINTEF. The water was also refilled if the experiments had been idle for a long time, as it evaporates over time. All the walls and the floor of the tank are made of glass, making it possible to take pictures and videos of the experiments.

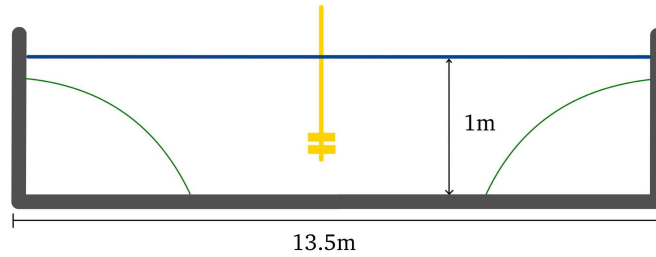


Figure 3.2: Simple schematic of Ladertanken, with parabolic beaches at the ends.

## 3.2 Apparatus and Equipment

The vertical actuator was placed in the middle of the tank. Attached to the actuator were two separate metal plates, the outer plate surrounding the inner plate. These plates were connected to separate force measurement devices so the contribution of the cylinders could be measured individually. For cases where four cylinders are present, each cylinder pair attached to the same plate had their force contributions measured together. Each of the two plates has two stiffeners welded to the respective plate and with screw holes drilled into the plate for cylinder assembly. The cylinders were mounted with an equal counterpart on the opposite side of the plate to create a  $yz$ -symmetry. This ensures that there were no inherent moment contributions in the system that may affect the force measurements.

The actuator itself allows for control of both vertical amplitude and oscillation period. This enables us to program the actuator for a large range of different  $KC$  numbers according to Section 2.6. The maximum amplitude of the actuator was restricted to 20cm, which along with periods of 1.0s and 1.5s allows us to test  $KC$  numbers up to 22.



Figure 3.3: Vertical oscillator from different perspectives



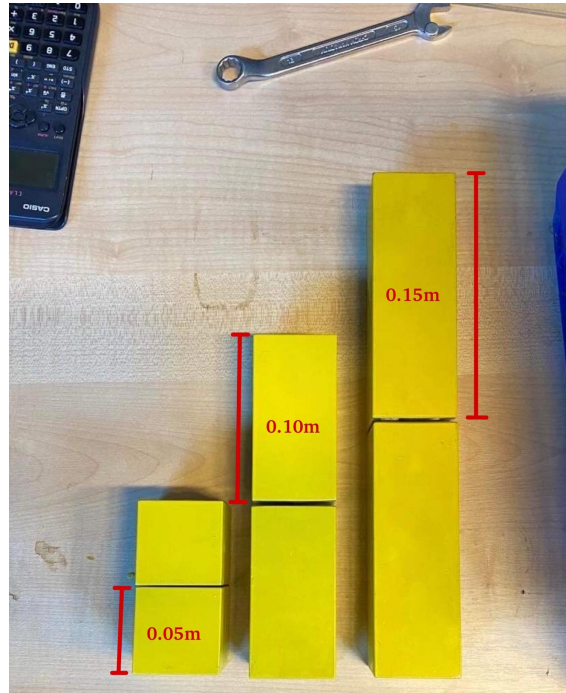


Figure 3.4: Alternating cylinder lengths

All cylinders used in this project had a 5cm width with three different lengths that the test cases alternated between. These included a short cylinder of 5cm, a medium-length cylinder of 10cm, and a long cylinder of 15cm. Each test case was run for all three cylinder lengths. The cylinders were secured by a mumle, and the mumle cavities were sealed by tack. The cylinders are mirrored by the plate due to symmetry concerns.



Figure 3.5: Case 4 with cylinder lengths  $L = D$ .

### 3.3 Test Configurations

Two different experiments have been conducted to investigate the scope of this thesis. The first of these was conducted in the fall semester in conjunction with the pre-project work and is designed to explore cylinders in tandem. The second was conducted in the spring semester and designed to capture the effects of inflow angles. Tandem and staggered are chosen as names to keep with the naming conventions of Zdravkovich [26].

### 3.3.1 Tandem Arrangement

Four main cylinder configurations were run during the experiments for tandem arrangement. Case 1 is two cylinders in tandem condition with a cylinder spacing  $S$  equal to one cylinder width  $D$ . Similarly, Case 2 also has two cylinders in tandem, but with a spacing of  $S = 2D$ . Case 3 represents a module consisting of four cylinders with equal spacing  $S = D$  between all horizontal and vertical pairs. Lastly, Case 4 covers two cylinders in a staggered arrangement where the spacing between the two cylinders becomes  $S = D$ . This means that Case 4 becomes a special expression of Case 1, where an oscillatory inflow of  $\theta = 45^\circ$  is considered. Case 11, Case 12, and Case 13 have the same configurations as cases 1-3, but with a diamond instead of square geometry. The difference between square cylinders and diamond cylinders is the latter being square cylinders rotated 45 degrees. A sketch of these two is provided by Figure 3.6.

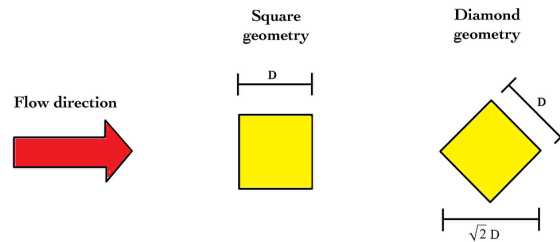


Figure 3.6: Schematic of square and diamond geometries

Seven cases total are run for the experiments, and an overview can be seen in Figure 3.7. Additionally, a separate test Case 0 was run without any cylinders. This is to capture the force contribution from the rig, and is discussed in more detail in Chapter 4 with regards to the post-processing.

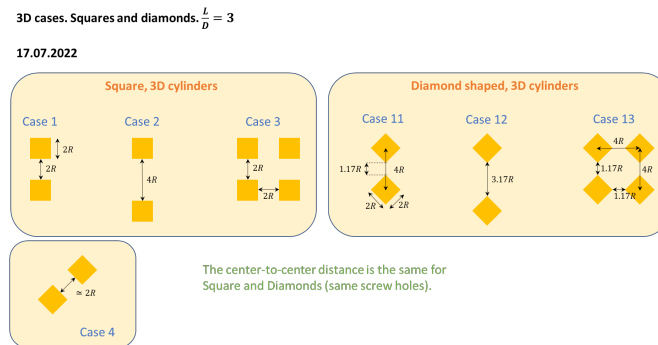


Figure 3.7: Overview of all the different test cases of the investigations

Source: [10]

Not all cases are needed to investigate the scope and motivation presented in Section 1.2 and 1.3. For the purposes of this thesis, only square geometry is considered and the effect of changing geometry is not evaluated. As the staggered arrangement has its own dedicated experimental investigation, Case 4 from the tandem experiments is neglected.

### 3.3.2 Staggered Arrangement

The staggered arrangement experiments aim to investigate the effect of changing the inflow angle  $\theta$ . Due to limitations with the experimental rig and setup, the spacing ratio was kept constant at  $\frac{S}{D} = 2$ . This means that the staggered experiments are a special realization of Case 2 where the setup is rotated to get an inflow angle. Additionally, inflow angles below  $\theta = 35^\circ$  were unable to be tested. A Sketch of the staggered arrangement is provided in Figure 3.8.

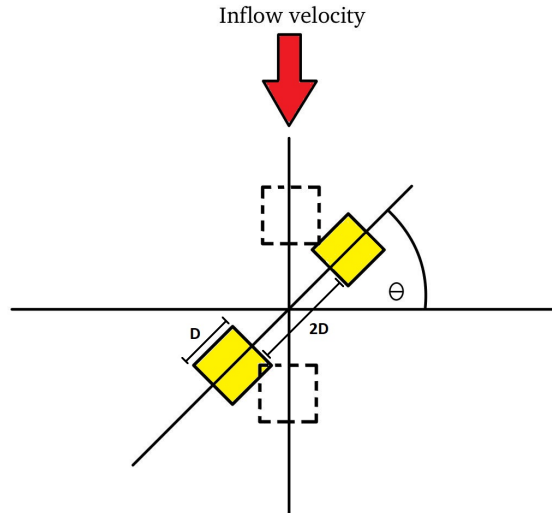


Figure 3.8: Sketch of the staggered arrangement experiments with the test parameter  $\theta$

## 3.4 Hammer Tests

The rig consists of numerous mechanical components that can result in measurement inaccuracies due to resonance-induced noise. Filtering this noise is possible given that the frequencies of the noise are sufficiently far from the frequency of the forced oscillating motion. Significant amplification of the measurements is expected if this is not the case, and the frequency components close to the rig's eigenfrequencies need to be discarded from the results.

To address this issue, a hammer test was conducted on several of the components attached to the rig. This involved gently hitting the tank, attachments, rig, and plates with a rubber hammer while simultaneously logging the data. By analyzing the hammer test data, any noise that may have affected the measurements can be identified. Each of the aforementioned locations is hit from multiple directions and the results are stored separately. Examples of the resulting time series created from the hammer test are provided in Figure 3.9 and Figure 3.10.

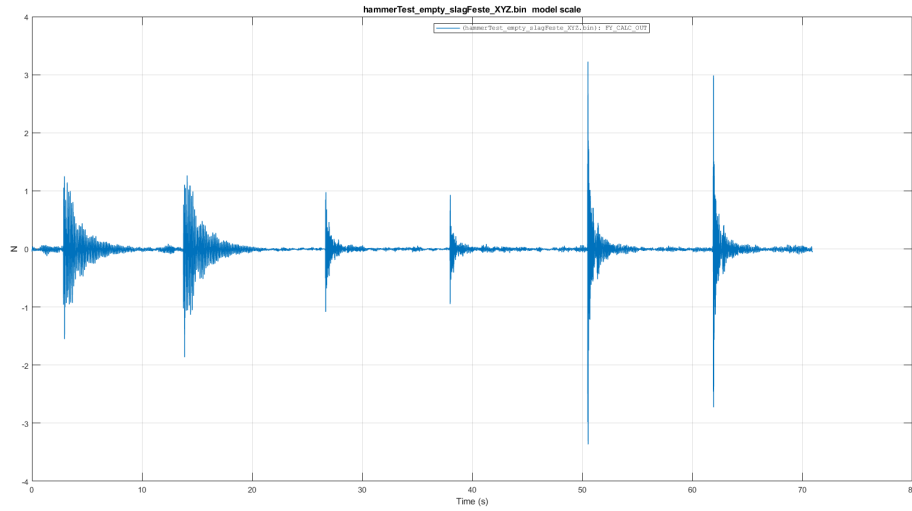
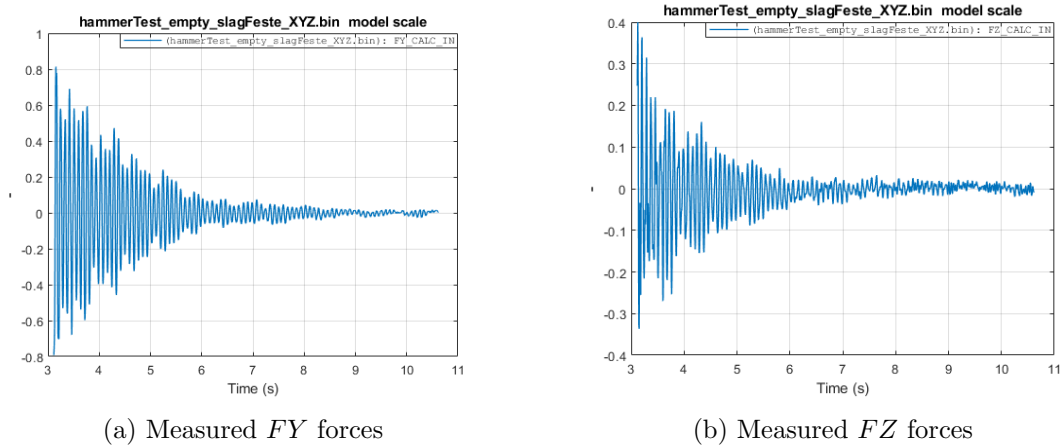


Figure 3.9: Example of a time-series created from the hammer test.



(a) Measured  $FY$  forces

(b) Measured  $FZ$  forces

Figure 3.10: Example of time series immediately after hammer strikes on the empty rig configuration.

The frequencies of the rig vibrations were determined through Fourier analysis of the isolated data, as illustrated in Figure 3.10. The results from the hammer test show that frequency variations were independent of the degree of freedom and the location where the rubber hammer was applied.

The results revealed that the eigenfrequencies of the rig decreased when mass was added to the plate, by introducing longer cylinders. Specifically, the lowest eigenfrequencies of the rig decreased from 7 Hz for the empty plate to 6 Hz and 4.5 Hz for the plate with small and large cylinders. These results are illustrated in Figure 3.11, Figure 3.12, and Figure 3.13. These plots depict the frequency response for each of the three test cases during the hammer test. Further analysis and determination of the ramifications from the hammer test will be discussed in Section 4.4, where filtration of the measurements will be discussed.

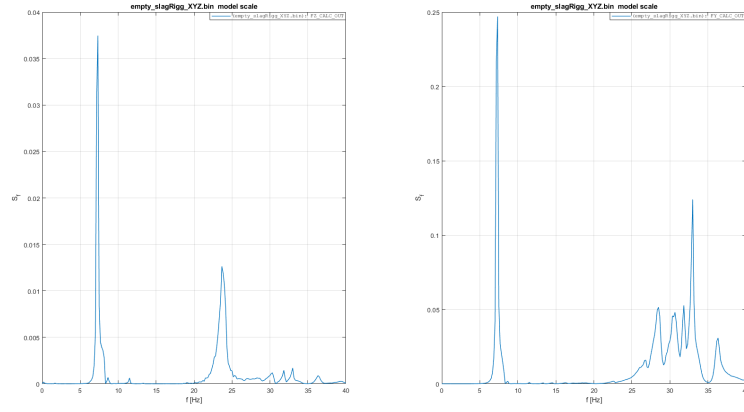


Figure 3.11: Hammer test results for the empty rig configuration. The results for  $FZ$  are presented in the left plot, while the results for  $FY$  are presented in the right plot.

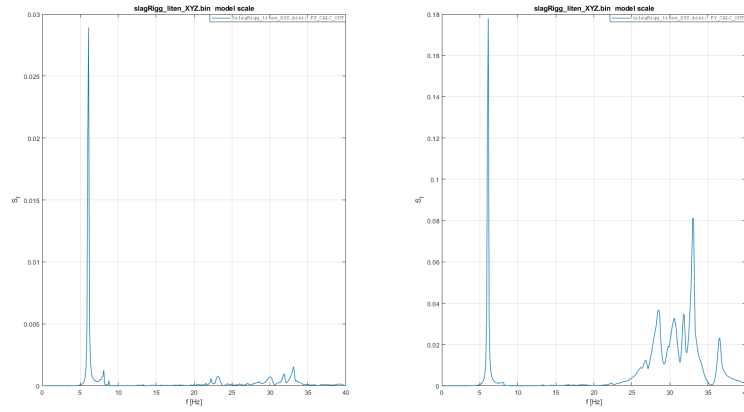


Figure 3.12: Hammer test results for case 2 with small cylinders. The results for  $FZ$  are presented in the left plot, while the results for  $FY$  are presented in the right plot.

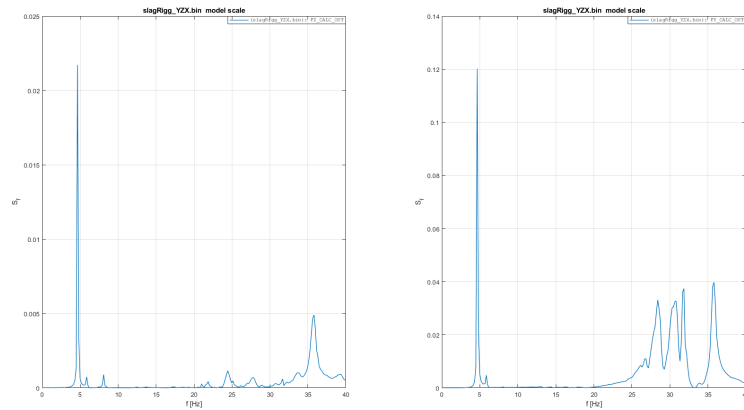


Figure 3.13: Hammer test results for case 2 with large cylinders. The results for  $FZ$  are presented in the left plot, while the results for  $FY$  are presented in the right plot.

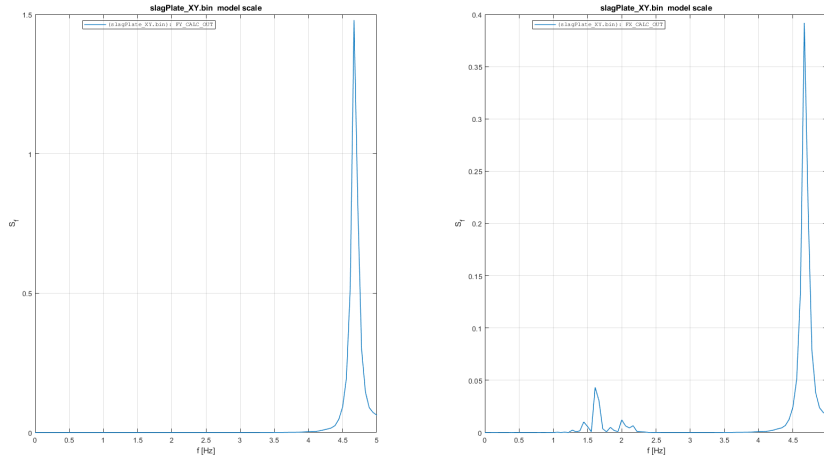


Figure 3.14: Zoomed hammer test results for case 2 with large cylinders. The results for  $FY$  are presented in the left plot, while the results for  $FX$  are presented in the right plot. A small peak around  $1,5Hz$  is observed for  $FX$ .

In addition to the eigenfrequency and mode shape analysis, the hammer tests also revealed some excitation along the longitudinal direction of the tank, particularly at frequencies between 1.5 to 2 Hz. At this time it is unclear whether this excitation is due to a particular eigenfrequency or if it is the result of the hammering direction. No evidence indicates that the frequency components in the drag and lift directions for the cylinders are affected by this noise.

### 3.5 Sources of Error

There are, generally speaking, two different types of errors that occur during experimental investigations. These are random errors and systematic errors. Random errors occur because there always is some variability between tests. Such variability may be due to slight fluctuations in instrumentation, environment, or simply due to chance. Repetition and averaging of results help smear out the effect of any spurious modes and reduce the significance of random error. The systematic error provides measurements that are consistently different from the experiment's true value. Bad calibration of either instruments or procedures is a typical source of systematic error and is usually harder to detect.

The experiments operate under the assumption of infinite fluid. Interaction between the tank boundaries and surface is expected due to limitations regarding the tank. This is especially true for the largest  $KC$  numbers, where the amplitude of the oscillation is highest. The cylinders are located in the center of the tank in an effort to minimize wall and surface effects. Despite this effort, small surface disturbances can be observed, meaning that the infinite water assumption is imperfect.

Experimental rigs are designed to provide controlled environments for scientific investigations, but they can be subject to sources of error. These may include both mechanical and electrical vibrations and noise. Electrical noise is typically very high-frequency noise, which should automatically be filtered away using the band-pass filter described in Section 4.4. Mechanical noise is typically linked to the eigenfrequencies of the rig, and force-frequency components located in close proximity to the rig's eigenfrequencies will experience amp-

lification. It is essential that the results presented are not close to these eigenfrequencies in order to ensure the reliability of the experimental data. Sources of vibrations may also arise from external factors, such as nearby machinery. This was experienced when vibrations from the cavitation lab on the above floor were induced. These vibrations can introduce measurement errors and interfere with the accuracy of the results.

Worn sensors and springs in experimental rigs may lead to sources of error in scientific experiments. Over time, these components may degrade and become less sensitive. This might in turn lead to inaccurate measurements of physical quantities. Additionally, old sensors and springs may not respond consistently to changes in the environment, leading to variability across experiments. This can be problematic when trying to replicate experiments. Furthermore, worn springs may not provide consistent force, leading to imprecise measurements and reduced experimental accuracy. The position sensor in particular was found to give artificially high and spurious results when responding to oscillation starts and stops.

The tank is usually filled up with water from the cavitation lab. However, the last few tests of the experiments conducted in the spring were run with the tank partially filled with tap water due to maintenance in the cavitation lab. This water will for instance not hold the same concentration of chlorine, which is expected to alter the water's properties.

# Experimental Post-Processing

This section presents the primary workflow and post-processing procedures for the two experimental tests carried out. A substantial amount of data has been acquired, and a significant aspect of this work has therefore been to post-process this data. All post-processing was conducted by creating various scripts and functions using Python. The data is stored as binary files with the default sampling rate of 200Hz, and later converted to Matlab format.

## 4.1 Locate KC Number

The data-logging system and oscillator are not initiated simultaneously when a test is commenced. Consequently, the period of inactivity prior to the first oscillation may differ across tests. To mitigate this, a Python function is applied to each test to record the start time. This time is determined by identifying when the rig position reaches 1% of the amplitude at  $KC = 1$ .

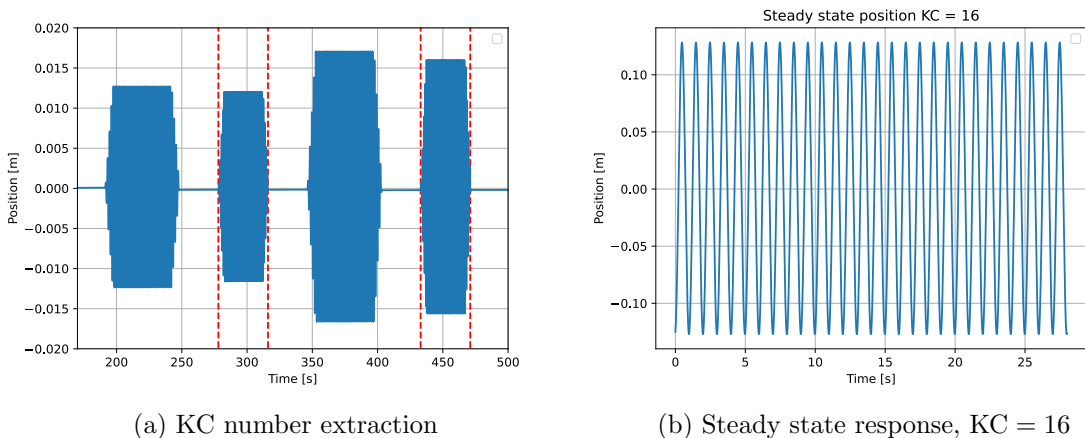


Figure 4.1: Example of KC number extraction and corresponding steady-state responses. The stapled red lines indicate the start and end times of the desired KC number.

The testing procedure remains uniform for all tests, ensuring that the location of each KC



number is precisely known once the start time is recorded. By excluding the four ramp-up and ramp-down periods, the steady-state response for each KC number is then readily extracted. A visual example is provided by Figure 4.1. The first and second experiments have slightly different testing procedures, where the first also tests for KC increments of 0.5 and  $T = 1.5$ s. Therefore, the increments between each KC number are slightly different, though follow the same analogy.

## 4.2 Synchronization

The start times as described in Section 4.1 may be affected by noise or other errors. Although suitable to give an approximate start time for the rig and empty rig, a more sophisticated synchronization scheme is needed. Euclidean distance is used for this endeavor.

Euclidean distance is the L2 norm of the difference between two vectors, and can subsequently be considered a special case of the L2 norm. The expression for the Euclidean error can be written as

$$\epsilon = \sqrt{\sum_{i=1}^{f \cdot T} (P_i^1 - P_i^0)^2}, \quad (4.1)$$

where  $P^1$  is the rig position of the case,  $P^0$  is the empty rig position and  $f$  is the sampling frequency. We can reduce the lag between the two by incrementally shifting the empty rig position along the horizontal axis and recording the corresponding euclidean distance or error. By identifying the shift which results in the lowest error, we can determine the optimal position of the empty rig. In addition, the empty rig position is the only shifted series and only along the horizontal axis. An artificial shift is therefore subtracted initially to ensure that the empty rig is lagging. This artificial shift is subtracted again at the end to get the actual shift.

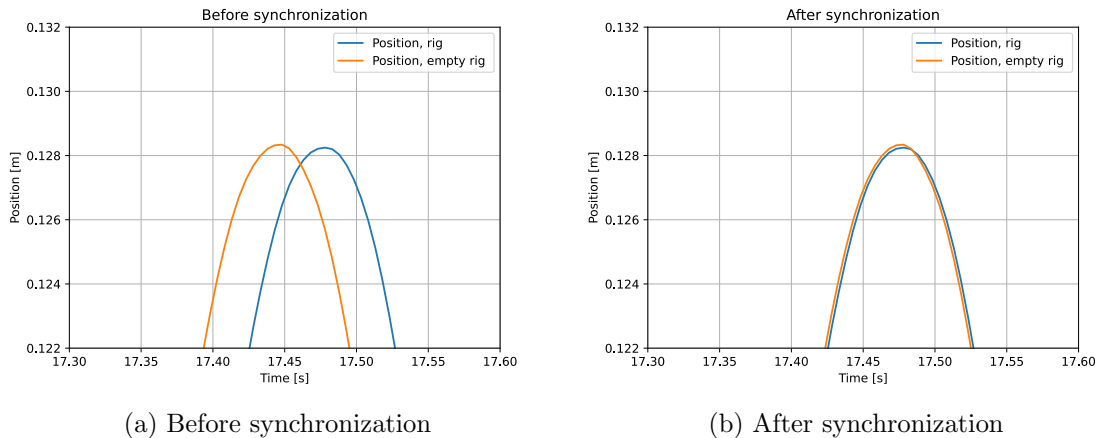


Figure 4.2: Illustration of a local oscillation peak before and after being synchronized. The empty rig position is shifted along the horizontal axis to provide the best fit over one oscillation period.

The steady state responses are extracted as described in Section 4.1, and the mean of the

two time-series are subtracted to ensure zero mean oscillation. By evaluating the sum in Equation (4.2) over only one period, we avoid finding several shifts that satisfy a minimum error. This ensure that the rig and empty rig are locked onto the correct peak, and not the subsequent one.

### 4.3 Rig and Acceleration Subtraction

The rig itself dominates the measured forces from the raw data created during the experiments. In order to isolate the hydrodynamic forces acting on the cylinders, the empty rig forces need to be subtracted from the measured data on each case. The end goal of the procedures described in Section 4.1 and Section 4.2 is therefore to subtract the empty rig forces from the actual case at corresponding times. This is written as

$$F_{net} = F_{measured} - F_{emptyrig}. \quad (4.2)$$

Since the actuator oscillates the cylinders vertically, a mass force will also act on the cylinders in  $z$ -direction. This force also needs to be subtracted from the measured data. The total force then becomes

$$F_{net} = F_{measured} - F_{emptyrig} - m_{cyl}a_{measured}, \quad (4.3)$$

where  $m_{cyl}$  is the cylinder mass and  $a_{measured}$  is the measured acceleration. The result of this operation isolates the hydrodynamic damping and added mass forces.

### 4.4 Band-Pass Filtering

After synchronizing the results with the empty rig, locating each KC number, and isolating the hydrodynamic forces, the data is now ready for filtering. A band-pass filter is used for the purposes of this thesis. A band-pass filter is a device that passes frequencies within a range whilst attenuating frequencies outside the range. A visual example of prior and post-filtration is provided by Figure 4.3.

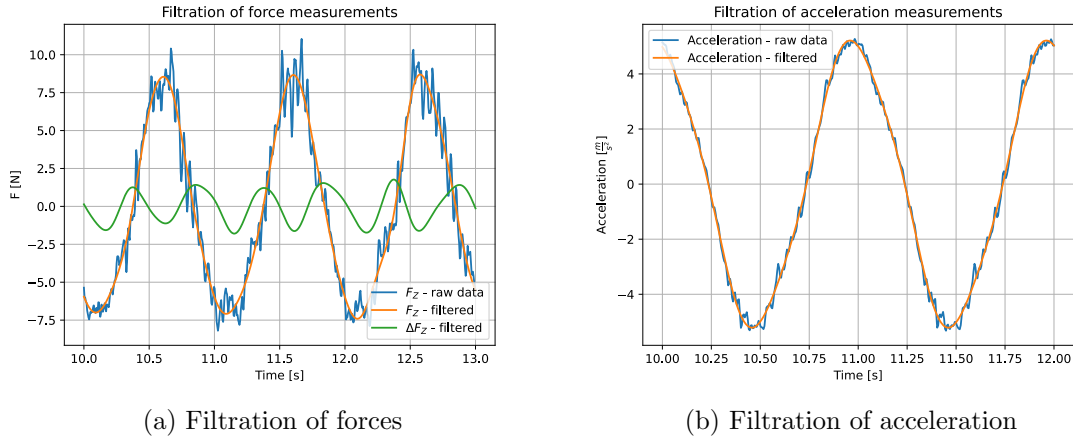


Figure 4.3: Example illustration of force and acceleration results before and after noise attenuation.

The end goal of the filtration is to attenuate the noise from the physical force signal. Noise typically comes from resonance from the rig itself, as electrical noise is located at higher frequencies. A broad-banded Fourier spectra in-between integer frequencies can indicate the presence of noise.

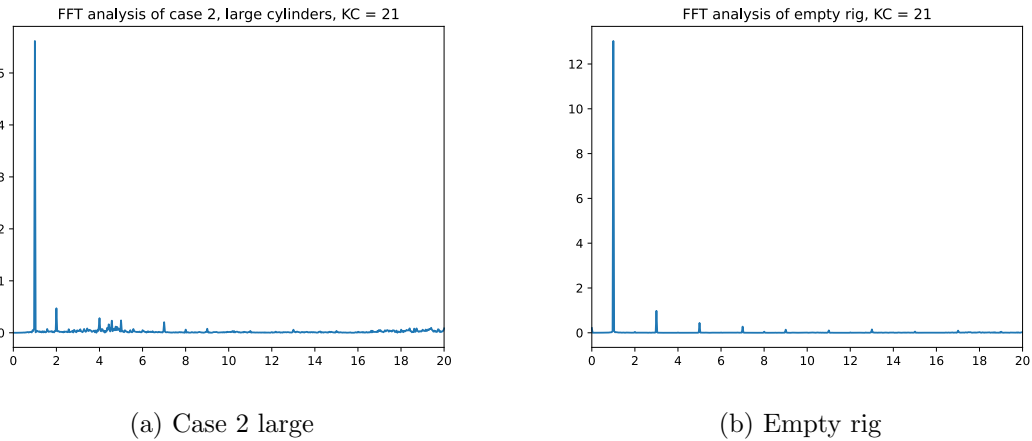


Figure 4.4: Fourier analysis of  $F_Z$  measurements on the outer plate. The empty rig shows clear peaks for odd frequencies, while signs of noise are shown around  $f = 4 - 5\text{Hz}$  with cylinders.

Fourier plots of the empty rig and with large cylinders attached are shown in Figure 4.4. Clear and pronounced peaks are observed for odd frequencies on the empty rig in Figure 4.4b. Indication of noise in the range of 4 and 5 Hz can be seen in Figure 4.4a. We can explain this observation by relating it to the eigenfrequency of a simple harmonic oscillator

$$\omega_0 = \sqrt{\frac{k}{m}}, \quad (4.4)$$

where  $k$  is the stiffness and  $m$  is the mass. By attaching cylinders, or increasing cylinder lengths, the mass of the system should increase. Subsequently, the eigenfrequencies of the system should be shifted further towards the left.

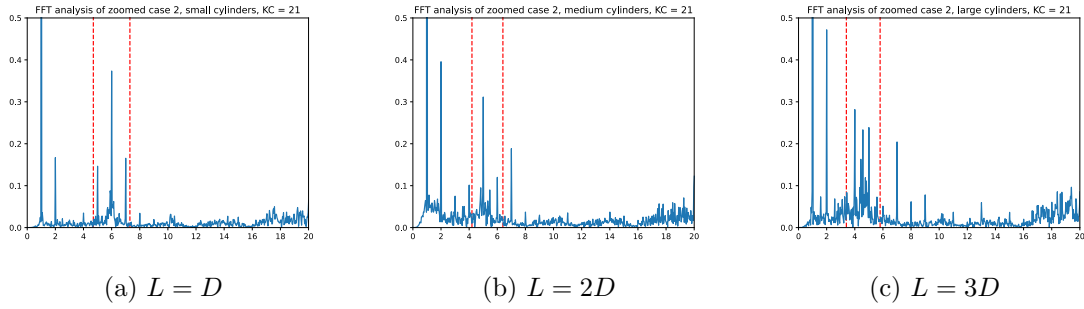


Figure 4.5: FFT comparison of different cylinder lengths, where the stapled red lines indicate the approximate noise range from the rig’s eigenfrequencies. The range is shifted towards the physical range when mass is added.

It is clear from Figure 4.5 that the noise frequencies from the rig eigenperiods are shifted more into the physical domain when larger cylinders are introduced at about 4.5Hz. This is consistent with the findings in Section 3.4. Unfortunately, the rig noise is shifted far enough to affect the  $4\omega$  force contributions, giving rise to spurious results at this frequency for Case 1 and 2 with large cylinders.  $4\omega$  results should be discarded for these cases. This also unfortunately makes evaluating Case 3 difficult, and is subsequently neglected in this thesis.

## 4.5 Harmonic Component Extraction

The harmonic components of the force signal are exposed and isolated by using the band-pass filter from Section 4.4 and setting its range to filter around the harmonic frequency. Each harmonic component is stored as its own time series and analyzed separately. The harmonic amplitude is then determined by subtracting the average minima from the average maxima and dividing by 2.

## 4.6 Nondimensionalization

Although only the cylinder lengths  $L$  were changed during the experiments, both  $L$  and  $D$  are presumed to be subject to change in practical applications or further research. A non-dimensional factor is introduced to present scalable results, make result comparison between cases easier and keep with the established convention by Reiten and Kristiansen [19]. The resulting non-dimensionalization can be written as

$$\frac{FT^2}{\rho LD^3} \left[ \frac{\frac{kg \cdot m}{s^2} \cdot s^2}{\frac{kg}{m^3} \cdot m^3 \cdot m} \right] \implies [-]. \quad (4.5)$$

## Potential Flow Analysis - Wadam

Wadam is a hydrodynamic analysis program made for calculating wave-structure interaction for fixed and floating structures. The program applies Airy wave theory and linear frequency domain methods to solve the 3D radiation and diffraction problem, which is automatically included in the analysis. HydroD is used to execute the Wadam analysis and is also where the environment is modeled. To perform the hydrodynamic analysis, a structure is needed, and Wadam requires a panel model of this structure. For this endeavor, GeniE will be used.

### 5.1 Panel Model Setup

The first step is to create a panel model for the hydrodynamic analysis. GeniE is a structural modeling program that can create panel models and export them as FEM files. Both GeniE and Wadam, are developed by DNV and are part of the Sesam package, so they are fully compatible. GeniE is therefore a good choice for creating the panel model.

The Wadam analysis is used to solve the radiation problem and calculate the excitation forces. These problems only depend on the structure's geometry and not on parameters that would be important for structural analysis, such as plate thickness or material. Therefore, only the structure geometry needs to be modelled. We want to compare the exciting and added mass forces from Wadam with the experimental results. The panel model needs to represent the same square cylinders used in the experiments if the diffraction and radiation results are to be used. For this thesis, cases 1, 2, and 3 have been analyzed for all cylinder lengths.

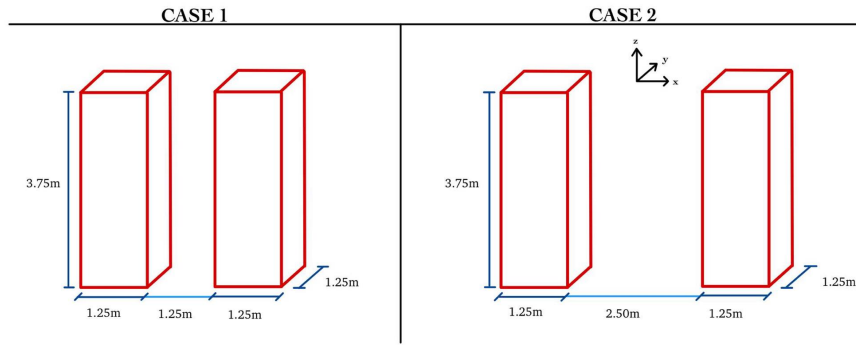


Figure 5.1: Sketch of the modeling strategy in GeniE. All cases in Wadam will be modeled around origo with respect to  $x$  and  $y$ , while only negative  $z$  values are modeled.

It is important to ensure that the coordinate systems used in GeniE and HydroD correspond with each other when exporting the panel model from GeniE to HydroD. If they do not match, the model's translation may be unfavorable when importing it into HydroD, which will produce incorrect results. To prevent this, the panel model geometry is always modeled around the global origin in GeniE as shown in Figure 5.1. Additionally, we are only interested in the wet surface of the model, so the model is only modeled below the waterline. HydroD have symmetry options that can mirror a structure around the  $xz$  and  $yz$  plane. This means that only 25% of the model needs to be modeled in practice, shortening the computation time and memory needed.

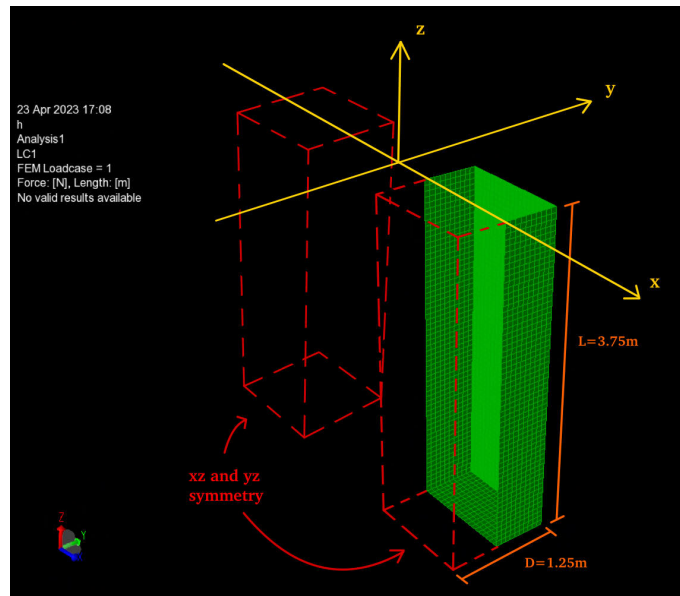


Figure 5.2: Sketch of the resulting model for Case 1 with large cylinders in GeniE. Staped red lines indicate the whole structure when double symmetry is applied in HydroD.

## 5.2 Wadam Setup

In addition to the panel model, the Wadam analysis requires an environment to run. This environment is defined in HydroD, which is the program used to create and run the Wadam analysis. The easiest way to create the analysis is to use a Wadam wizard, which

will guide you through the required steps. The Wadam mass model is set up with scales and data for a full-size module.

The environmental parameters are set to match the experimental setup. This mostly involves the water density  $\rho$ , gravity  $g$  and viscosity  $\nu$ . The panel model mass and the center of gravity are explicitly specified in HydroD. As the radiation and excitation forces are frequency-dependent, the Wadam and experimental results will not correspond if the numerical frequencies match those used in the experiments. The environmental variables used are given in Table 5.1 and Table 5.2.

Table 5.1: Definition of environment in HydroD

$g$ [m/s <sup>2</sup> ]	depth [m]	$\rho$ [kg/m <sup>3</sup> ]	$\nu$ [m <sup>2</sup> /s]
9.8066	300	1000	1.19E-06

Table 5.2: Wadam mass model, single large cylinder

$m$ [kg]	$COG_x$ [m]	$COG_y$ [m]	$COG_z$ [m]
5859.4	0	0	1.875

### 5.3 Mesh Refinement Analysis

Mesh refinement analysis is crucial in improving the accuracy of numerical simulations used in engineering design and analysis. In hydrodynamic simulations, a refined mesh is essential to capture complex flow behaviors and accurately predict hydrodynamic loads. In this case, a mesh refinement analysis was performed on a single cylinder using Wadam and GeniE to improve the accuracy of the hydrodynamic loads. The cylinder was discretized by splitting  $D$  into a number of elements. The number of elements used for the analysis varied between five, ten, twenty, and thirty elements. Added mass and excitation forces were calculated using Wadam for these numbers of elements in the mesh.

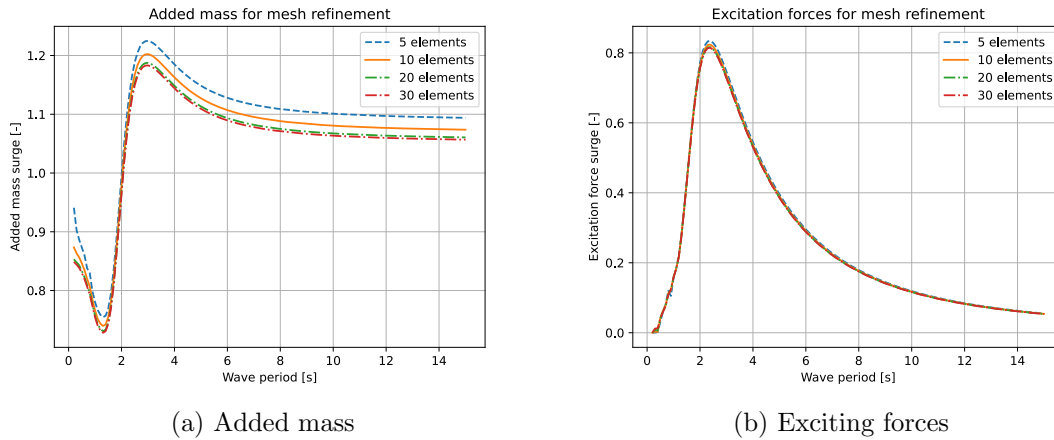


Figure 5.3: Results for added mass and excitation forces for mesh refinement analysis in surge. Added mass coefficient converges at about 20 elements, while excitation force is largely unaffected.

The results of the mesh refinement analysis are presented in Figure 5.3, and shows that the results converged at around twenty elements. It can be observed that as the number of elements is increased, the added mass becomes more accurate and converge while excitation forces stay largely unaffected. The convergence of the results can be observed for about twenty elements, and further refinement of the mesh does not significantly improve the accuracy of the results. Therefore, twenty elements were chosen for subsequent analysis due to the trade-off between accuracy and computational time.

## 5.4 Added Mass

The added mass output from Wadam is automatically normalized by mass displacement  $\rho V$ . It is also given as a per-wave period mass matrix because added mass is frequency-dependent. To verify the Wadam results, we can compare them to the added mass coefficients for strip theory and the coefficients provided in DNV-RP-C205 [4]. Both tables are provided by Figure A.1 and Figure A.2. While the coefficient for strip theory can be read as  $C_a^o = 1.51$ , no table for a right square cylinder in vertical motion is provided. We use the data for a circular cylinder in Figure A.1 and interpolate in order to get the reduction from the infinite value. Furthermore, we assume that this reduction is equivalent for a square cylinder and scale the reduction with value for strip theory. This yields

$$C_a^o = 1.51 \left( y_0 + \frac{y_1 - y_0}{x_1 - x_0} (x - x_0) \right), \quad (5.1)$$

where  $y_0$  and  $y_1$  are the coefficients, and  $x_0$  and  $x_1$  are  $b/2a$  between point 0 and 1. Furthermore, the coefficients from the Wadam results should use a circular reference area to keep the comparison consistent. Plotting the results from Wadam against the added mass coefficients for strip theory and the result from Equation (5.1) for a large cylinder yields Figure 5.4a.

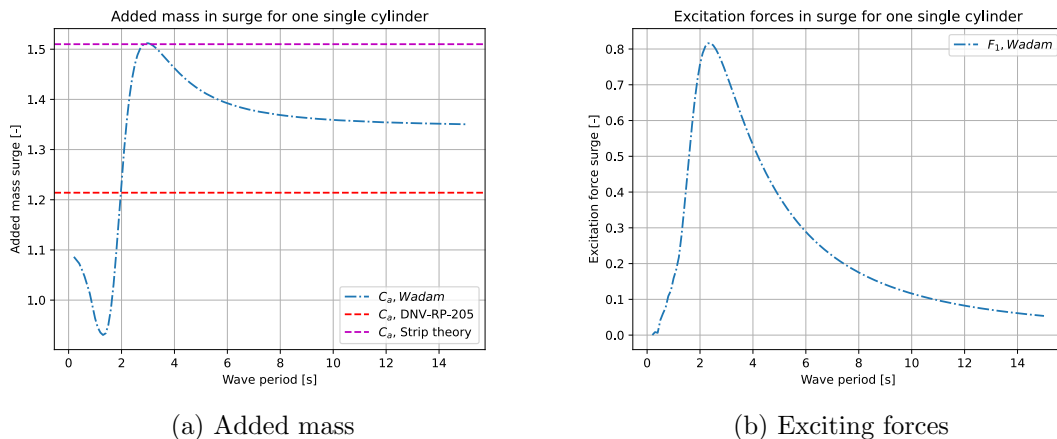


Figure 5.4: Non-dimensional added mass values from Wadam plotted against theoretical added mass, and non-dimensional exciting force of a single large cylinder.

The results show discrepancies between the asymptotic added mass from Wadam and the other added mass coefficients. It is known that strip theory added mass will overestimate the actual added mass [4], but the results from DNV-RP-C205 are harder to explain. It is



possible that using circular cylinder interpolation directly with infinite values for a square is not valid. However, we will use this anyway since we lack standards for square cylinders. The added mass results appear to be "independent" of time at about  $T = 10$ s as the added mass coefficient is close to the asymptotic value at that period. Overall, the results for the reference case show reasonable enough correspondence with the theory.

## 5.5 Excitation Loads

The excitation forces from Wadam are the integrated pressure over the body, given as a per period, wavelength, and heading angle value. They are expressed as complex numbers with both real and imaginary contributions. The corresponding absolute value and phase angle are also provided. As such, the excitation forces from Wadam can be expressed as

$$F_{11}^{exe} = re^{i\phi} = r(\cos(\phi) + i\sin(\phi)), \quad (5.2)$$

where  $r$  is the magnitude or length of the complex number.

As outlined in Section 2.2, the excitation forces are expressed as the sum of the Froude-Kriloff forces and the diffraction problem. To separate the two and acquire an expression for the diffraction force, we can solve

$$F_{FK}^{exe} = \rho \int_{S_0} \frac{\partial \phi_0}{\partial t} n_i dS, \quad (5.3)$$

and subtract the solution for the Froude-Kriloff force from the total excitation force. This will become relevant to the experimental post-processing when the diffraction force from Wadam is to be compared to the experimental results. Preliminary results for the exciting forces of the single cylinder are also presented in Figure 5.4b.

## 5.6 Presentation of Numerical Results

The end goal of the numerical Wadam simulation is to evaluate the applicability of potential theory when estimating added mass forces. In order to present the results from Wadam in a manner consistent with the nondimensionalization established in Section 4.6, we first start with the inertial term from Equation (2.28).

$$F_I = \rho \frac{\pi D^2 L}{4} C_a^o a(t) \quad (5.4)$$

Furthermore, it is known from Equation (2.12) that the amplitude of the acceleration can be written as  $a = \omega^2 \eta_a$  and that the frequency is equal to  $\omega = \frac{2\pi}{T}$ . The oscillation amplitude  $\eta_a$  can also be expressed by rewriting Equation (2.26) as  $\eta_a = \frac{KCD}{2\pi}$ . We can then rewrite Equation (5.4) as

$$F_I = \rho \frac{\pi D^2 L}{4} C_a^o \frac{(2\pi)^2 KCD}{T^2} \frac{1}{2\pi}, \quad (5.5)$$

which can be added together to

$$F_I = \frac{1}{8}\rho D^3 L C_a^o \frac{(2\pi)^2}{T^2} KC. \quad (5.6)$$

The added mass coefficients found from Wadam will be directly related to the actual geometry of the analysis, which for this instance is a square. Added mass coefficients in the literature are typically normalized by the displaced mass of a circular cylinder and are denoted here as  $C_a^o$ . The relation between the circle and square can be written as  $C_a^o = \frac{4}{\pi} C_a^\square$ , where  $C_a^\square$  is the coefficient from Wadam. Using this expression with the nondimensionalization from Section 4.6, we get the

$$\frac{F_I T^2}{\rho L D^3} = 2\pi C_a^\square KC. \quad (5.7)$$

This expression yields a linear relationship between the inertial forces and the KC number. Comparing this linear trend from Wadam with the results for diffraction forces from the experiments is especially important. A discrepancy between the two indicates that separation affects the inertial force contribution. An example of this linear trend is provided in Figure 5.5. The assumptions used are that surface acceleration and  $C_a^\square$  at large wave periods are representative of the entire case.

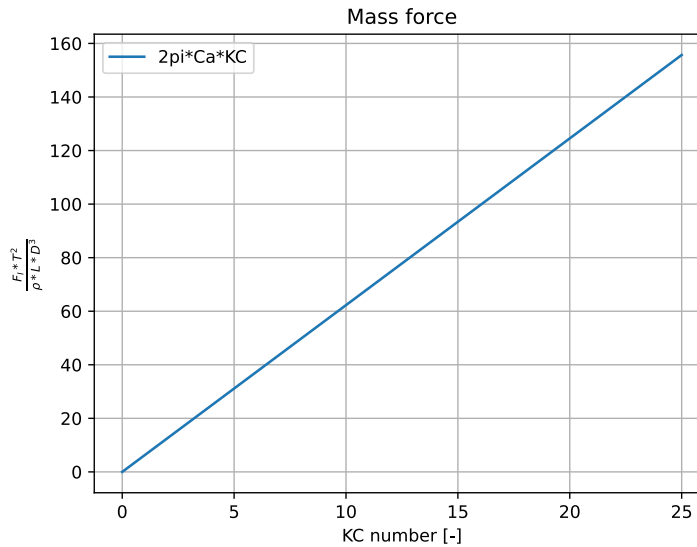


Figure 5.5: Example illustration of how the results from Wadam are presented as a linear function of the KC number using Equation (5.7). This specific plot depicts the Wadam results for Case 2 ( $\frac{L}{D} = 3$ ).

## Results and Discussions

The following chapter presents the results of the experimental investigations and the numerical Wadam simulations. Firstly, the findings from the results for tandem arrangement will be presented and discussed. The KC number and spacing ratio dependency are the main parameters related to the tandem investigation. These investigations are also supplemented by the Wadam analysis. Following tandem is the staggered arrangement, where the effects of the inflow angle  $\theta$  are the main topic of discussion. Each arrangement corresponds to a separate experimental investigation, which means that the two experiments are subsequently presented and discussed in chronological order. The chapter is completed with separate discussions on the  $2\omega$  responses, the applicability of the Morison equation, and some summarizing comments.

### 6.1 Tandem Arrangement

Results for tandem arrangement are the product of the experimental investigation of the cases described in Figure 3.7, conducted during the autumn. They are in general presented as the force measurements  $F_z$  on each cylinder and the difference force  $\Delta F_z$ . In the experimental setup Cylinder 1 is defined as the bottom cylinder, and Cylinder 2 as the top cylinder. Consequently, the difference force is defined as the subtraction of Cylinder 1 from Cylinder 2. Any time series provided are the band-passed force measurements while KC dependent plots are made by extracting the different harmonic components from the force.

#### 6.1.1 Case 1

Until now, the cylinder configurations have solely been described by the cases described in Section 3.3 and Figure 3.7. From this point forward, the use of the word 'cases' specifically refers to the experimental implementation and post-processing, while the results will be presented and discussed using spacing ratio  $\frac{S}{D}$ . Three KC numbers are selected to give a representative view of the force development across the KC number range. A time series of  $F_z$  and  $\Delta F_z$  for  $\frac{S}{D} = 1$ , for  $5T$  is provided in Figure 6.1, Figure 6.2 and Figure 6.3.

It quickly becomes apparent from these figures that higher order frequency contributions are more relevant for  $L = D$ , compared to  $L = 2D$  and  $L = 3D$ . The likely explanation

for this phenomenon is the vortex-shedding frequencies at the 3D ends. Li wrote that the  $St$  numbers of 3D cylinders are more broad-banded at the base and ends of the cylinders, with pronounced peaks towards the center [13]. This implies that the end effects should introduce a larger range of higher-order frequencies compared to 2D or infinite cylinders. While  $L$  is incrementally increased, the cross-section and end effects should stay unchanged. The higher-order force components should therefore be more smeared out when increasing  $L$ , as the center shedding frequency peaks become more dominating.

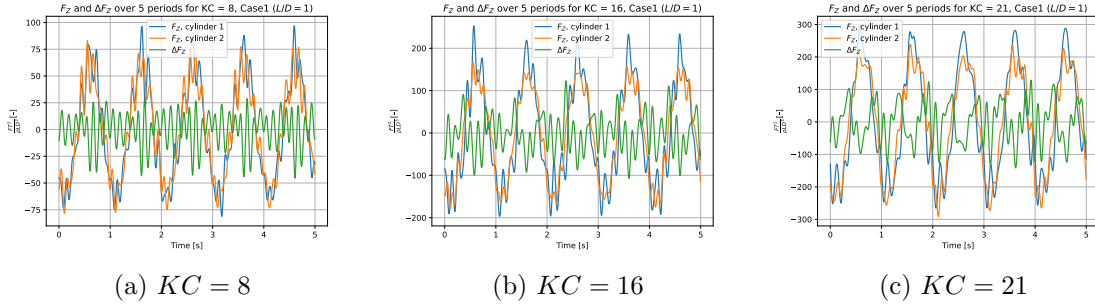


Figure 6.1: Time series of  $F_z$  and  $\Delta F_z$  for Case 1 ( $\frac{S}{D} = 1$ ) and  $L = D$  across three representative  $KC$  numbers.

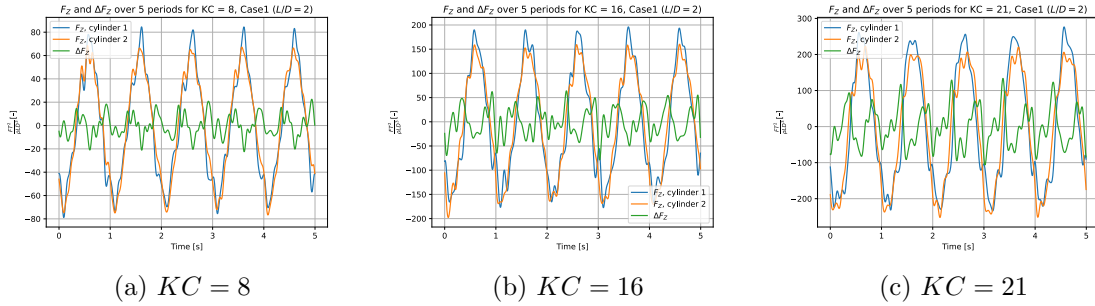


Figure 6.2: Time series of  $F_z$  and  $\Delta F_z$  for Case 1 ( $\frac{S}{D} = 1$ ) and  $L = 2D$  across three representative  $KC$  numbers.

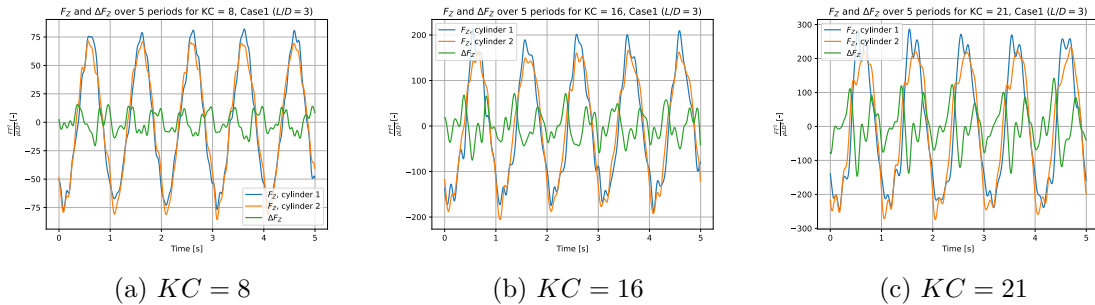


Figure 6.3: Time series of  $F_z$  and  $\Delta F_z$  for Case 1 ( $\frac{S}{D} = 1$ ) and  $L = 3D$  across three representative  $KC$  numbers.

Another interesting finding is that Cylinder 1 consistently experiences larger peaks for  $F_z$  in the positive direction, while Cylinder 2 experiences larger peaks in the negative direction. This indicates a force contribution that acts on each half-cycle during the

oscillation, and that this contribution on Cylinders 1 and 2 acts 180 degrees out of phase from each other. A nonzero mean value should therefore be expected for both cylinders individually.

An additional observation is the development of  $\Delta F_z$  when increasing the KC number. Clear and pronounced oscillation peaks show that  $\Delta F_z$  becomes increasingly dominated by  $2\omega$  frequency amplitudes at higher KC numbers. The exception is at  $L = D$ , where even larger frequencies seem present. The dominating frequency component seems to be  $2\omega$  by counting peaks over one period  $T$ , which is consistent with the findings of Reiten presented in Section 1.4.

It becomes evident that increasing  $L$  has little impact on the measured force range when considering the non-dimensionalized values. This observation suggests that the force exerted by the cylinders is primarily dependent on nondimensional factors. As previously stated, it is likely that the primary effect of a shorter cylinder length is the introduction of more high-frequency forces. The 3D end effects should be further investigated in future studies in order to quantify them.

Due to the clear presence of higher-order frequency contributions in the time series, it is appropriate to separate and analyze the harmonic force components separately. Trends in the separate force harmonics are likely to be explained by different physical phenomena. Using the same approach described in Section 4.5, the non-dimensional harmonic amplitudes are extracted and shown in Figure 6.4 as a function of the KC number.

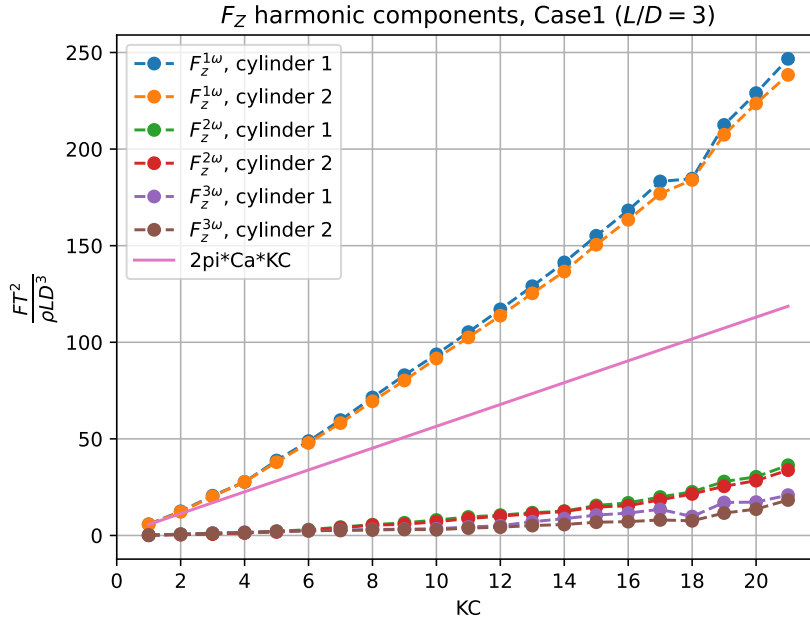


Figure 6.4: The harmonic force component amplitudes measured for Case 1 ( $\frac{S}{D} = 1$ ) and  $L = 3D$ . Both cylinders are included along with the equivalent Wadam results.  $4\omega$  components are neglected due to noise concerns.

The first takeaway is that the  $1\omega$  force component dominates for both cylinders. This is expected considering that the actuator also oscillates with a frequency of  $1\omega$ . A much more interesting observation is how  $F_z^{1\omega}$  compares to the results from Wadam. It can be seen that these two correspond quite well until  $KC = 4$ , before  $F_z^{1\omega}$  diverges more for

higher KC numbers. There are two possible explanations for this nonlinear trend. The first possible explanation is that viscous forces dominate more for higher KC numbers and that the inertial forces from Wadam are a better fit to the added mass force from the experiments isolated. The second is that vortex shedding affects the experimental mass force. This is further discussed in Section 6.1.3, where the experimental added mass and damping force contributions are separated.

Furthermore, this nonlinear trend is shared by the  $2\omega$  and  $3\omega$  forces. Higher-order contributions are usually related to nonlinear or stochastic problems, so this is not that surprising. A more notable observation is that these contributions are not negligible at high KC numbers. Adding  $F_z^{2\omega}$  to  $F_z^{3\omega}$  with  $KC = 21$  sums to approximately 50, which is 20% relative to  $F_z^{1\omega}$ . This means that although  $F_z^{1\omega}$  dominates the force signal, the higher-order contributions still provide a noticeable effect.

Lastly, the force measurements for Cylinder 1 are slightly higher than those for Cylinder 2 for all  $\omega$  contributions. As mentioned in Section 3.5, the experiments are assumed to be in deep water conditions. If this is not the case, and Cylinder 2 experiences larger boundary interaction, it might explain the discrepancies in harmonic amplitudes. These disturbances seem small enough to not significantly impact the results, with an amplitude difference less than 10 at most. They are nonetheless worth mentioning and should be considered for future experiments. This might explain  $\Delta F_Z^{1\omega}$  presence, but no other significant impact is identified on the difference forces, which are presented in Figure 6.5.

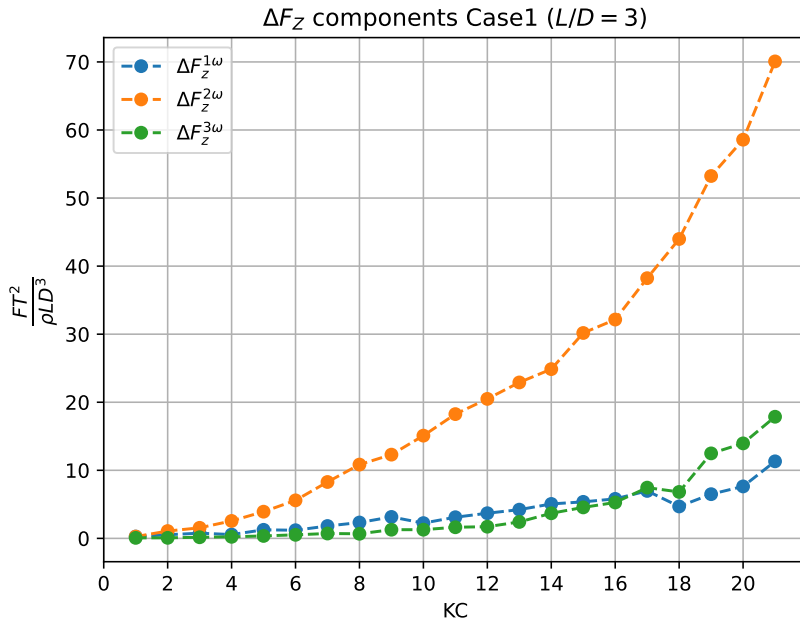


Figure 6.5: Force amplitudes of  $\Delta F_Z$  for Case 1 ( $\frac{S}{D} = 1$ ) and  $L = 3D$ .

The first interesting observation is the development of the importance of the  $2\omega$  contribution going from Figure 6.4 to Figure 6.5. It is clear that the difference forces are dominated by  $\Delta F_Z^{2\omega}$ . The  $\Delta F_Z^{2\omega}$  contribution reaches 70 at  $KC = 21$ , making it a significant part of the force image. Difference forces are important to evaluate, as they need to be taken up in either the mooring system or in hinges to prevent drift. The fact that the difference force is dominated by  $\Delta F_Z^{2\omega}$  may pose fatigue problems for a potential hinge, as the difference force then becomes predominately  $2\omega$ . In other words, the hinges will then experience

twice as many force oscillations as the dominating forces on the rest of the structure.

Probably the most interesting takeaway from Figure 6.5 is the values of  $\Delta F_z^{2\omega}$  compared to the  $2\omega$  forces in Figure 6.4. Using  $KC = 21$  as an example, it can be seen that  $F_z^{2\omega} \approx 35$  for both Cylinder 1 and Cylinder 2. The  $2\omega$  difference force amplitude is 70 at the same  $KC$  number, meaning that  $\Delta F_z^{2\omega}$  is double the values for the individual cylinders. This implies that the  $2\omega$  forces that act on the two cylinders are 180 degrees out of phase from each other, leading to a sign shift when taking the difference. Any nonlinearity acting on the cylinders will subsequently become exacerbated in  $\Delta F_z^{2\omega}$ . This is in contrast to the  $1\omega$  component which is largely canceled out during the subtraction. The  $2\omega$  forces are discussed more in-depth in Section 6.1.4 and Section 6.3.

Only time series and the amplitudes of the harmonic components have been evaluated up until now. In an effort to bolster the understanding of the hydrodynamic forces, plotting the added mass and damping coefficients is a powerful tool. They provide a clue to the development of the forces at high  $KC$  numbers and locate any trends. Furthermore, by separating the mass and damping forces, determining the point where one overtakes the other becomes possible. The added mass and damping are calculated using Equation (2.16) and Equation (2.17) with the measured acceleration and its corresponding velocity using a forward Euler scheme on the acceleration, before nondimensionalized. Figure 6.6 presents the  $1\omega$  mass and damping force coefficients from the experiments for  $\frac{S}{D} = 1$ , along with supplementary values from Wadam, DNV-RP-C205, and strip theory. The values from Wadam and DNV-RP-C205 are only relatable to the mass coefficient  $C_a^{1\omega}$ . Due to long wave approximation, these values should correspond with  $KC = 0$ . The experimental results for  $C_a^{1\omega}$  are in good agreement with the numerical results from Wadam, as they lie closely together at  $KC = 0$ . The DNV-RP-C205 line slightly overshoots the Wadam line, which might be because the method described in section 5.4 is derived from a single cylinder.

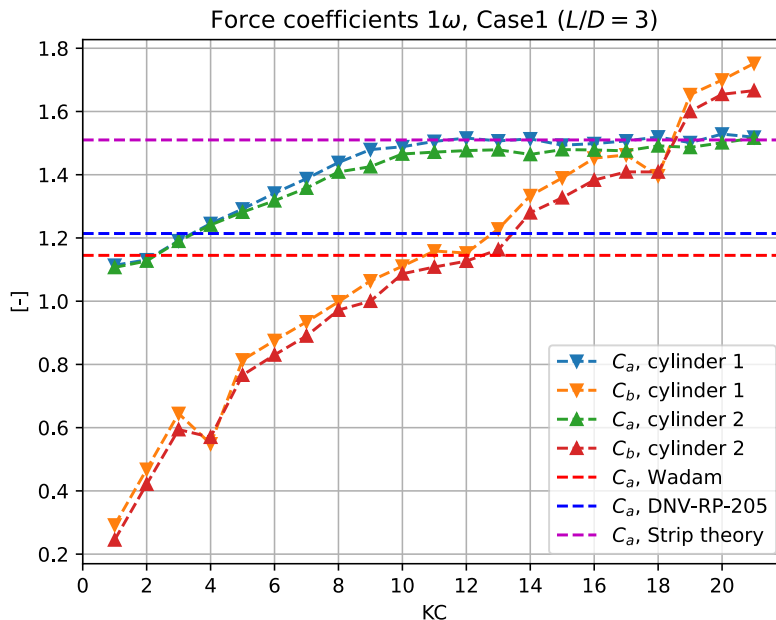


Figure 6.6:  $1\omega$  force coefficients for Case 1 ( $\frac{S}{D} = 1$ ) and  $L = 3D$ . The measured force coefficients are plotted against strip theory, the interpolated values for DNV-RP-C205 and the coefficients from Wadam.

It is clear that both  $C_a^{1\omega}$  and  $C_b^{1\omega}$  is highly dependent on the KC number. While  $C_b^{1\omega}$  starts off close to zero and increases steadily,  $C_a^{1\omega}$  remains much more consistent throughout the KC range. Unlike  $C_b^{1\omega}$ ,  $C_a^{1\omega}$  seems to stay mostly independent of the KC number after reaching  $KC = 10$ . This leads to the damping coefficient overtaking the added mass coefficient at about  $KC = 18$ . The added mass force coefficient is expected to be larger than the damping coefficient at lower KC numbers, while damping should increase in relevance at higher KC numbers when viscous forces become more prevalent. As mentioned earlier, the Wadam added mass coefficient corresponds quite well with the first experimental added mass coefficient. This is a good indication that the numerical model in Wadam is set up properly.

A more thorough investigation of the relative importance between the inertial and damping forces is appropriate. This will help in determining which governing physical phenomena become significant at different KC numbers. The relative importance between the inertial coefficient and damping coefficient,  $\frac{C_b^{1\omega}}{C_a^{1\omega}}$ , should be evaluated. Furthermore, the damping force should be evaluated as the percentwise contribution to the total force amplitude. Both of these are presented in Figure 6.7. Interestingly, the damping coefficients seem to overtake the added mass coefficients at  $KC = 18$ . This is a slightly higher KC number than the expected value where damping coefficients overtake added mass coefficients for a single circular cylinder at about  $KC = 10 - 14$ . A possible explanation is that the interaction between the cylinders, especially the fluid entrainment of the fluid in the cylinder gap, increases the relevance of the inertial force. It is also possible that vortex shedding of the upstream cylinder and reattachment on the downstream cylinder lowers the damping relevance.

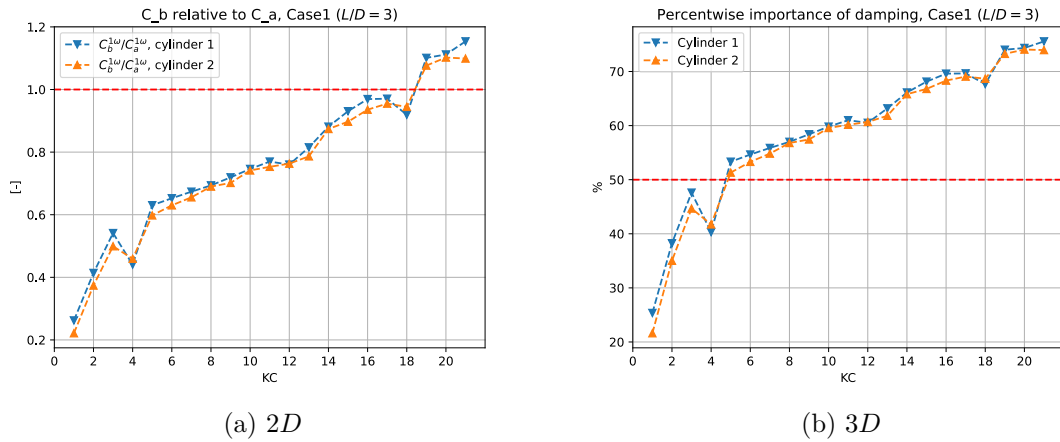


Figure 6.7: Relative importance of the force coefficients for Case 1 ( $\frac{S}{D} = 1$ ) and  $L = 3D$  and percentwise importance of damping in the force amplitude. Red stapled lines indicate the point where damping overtakes the mass force coefficient.

### 6.1.2 Case 2

Case 2 is the experimental testing of cylinders where  $\frac{S}{D} = 2$ , doubling the spacing ratio in Case 1. Due to the double spacing between the two cylinders, wake interaction between the two is expected to reduce going from  $\frac{S}{D} = 1$ . Time series of the same selective KC numbers as before are presented in Figure 6.8, Figure 6.9 and Figure 6.10.

The first introductory observation from these figures is the same as for  $\frac{S}{D} = 1$ . The



forces are more high-frequent for  $L = D$  compared to  $L = 2D$  and  $L = 3D$ . The overall oscillation amplitudes remain largely unaffected when altering the lengths. It is evident that the 3D end effects affect the frequencies, and that a more comprehensive investigation of this phenomenon is needed to quantify these effects.

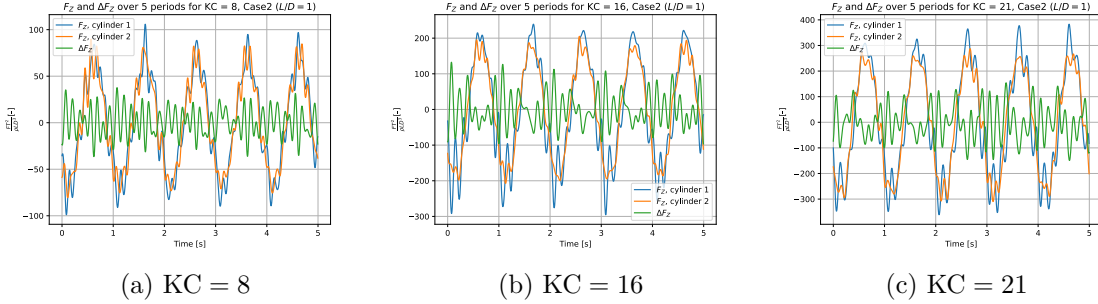


Figure 6.8: Time series of  $F_z$  and  $\Delta F_z$  for Case 2 ( $\frac{S}{D} = 2$ ) and  $L = D$  across three representative KC numbers.

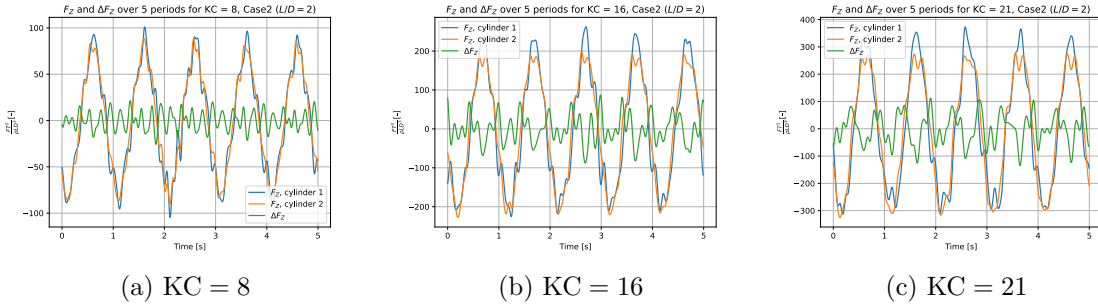


Figure 6.9: Time series of  $F_z$  and  $\Delta F_z$  for Case 2 ( $\frac{S}{D} = 2$ ) and  $L = 2D$  across three representative KC numbers.

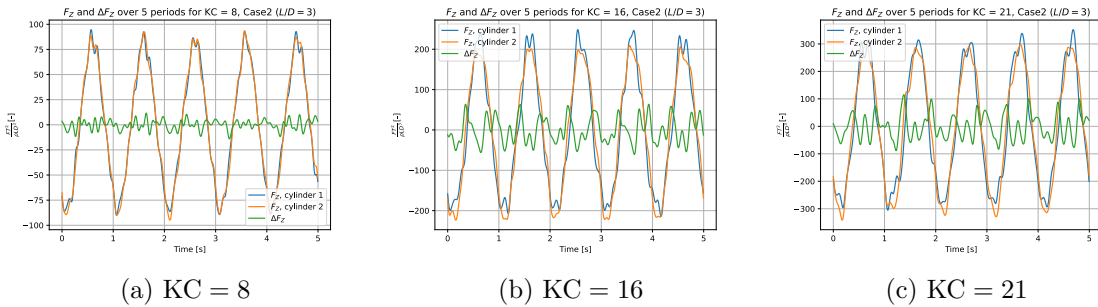


Figure 6.10: Time series of  $F_z$  and  $\Delta F_z$  for Case 2 ( $\frac{S}{D} = 2$ ) and  $L = 3D$  across three representative KC numbers.

There are mainly two takeaways that differentiate these figures from the figures from  $\frac{S}{D} = 1$ . The first is that the general amplitudes of the force series increase when increasing the spacing ratio from  $\frac{S}{D} = 1$  to  $\frac{S}{D} = 2$ . This is in contrast to the  $\Delta F_z$  forces, which appear to require higher KC numbers to develop. An added effect of this is that  $\Delta F_z$  amplitudes do not reach the same levels as for  $\frac{S}{D} = 1$ . The  $\Delta F_z$  amplitudes for spacings  $\frac{S}{D} = 1$  become larger relative to the regular force measurements compared to  $\frac{S}{D} = 2$  as a result.

The second takeaway is that the positive and negative force oscillation peaks of the two cylinders coincide up until higher KC numbers compared to  $\frac{S}{D} = 1$ . Cylinder 1 will have larger positive peaks while Cylinder 2 have larger negative peaks after this KC number, which is the same as before. Any other observations that can be drawn from the time series are otherwise consistent with the findings for  $\frac{S}{D} = 1$ .

The harmonic force amplitudes are extracted as previously for  $\frac{S}{D} = 1$  and presented in Figure 6.11. There are several similarities between the two spacing ratios, including the general nonlinear trends. Likewise, the Wadam results and the first-order forces still correspond well with each other at low KC numbers.

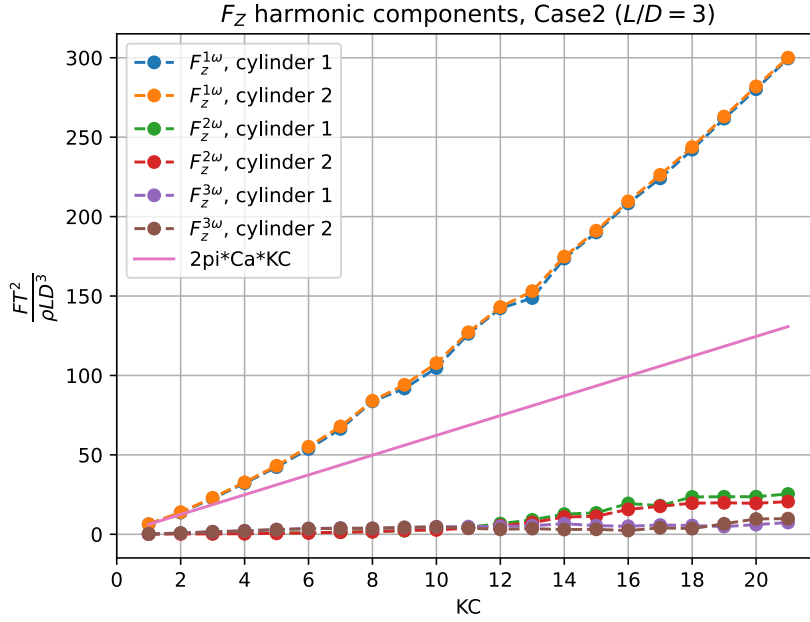


Figure 6.11: The harmonic force component amplitudes measured for Case 2 ( $\frac{S}{D} = 2$ ) and  $L = 3D$ . Both cylinders are included along with the equivalent Wadam results.  $4\omega$  components are neglected due to noise concerns.

Interestingly,  $F_z^{1\omega}$  increased considerably by approximately 50 at  $KC = 21$  when increasing the spacing ratio. Unlike  $F_z^{1\omega}$ , the  $F_z^{2\omega}$  amplitudes decrease when the spacing ratio increases. This further strengthens the theory that the  $2\omega$  force components are mainly a product of the wake interaction between the two bodies. It was observed earlier that the  $F_z^{2\omega}$  forces on the two cylinders appear added together when calculating the difference force for  $\frac{S}{D} = 1$ . Coupled with the reduced measured  $F_z^{2\omega}$  amplitudes, it is therefore expected that the difference force is reduced as well. Figure 6.12 presents the difference forces for  $\frac{S}{D} = 2$ .

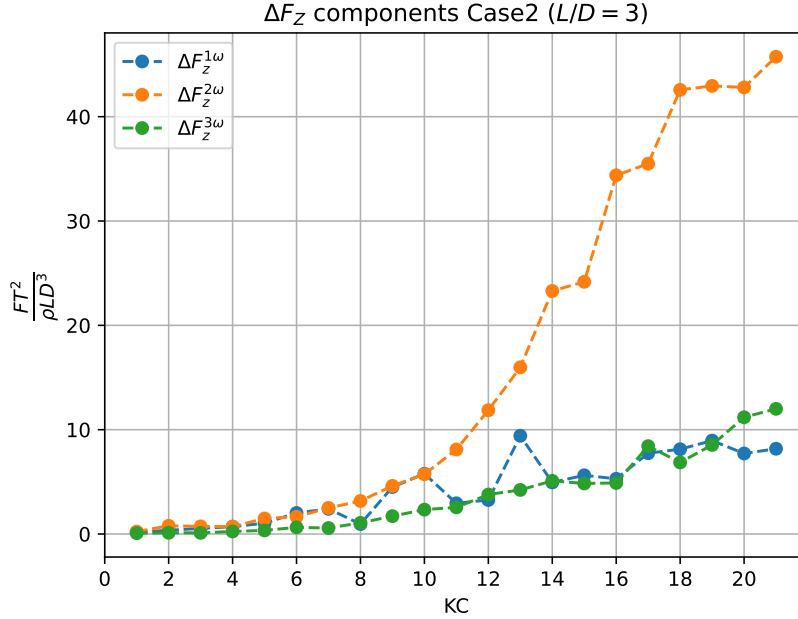


Figure 6.12: Force amplitudes of  $\Delta F_z$  for Case 2 ( $\frac{S}{D} = 2$ ) and  $L = 3D$ .

As expected,  $\Delta F_z$  decreases when the spacing ratio is doubled. The  $2\omega$  difference force is decreased by  $\approx 22$  at  $KC = 21$ , which means that a doubling in spacing ratio did not warrant a halving of  $\Delta F_z^{2\omega}$ . The difference forces are subsequently still a considerable force response that needs to be evaluated and is still dominated by the  $\Delta F_z^{2\omega}$  amplitudes. Considering that the  $1\omega$  amplitudes in Figure 6.11 increases, while the  $2\omega$  difference force decreases, the importance of wake interaction and  $\Delta F_z$  decreases when increasing the spacing ratio. Simultaneously, the forces acting on each individual cylinder should increase in importance.

As the spacing ratio increases from 1 to 2, the  $\Delta F_z^{2\omega}$  pickup begins to exhibit a noticeable shift to later  $KC$  numbers. Previously from Figure 6.5 it is seen that the  $2\omega$  amplitudes completely dominate  $\Delta F_z$  all the way down to  $KC = 5$ . This point is now shifted up to  $KC = 9$  or  $KC = 10$  as shown in Figure 6.12 going to  $\frac{S}{D} = 2$ . Overall, the results for the difference forces shown in Figure 6.5 and Figure 6.12 show that the wake interaction decreases when the spacing ratio increases.

Another interesting observation is the less smooth development of  $\Delta F_z^{2\omega}$  compared to  $\frac{S}{D} = 1$ . Whereas  $\Delta F_z^{2\omega}$  in Figure 6.5 exhibits a strong nonlinear and explosive trend,  $\Delta F_z^{2\omega}$  in Figure 6.12 are slower to develop and have a more uneven curve at larger  $KC$  numbers. An example of this is the plateau that occurs between  $KC = 18$  and  $KC = 20$ , and some smaller ones at  $KC = 14$  and  $KC = 16$ . Compared to  $\frac{S}{D} = 1$ , it may indicate that the rate of increase dissipates with increasing  $KC$  numbers or is just slower in general, but the  $KC$  number range is too small to determine this conclusively. Seeing the difference in the development of  $\Delta F_z$  for more spacing ratios would be interesting, but would require a new set of experiments.

Figure 6.13 presents the first order added mass and damping coefficients for spacing ratio  $\frac{S}{D} = 2$ . As for  $\frac{S}{D} = 1$  in Figure 6.6, the force coefficients exhibit a strong  $KC$  number dependency. The general trends in the two spacing ratios are equal, although the curves seem steeper for  $\frac{S}{D} = 2$ . As mentioned earlier, the forces on the individual cylinders in-

crease going to larger spacing ratios. It is therefore expected that also the non-dimensional force coefficients are larger. The  $C_a^{1\omega}$  from Wadam and DNV-RP-C205 still coincide well with the experiments at  $KC = 0$ .

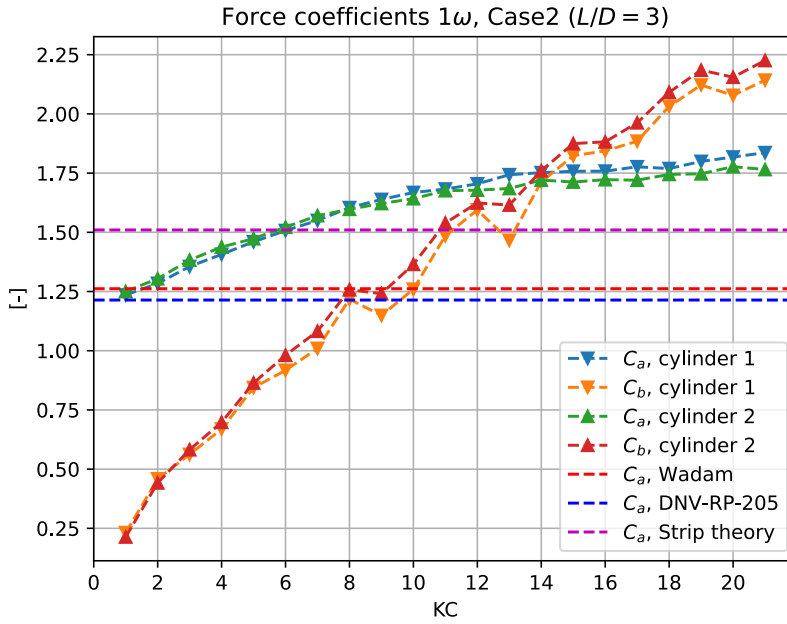


Figure 6.13:  $1\omega$  force coefficients for Case 2 ( $\frac{S}{D} = 2$ ) and  $L = 3D$ . The measured force coefficients are plotted against strip theory, the interpolated values for DNV-RP-C205 and the coefficients from Wadam.

Another observation is that the  $KC$  number at which  $C_b^{1\omega}$  overtakes  $C_a^{1\omega}$  is now shifted to  $KC = 14$ . It appears that the damping forces increase more compared to the added mass force when the spacing ratio is increased. More interestingly, this  $KC$  number is closer to when  $C_b^{1\omega}$  is expected to dominate for a single circular cylinder. This is also shown in Figure 6.14a, which represents the ratio between  $C_b^{1\omega}$  and  $C_a^{1\omega}$ . Furthermore, it is seen in Figure 6.14b that the percentwise importance of damping overtakes added mass at about  $KC = 5$ . This is consistent with the findings of Mentzoni and Reiten, who noted the same at around  $KC = 4$  to  $KC = 5$  [15][19].

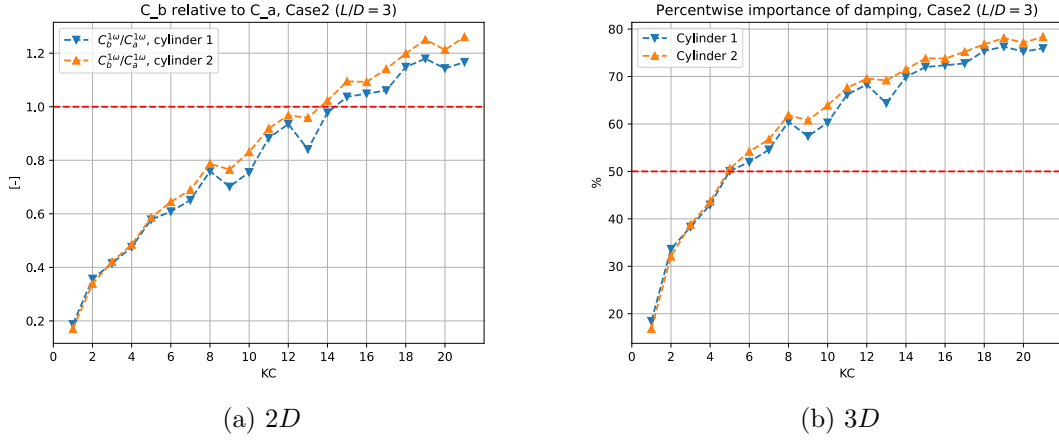


Figure 6.14: Relative importance of the force coefficients for Case 2 ( $\frac{S}{D} = 2$ ) and  $L = 3D$ , and percentwise importance of damping in the force amplitude. Red stapled lines indicate the point where damping overtakes the mass force coefficient.

### 6.1.3 Experiments and Potential theory

This subsection aims to tie the Wadam results together with the experimental mass forces. In doing so, the validity of potential flow theory as an estimation model for the  $1\omega$  added mass force will be evaluated. The added mass is separated from the total force signal using Fourier averaging from Equation 2.14. By multiplying the added mass by the KC equivalent acceleration, the inertial forces are obtained. The inertial forces and the corresponding Wadam results for  $\frac{S}{D} = 1$  are presented in Figure 6.15.

It can be seen that the Wadam results, following the linear curve  $2\pi C_a KC$ , are almost identical to the experimental  $F_I^{1\omega}$  at low KC numbers. This was also the case for the total measured forces in Subsection 6.1.1, but now they remain close for longer in comparison. Viscous forces and vortex shedding become more important at higher KC numbers. Therefore, potential theory will become less valid when the KC number is increased. Notably, the inertial forces and the Wadam results are similar until about  $KC = 8$ , at which point  $F_I^{1\omega}$  starts to creep away from the numerical results. As a result, the experimental added mass forces are  $\approx 30\%$  larger than the Wadam results at  $KC = 21$ .

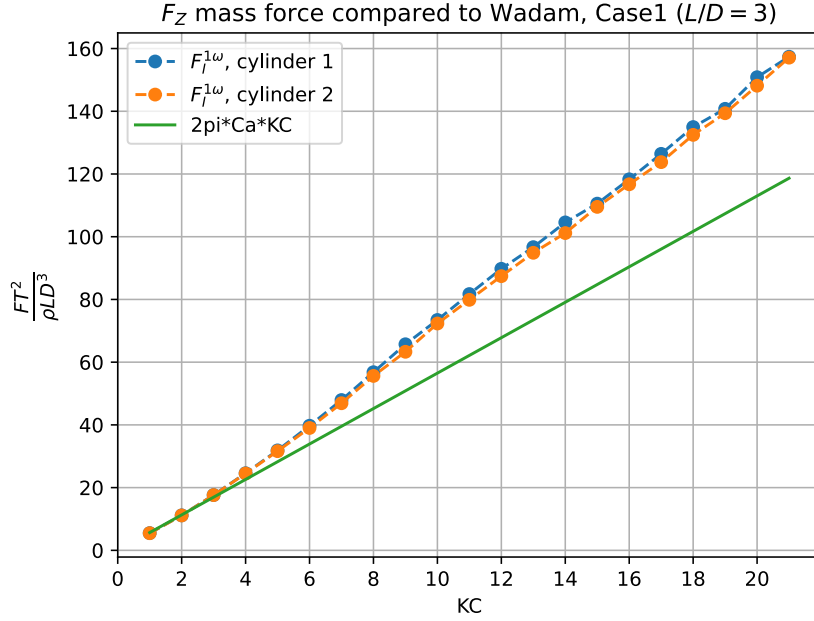


Figure 6.15: The mass force measurements for Case 1 ( $\frac{S}{D} = 1$ ) and  $L = 3D$ , along with results from Wadam. The first  $\omega$  component and the Wadam results coincide well for the first KC numbers.

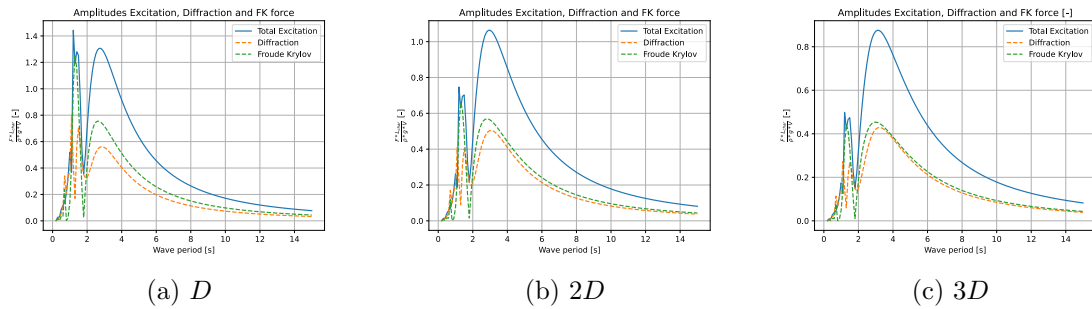


Figure 6.16: Excitation, diffraction and Froude-Kriloff forces for Case 1 ( $\frac{S}{D} = 1$ )

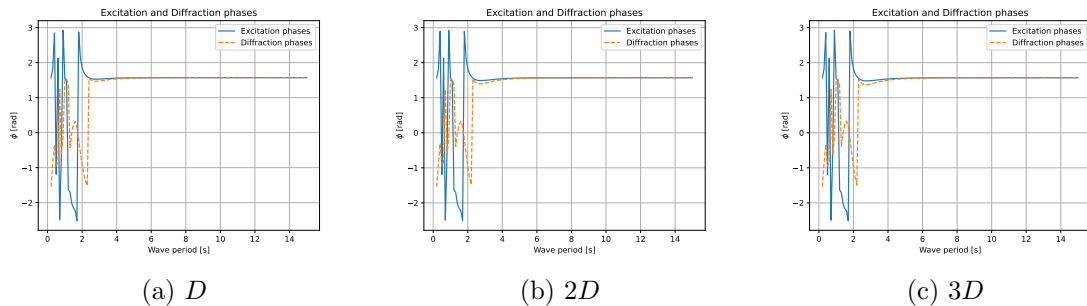


Figure 6.17: Phase angles of the excitation and diffraction forces for Case 1 ( $\frac{S}{D} = 1$ )

The  $\frac{S}{D} = 2$  inertial forces and the corresponding Wadam results are shown in Figure 6.18. Like the results for  $\frac{S}{D} = 1$ , the Wadam results follow the experimental inertial forces much

closer compared to the total forces. It may however, seem like the experimental results increases slightly faster away from the numerical results for  $\frac{S}{D} = 2$ , although not by much. In Subsection 6.1.2 it was discussed how the forces were increased when the spacing ratio was increased. This is also reflected with the added mass force in Figure 6.18 being slightly increased compared to Figure 6.15. Interestingly, the experimental results are now more overestimated compared to the lower spacing ratio. With regards to the percentage, it went from  $\approx 30\%$  to  $\approx 40\%$  overestimation compared to the numerical results.

In addition, the excitation forces are split into the diffraction and Froude-Kriloff forces as described in Section 2.2 and Section 5.5. These forces are presented in Figure 6.16 with the accompanying phases in Figure 6.17 for  $\frac{S}{D} = 1$ . Likewise, the forces and phases for  $\frac{S}{D} = 2$  are presented by Figure 6.19 and Figure 6.20. The general trends stay the same for both  $\frac{S}{D} = 1$  and  $\frac{S}{D} = 2$ , with large phase angle dependency at shorter waves before smoothing out at longer  $T$ . It is also seen that the phases converge to  $\frac{\pi}{2}$  at about  $T = 3s$ , at which point all the forces are in phase for the full-scale model. Normalizing the diffraction forces further by water particle acceleration after  $T = 3s$  will yield  $C_a$  from Wadam [7].

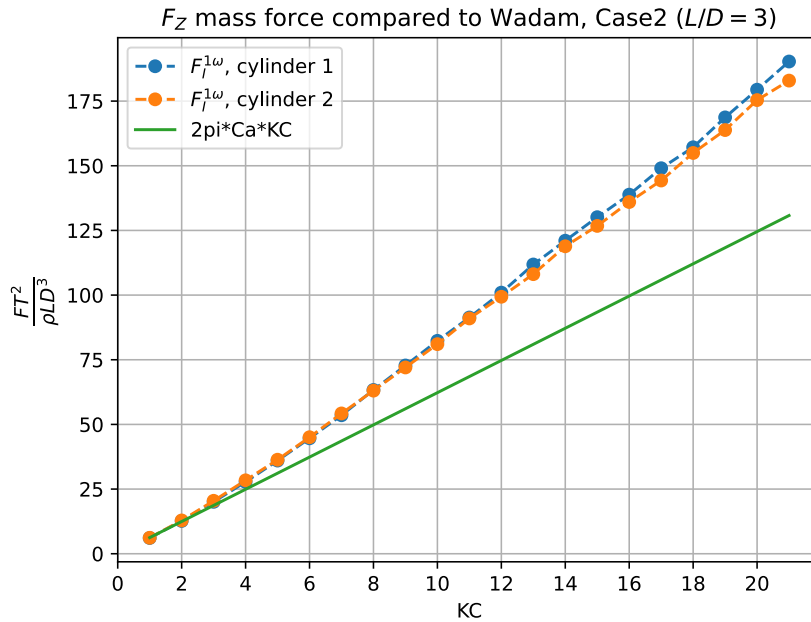


Figure 6.18: The mass force measurements for Case 2 ( $\frac{S}{D} = 2$ ) and  $L = 3D$ , along with results from Wadam. The first  $\omega$  component and the Wadam results coincide well for the first KC numbers.

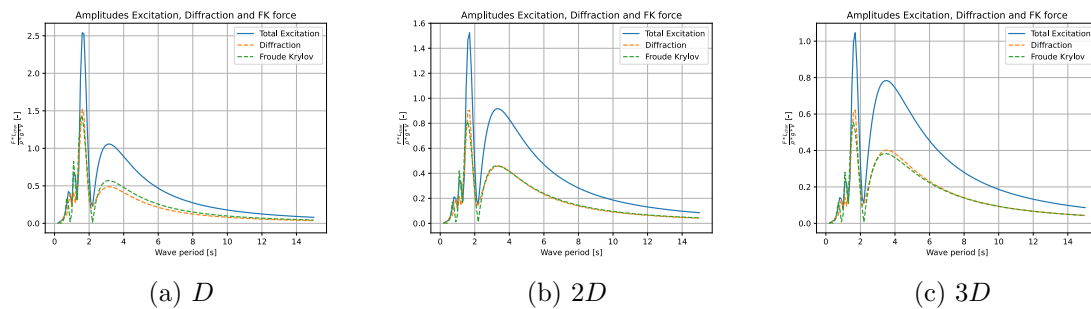


Figure 6.19: Excitation, diffraction and Froude-Kriloff forces for Case 2 ( $\frac{S}{D} = 2$ )

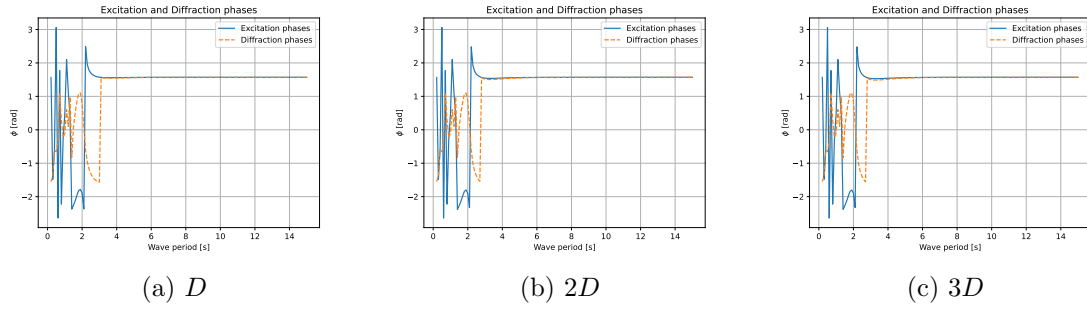


Figure 6.20: Phase angles of the excitation and diffraction forces for Case 2 ( $\frac{S}{D} = 2$ )

It is seen in Figure 6.15 and Figure 6.18 that the difference between experimental added mass force and the numerical added mass increases at high KC numbers. Potential flow theory is not really compatible with vortex shedding by definition. As viscous effects become more prevalent at higher KC numbers, the numerical potential theory results should become less valid. Tying this back to Figure 6.15 and Figure 6.18, means that the results show the added mass forces are increased due to the presence of viscous vortex shedding.

### 6.1.4 Higher Order Force Coefficients

The following subsection presents the results for higher order  $\omega$  forces. Due to the noise discussed in Section 4.4 and Section 3.4, the main focus will be on the  $2\omega$  and  $3\omega$  contributions.

To calculate the added mass and damping, the acceleration and velocity utilized in Equation (2.16) and Equation (2.17) must match the  $\omega$  component of the force being represented. This is already satisfied for the  $1\omega$  forces because the rig acceleration is  $1\omega$ , and the measurements from the accelerometer can be used directly. For the higher-order force components, fictitious  $\ddot{\eta}(t)$  and  $\dot{\eta}(t)$  are created by assuming unit amplitude for the acceleration and integrating to get velocity. This is expressed as

$$\ddot{\eta}(t) = \cos n\omega t, \quad (6.1)$$

$$\dot{\eta}(t) = \frac{1}{n\omega} \sin n\omega t, \quad (6.2)$$

where  $n$  is the frequency order. These expressions are used to create time series of  $5T$ , which can subsequently be used to calculate the force coefficients. This fictitious velocity and acceleration should be in phase with the force. It is important to note that the coefficients created by this process are not correctly scaled, but nonetheless, provide us with a qualitative basis to analyze the general trends in the higher-order forces.

Before presenting the higher-order results and discussing them, the opportunity to talk about the nature of the results is taken. Force coefficients are usually not presented as negative values, and many may therefore find the negative values strange. However, there is a reason for this. The actuator oscillates with a frequency of  $1\omega$ , meaning that all energy injection to the system happens at this frequency as well. This implies that:



1.  $C_b^{1\omega}$  should never be negative for the cases in tandem configuration. And,
2.  $C_a$  can always be negative. Examples of negative  $C_a^{1\omega}$  is VIV or moonpool resonance, although this is not expected here.

No energy injection happens at the higher order frequencies, and we can not expect the same for  $2\omega$  and  $3\omega$  contributions. Furthermore, we expect large interaction between vortices and cylinders in the wake interaction problem. It is reasonable to believe that a significant degree of stochasticity is related to this interaction. As a result, the coefficient signs and the KC number dependency may seem random. Identifying trends in the results will be important to determine the degree of stochasticity, and can provide clues to the governing parameters for each harmonic contribution.

The  $2\omega$  coefficients are presented in Figure 6.21 and Figure 6.22 for  $\frac{S}{D} = 1$  and  $\frac{S}{D} = 2$  respectively.

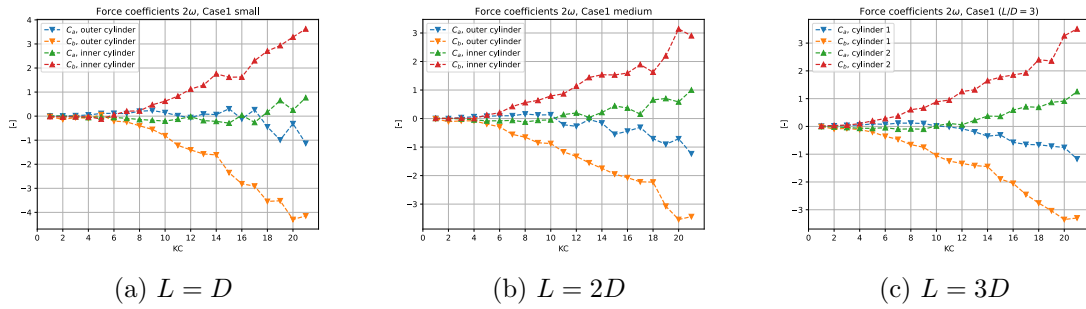


Figure 6.21:  $2\omega$  force coefficients for Case 1 ( $\frac{S}{D} = 1$ ).

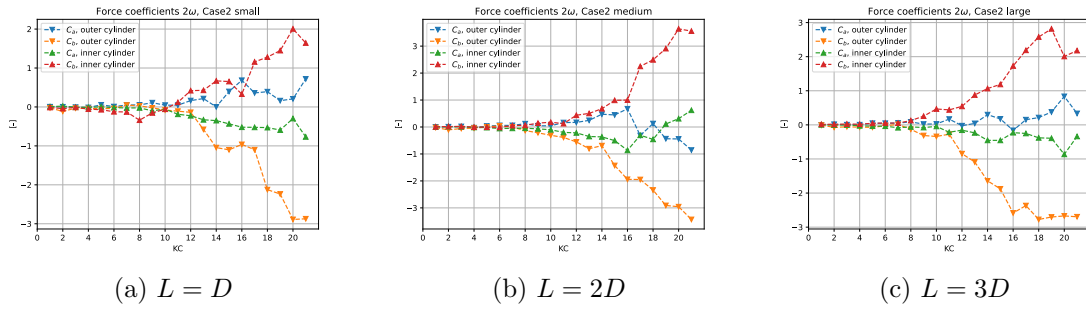


Figure 6.22:  $2\omega$  force coefficients for Case 2 ( $\frac{S}{D} = 2$ ).

There are mainly five prominent takeaways from Figure 6.21 and Figure 6.22 at face value:

1. The general trends for each case are, broadly speaking, independent of the cylinder lengths.
2. With the exception of some scatter on a KC number basis, the general range and magnitudes of the coefficients stay the same for all  $L$  within each case.
3. The inner and outer cylinders' results mostly mirror each other around the KC axis.
4. Damping forces dominate the  $2\omega$  force response for most of the KC number range.

5. The mass force stays relatively unchanged when going from  $\frac{S}{D} = 1$  to  $\frac{S}{D} = 2$ .

The first two points are significant. They offer a hint that the 3D end effects may not be a significant governing factor regarding the general trends of the  $2\omega$  force response. The most likely effect of the 3D end effect is the introduction of scatter in the coefficient values, as shown by the discrepancy between the values in Figure 6.22a and the other figures. We know from the findings of Li [13] that the St number spectrum is broad-banded at the ends of 3D cylinders. If there is a large randomness related to the vortex shedding at the end, it might contribute to the fluctuations seen on a KC number basis. A plausible explanation of the general trend seen in the  $2\omega$  coefficients may be the velocity reduction in the wake. This solution was proposed by Kristiansen, who identified the  $\Delta F_z^{2\omega}$  component and its mean using the drag equation with velocity reduction [12]. If this is the case, a velocity reduction may explain the nonlinear increase in  $C_b^{2\omega}$ .

The third point is also a good indication that the  $2\omega$  trends are largely decided by the velocity reduction. Velocity reduction from the upstream cylinder wake in an oscillating flow indicates that a cylinder's drag should always be bigger in one direction of the oscillation. This fact alone should also indicate the formation of a mean value. Furthermore, this indicates that the maximum  $2\omega$  value of the two cylinders should be 180 degrees out of phase from each other, or have opposite signs.

The last two points show that the damping forces dominate the  $2\omega$  forces for large KC numbers. Both mass and damping coefficients seem insignificant at low KC numbers, before increasing when approaching high KC numbers.  $C_b^{2\omega}$  in particular increases sharply at the first sign of increase, while  $C_a^{2\omega}$  increases slowly and seem independent of the spacing ratio. This may indicate that  $C_a^{2\omega}$  is largely unaffected by the velocity reduction from the wake, or is mainly due to sources of error. Furthermore, the sharp rise in  $C_b^{2\omega}$  seems shifted towards larger KC numbers when the spacing ratio was increased, which further strengthens the velocity reduction as an explanatory model.

The  $3\omega$  coefficients are presented in Figure 6.23 and Figure 6.24 for  $\frac{S}{D} = 1$  and  $\frac{S}{D} = 2$  respectively.

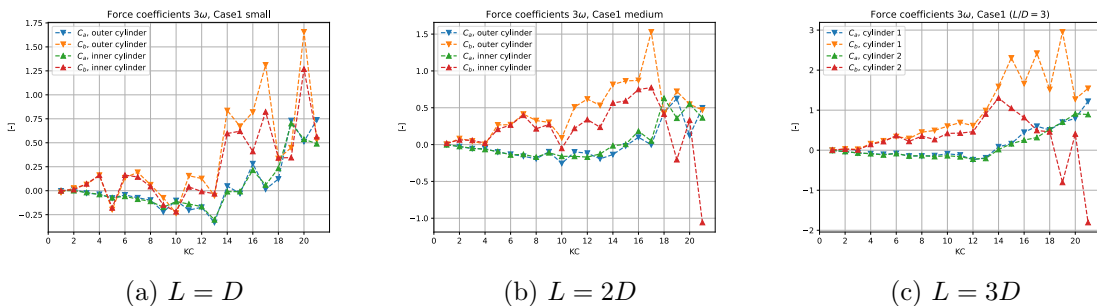
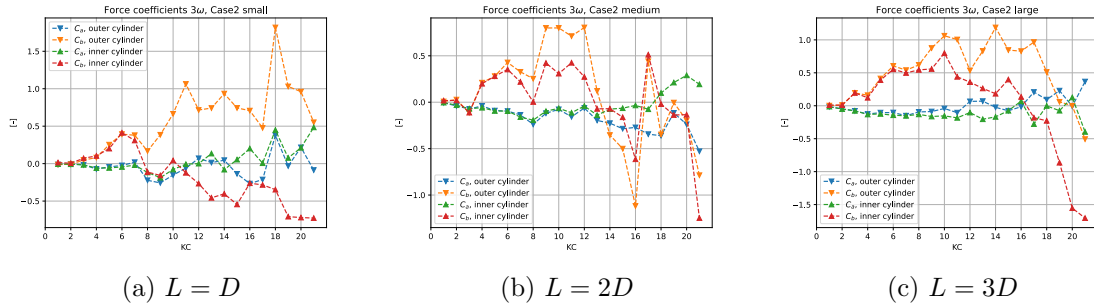


Figure 6.23:  $3\omega$  force coefficients for Case 1 ( $\frac{S}{D} = 1$ ).


 Figure 6.24:  $3\omega$  force coefficients for Case 2 ( $\frac{S}{D} = 2$ ).

Unlike the force coefficients for  $2\omega$ , trends in the  $3\omega$  coefficients are much harder to identify. There seems to be some kind of trend where the  $3\omega$  mass force is slightly negative at lower KC numbers before a slow and steady increase in the positive direction is observed. This is, however, not universal across all the lengths for the two spacing ratios. Figure 6.24a and Figure 6.24b specifically show that the mass coefficients may sporadically change sign on a KC number basis and subsequently stand out from this trend. Scatter on a KC number basis also seems to affect the results.

The damping coefficients exhibit no consistent trend across the board. They may start to increase and stay high and positive, increase and quickly fall towards strongly negative values, decrease slowly and steadily without stopping, or sporadically change between strongly positive and negative values. The two cylinders may exhibit different tendencies at the same time. Therefore, significant scatter and stochasticity clearly characterize the results for  $C_b^{3\omega}$ , and trends are hard to identify.

## 6.2 Staggered Arrangement

Results for staggered arrangement are the product of the experimental investigation as described in Figure 3.8, conducted during the spring. Any convention established regarding the formatting of the post-processed results from tandem configuration is kept. To that end, Cylinder 1 and Cylinder 2 are still placed at the bottom and top of the tank respectively. The results are presented as the harmonic components of the drag and lift forces on each cylinder, denoted  $D$  and  $L$ . Unlike the tandem configuration, the staggered configuration is designed to investigate the effects of the inflow angle  $\theta$ . Note that  $z$  and  $y$ -direction for tandem coincides with drag and lift respectively when  $\theta = 90^\circ$ . Due to limitations on the experimental rig,  $\theta$  could only be tested between  $\theta = 90^\circ$  and  $\theta = 35^\circ$  with increments of  $5^\circ$ .

### 6.2.1 $1\omega$ Force Components

The  $1\omega$  force components will be presented first for the staggered arrangement, as they show the most consistency over the different cylinder lengths. These results for  $F_D^{1\omega}$  and  $F_L^{1\omega}$  are presented for all  $L$  in Figure 6.25.

It was noted earlier that the dimensionless results in tandem configuration stay largely independent of  $L$ . Interestingly, this does not seem to hold true for the staggered arrangement. The results for drag and lift are seen to increase for each incremental increase in  $L$ .

Although  $F_D^{1\omega}$  and  $F_L^{1\omega}$  increase when increasing  $L$ , the general trend stays consistent in both Figure 6.25a, Figure 6.25b and Figure 6.25c. Localized, the water will flow in the direction of least resistance. For 3D cylinders with end effects, this means that the flow may choose to flow below the ends instead of around the "wall" formed by the cylinders. If the water for some reason is more likely to choose to flow under the cylinders for staggered cylinders compared to tandem, this might explain the sudden  $L$  dependency. This is, however, not certain at this stage of the research. Further investigations are required to determine this relationship definitely.

Firstly, both  $F_D^{1\omega}$  and  $F_L^{1\omega}$  experience a sudden increase at the first increments of  $\theta$ . For drag, this trend continues up until  $\theta = 65^\circ$  before stagnating. A kind of plateau is then formed between  $65^\circ$  and  $45^\circ$  before  $F_D^{1\omega}$  starts to decrease. A maximum drag is observed at  $\theta = 55^\circ$  for all  $L$ . Note that  $\theta = 45^\circ$  were unable to be tested for  $L = 2D$  due to limitations with the experimental rig, leading to a sharper plateau in Figure 6.25b.

The lift forces experience a much sharper increase at the first  $\theta$  increments compared to  $F_D^{1\omega}$ . This is sensible as  $F_L^{1\omega}$  is almost negligible at  $\theta = 90^\circ$ . They continue to grow up to about  $\theta = 65^\circ$  before a sharp free fall is experienced. It appears that the minimum lift is consistent throughout all  $L$  at about  $45^\circ$ . In contrast, the maximum lift is located between  $75^\circ$  and  $65^\circ$  depending on  $\frac{L}{D}$ . The drag and lift forces subsequently experience their maxima and minima at different inflow angles.

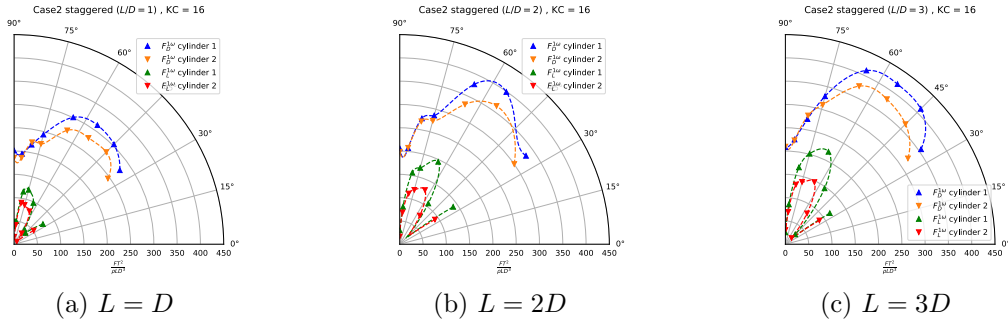


Figure 6.25:  $F_D^{1\omega}$  and  $F_L^{1\omega}$  at  $KC = 16$  for staggered arrangements.

As for tandem arrangement,  $\Delta F_D$  and  $\Delta F_L$  are also evaluated and presented in Figure 6.26. Where trends were found for  $F_D^{1\omega}$  and  $F_L^{1\omega}$ , there certainly are none for  $\Delta F_D^{1\omega}$  and  $\Delta F_L^{1\omega}$ . The only shared finding in Figure 6.26 is that maximum  $\Delta F_L^{1\omega}$  is located at  $\theta = 65^\circ$  for both  $L = 2D$  and  $L = 3D$ . It is otherwise difficult to locate any consistency between the three lengths.  $L = D$  for instance is completely different quantitatively and qualitatively from the other lengths.

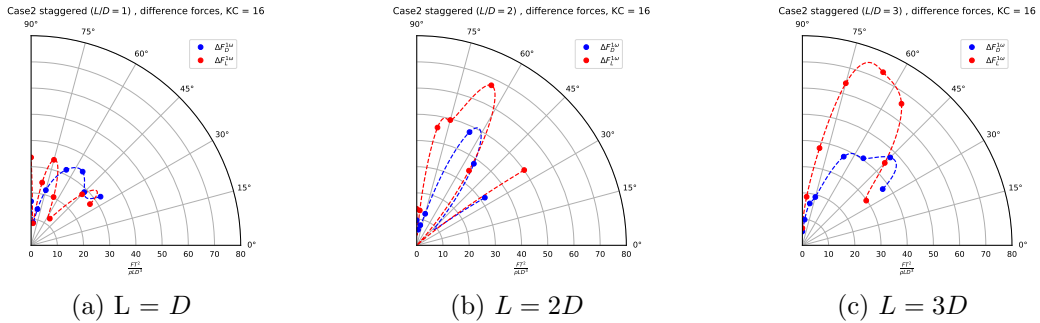


Figure 6.26:  $\Delta F_D^{1\omega}$  and  $\Delta F_L^{1\omega}$  at  $KC = 16$  for staggered arrangements.

To summarize, the  $1\omega$  drag and lift forces do appear to show general trends across the board for all  $L$ . What makes  $F_D^{1\omega}$  and  $F_L^{1\omega}$  from the staggered arrangement fundamentally different from their tandem counterpart is that their nondimensional magnitude seems dependent on  $L$ . This is also observed in Figure 6.25 and Figure 6.26, where the magnitude of the forces seem independent of  $L$  at  $\theta = 90^\circ$ . Any trend in the difference forces is cumbersome to identify, but it seems that  $\Delta F_L^{1\omega}$  has a large increase around  $75^\circ$  and  $65^\circ$ . The magnitudes and general shapes are not consistent across all  $L$ .

### 6.2.2 Higher Order Force Components

It was noted in Section 6.1.4 that scatter becomes more prevalent for higher  $\omega$  contributions. Given the previous analysis of the  $1\omega$  contribution for staggered arrangement, a significant scatter is expected for the higher-order frequencies. Figure 6.27 presents the results for  $F_D^{2\omega}$  and  $F_L^{2\omega}$ , while Figure 6.28 shows the results for  $\Delta F_D^{2\omega}$  and  $\Delta F_L^{2\omega}$ .

As expected, the forces from Figure 6.27 present quite different trends qualitatively across the  $L$  range. Curves do not stay consistent, and peaks or maxima are even shifted to different  $\theta$ . It is therefore difficult to make an identification of any trends that may characterize the  $2\omega$  forces. The cluster of measurement points does seem to become more stretched out or increased in magnitude by the increase in  $L$ . This is consistent with the  $1\omega$  drag and lift, which was also seen to be dependent on  $L$ .

The  $\Delta F_D^{2\omega}$  and  $\Delta F_L^{2\omega}$  amplitudes reflect the tendencies in ordinary lift and drag forces. Any significant peak seems to be at a random  $\theta$  and with a large scatter in magnitude. The notable difference is  $\Delta F_D^{2\omega}$  for  $L = 2D$  and  $L = 3D$ , where maximum drag is estimated at the same  $\theta$  with similar magnitudes. This is however not reflected for  $L = D$ . Figure 6.27c is also quite different from the findings of Reiten, both qualitatively and quantitatively [19]. The scatter on both measured drag and lift, as well as the difference forces, persists also on a  $KC$  number basis.

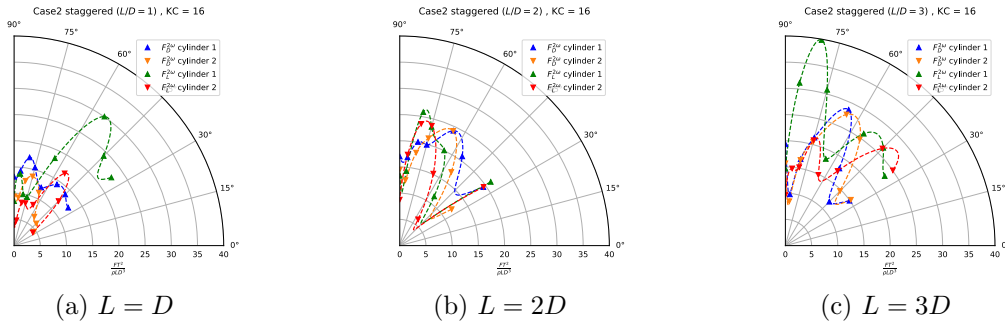


Figure 6.27:  $F_D^{2\omega}$  and  $F_L^{2\omega}$  at  $KC = 16$  for staggered arrangements.

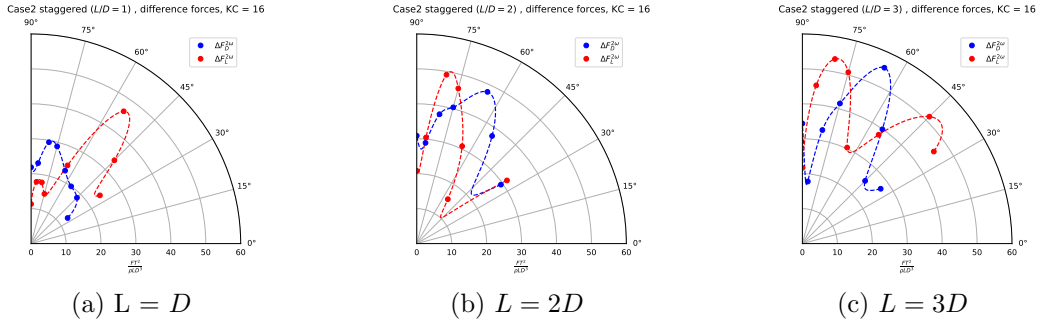


Figure 6.28:  $\Delta F_D^{2\omega}$  and  $\Delta F_L^{2\omega}$  at  $KC = 16$  for staggered arrangements.

The  $3\omega$  contributions from Figure 6.29 seem even more prone to scatter. It does appear that the maximum peak of  $F_L^{3\omega}$  is localized at earlier  $\theta$  increments, but the general shape varies. Unlike for  $1\omega$  and  $2\omega$  force contributions, the overall  $3\omega$  magnitude cluster does not seem largely affected by the change in  $L$ , although this is hard to determine definitely.

$\Delta F_D^{3\omega}$  and  $\Delta F_L^{3\omega}$  are presented in Figure 6.30. The drag forces seem to be behaving similarly throughout all cylinder lengths. On the other hand, the lift forces seem much more spurious both in trend and magnitude.

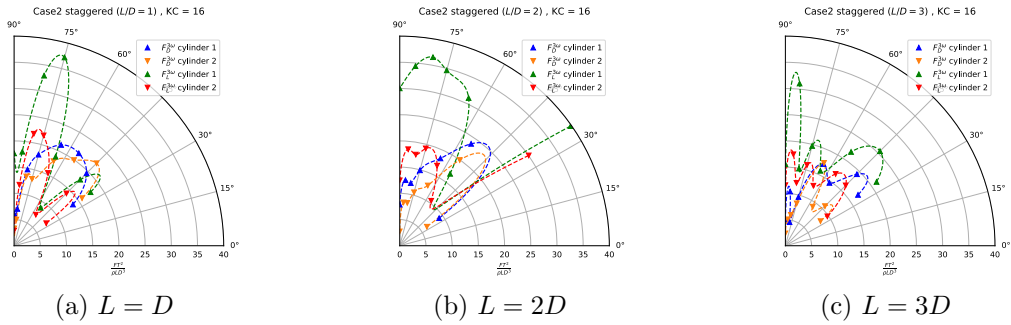


Figure 6.29:  $F_D^{3\omega}$  and  $F_L^{3\omega}$  at  $KC = 16$  for staggered arrangements.

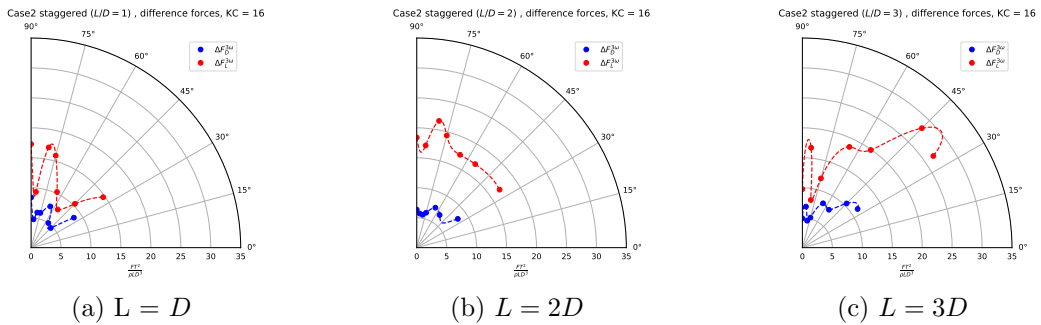


Figure 6.30:  $\Delta F_D^{3\omega}$  and  $\Delta F_L^{3\omega}$  at  $KC = 16$  for staggered arrangements.

To summarize, the higher-order frequency components are characterized by a large degree of scatter. This scatter is seen in both changes in  $L$  and the  $KC$  number. It is possible that this scatter is related to the broad-banded vortex-shedding Li found at the base ends. As he considered much longer cylinders, the larger order frequencies in our results may be exacerbated in comparison. This is however hard to determine definitely. Due to this stochasticity, repetition testing will be important in order to provide a comprehensive

picture of these forces. The scatter is also reflected in the difference forces, and their overall usefulness should be evaluated at this stage until a more holistic understanding of the regular forces is acquired.

### 6.2.3 Damping Forces - Staggered Arrangement

The most important source of prior research on the staggered arrangement is the paper by Zdravkovich. As mentioned in Section 1.4, Zdravkovich created contour plots of the drag and lift coefficients as a function of longitudinal and transverse spacing ratios. As Zdravkovich only considered steady flow, it is necessary to isolate the damping results from the experiments in order to compare the two. Compliance between the damping results and the findings of Zdravkovich would be a good validation of the results.

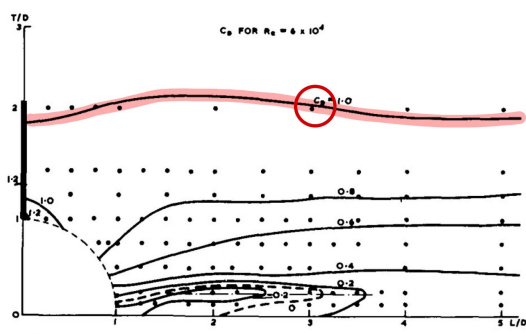


Fig. 23 Drag force coefficient for a downstream cylinder at  $Re = 6.1 \times 10^4$  [17]

(a) Drag coefficients

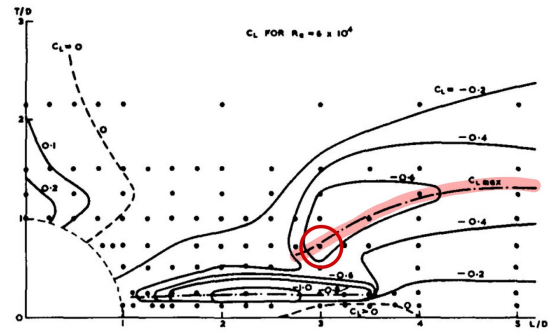


Fig. 22 Lift force coefficient for a downstream cylinder at  $Re = 6.1 \times 10^4$  [17]

(b) Lift coefficients

Figure 6.31: Contour plots from Zdravkovich for  $C_D$  and  $C_L$  from Figure 1.4, with the expected largest values marked for Case 2 ( $\frac{S}{D} = 2$ ).

Source: [26]

By using the spacing ratio for Case 2 along with the information from Figure 6.31, it is possible to estimate the angles where the largest  $C_L$  and  $C_D$  are expected to occur. One can use

$$\theta = 90^\circ - \arctan\left(\frac{(T/D)}{(L/D)}\right), \quad (6.3)$$

where  $T/D$  and  $L/D$  are the longitudinal and transverse spacing ratios respectively. The center-to-center distance between the cylinders in Case 2 can be written as  $S/D = 3$ . Finding the crossing between the contours of maximum drag and lift coefficients with  $S/D$  for Case 2 and using these values in Equation (6.3) will give approximately

$$\theta_D \approx 90^\circ - \arctan\left(\frac{2}{3}\right) = 56^\circ, \quad (6.4)$$

and

$$\theta_L \approx 90^\circ - \arctan\left(\frac{0.75}{3}\right) = 75^\circ \quad (6.5)$$

for drag and lift respectively. These calculations indicate that it is expected that drag should reach its maximal value at about  $\theta = 56^\circ$ . Likewise, lift should reach its maximum value at about  $\theta = 75^\circ$ . Remember that Zdravkovich defined his lift coefficients in Figure 1.4b as negative values, and one should expect a negative maximal value at this angle for the experiments.

Case2 staggered ( $L/D = 3$ ), damping forces,  $KC = 16$

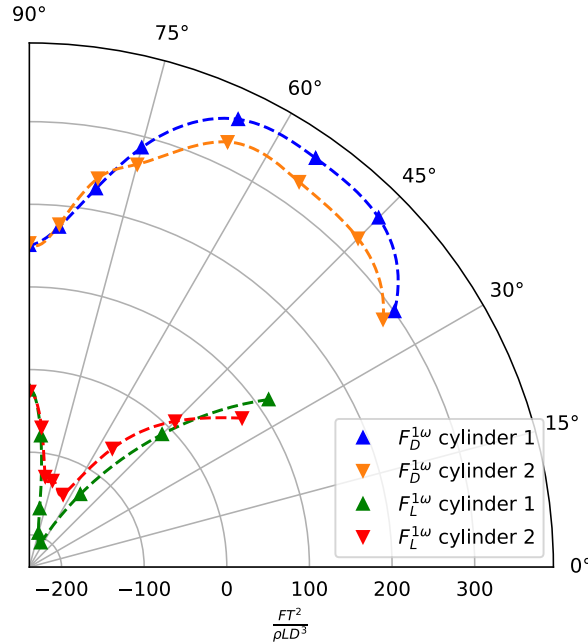


Figure 6.32:  $1\omega$  damping forces at  $KC = 16$  with  $L = 3D$ . The results show good correspondence with the findings of Zdravkovich, with a maximum at  $\theta = 75^\circ$  and  $\theta = 55^\circ$  for drag and lift respectively [26].

The damping forces for the staggered flow at  $KC = 16$  for large cylinders are illustrated in Figure 6.32. There are at least three main takeaways from this figure; Maximum drag coincides with an inflow angle of about  $\theta = 55^\circ$ , the minimum lift is located at about  $\theta = 75^\circ$  and drag decreases after an inflow angle  $\theta = 45^\circ$ . These takeaways seem independent of both cylinder lengths and  $KC$  number, as shown in the appendices by Figure C.1 and Figure C.2.

The possible explanations for each of these takeaways are presented separately.

1. Drag is seen to increase with a decrease in  $\theta$ . A likely explanation is that the downstream cylinder is gradually shifted outside the turbulent wake from the upstream cylinder. This means that the downstream cylinder experiences less velocity reduction from the turbulent wake.
2. The maximum negative lift is located at  $\theta = 75^\circ$ . As noted by Zdravkovich, a plausible explanation for the negative lift value may already be provided by Mair and Maull. They proposed that the negative lift is due to the entrainment of flow into the wake boundary of the upstream cylinder [14]. Furthermore, Zdravkovich noted that maximum negative lift is reached when the downstream cylinder displaces the wake and compresses the streamlines between its inner side and the displaced wake [26].



3. The drag starts to decrease after  $\theta = 45^\circ$ . This may be explained by the frontal area of the cylinders in the viscous part of Equation (2.28) decreasing. Additionally, the cylinders experience a gradual change away from diamond back to square geometry as they are rotated beyond  $\theta = 45^\circ$ , which are known to produce larger forces.

The findings regarding the second point are particularly interesting. As shown in Figure 6.32, the lift forces exhibit a quick increase in the negative lift as the first  $\theta$  increments towards its maximum value at  $\theta = 75^\circ$  before experiencing an abrupt fall in magnitude. This creates a sharp spike in the damping lift forces, and the same abrupt fall was also noted by Zdravkovich. Considering the inflow angle and the cylinder positions, it is likely that an intense gap flow between the cylinders is responsible for the large lift force. If this is correct, then the abrupt decrease in negative lift going from  $\theta = 75^\circ$  to  $\theta = 90^\circ$  is explained by a blockage of that gap flow. Subsequently, the abrupt fall going from maximum negative lift towards lower  $\theta$  is due to more projected space in the gap, lowering the intensity of the gap flow.

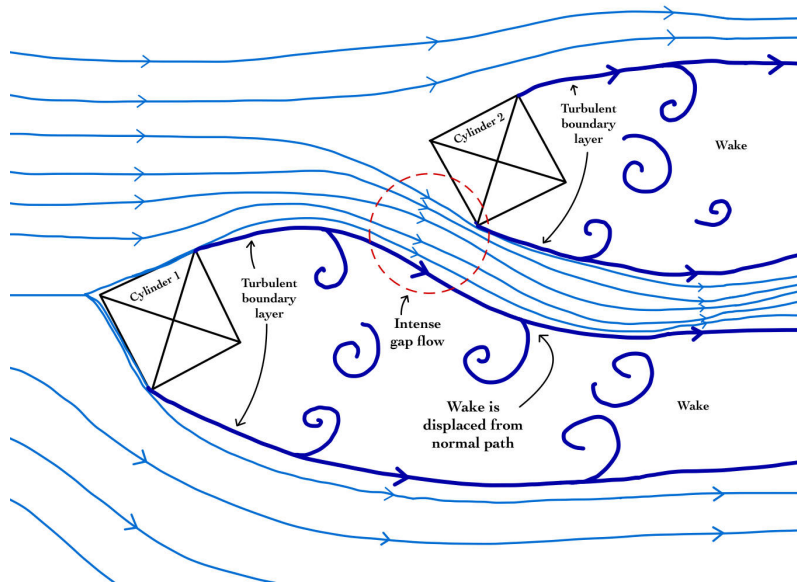


Figure 6.33: A sketch of the flow pattern for staggered arrangement.

### 6.3 A Discussion on $2\omega$ Forces

As mentioned earlier in Section 6.1.4, a plausible explanation for the  $2\omega$  response of the force in tandem is the wake velocity reduction. This section will outline how the findings in that section affect the difference forces and why the  $2\omega$  component dominates. The Morison equation in Section 2.7 is used to describe this phenomenon. By assuming large KC numbers, Equation (2.28) can be reduced to the drag term since we expect viscous drag to dominate at large KC numbers. The Morison equation then becomes

$$F_D = \frac{1}{2} \rho D C_D u |u|. \quad (6.6)$$

As described by Kristiansen, a simplified wake model by introducing a wake reduction factor on the velocity acting on the cylinders for separate half-cycles [12] can be created. This is expressed as

$$u = u_a \sin \omega t, \quad 0 \leq t \leq \frac{T}{2} \quad (6.7)$$

$$u = u_b \sin \omega t, \quad \frac{T}{2} \leq t \leq T \quad (6.8)$$

where  $u_a$  is the undisturbed velocity amplitude and  $u_b$  is the reduced velocity amplitude. Introducing this half-cycle velocity reduction to Equation (6.6) results in the force expressions

$$F_D = \frac{1}{2} \rho D C_D u_a^2 \sin \omega t |\sin \omega t|, \quad 0 \leq t \leq \frac{T}{2} \quad (6.9)$$

$$F_D = \frac{1}{2} \rho D C_D u_b^2 \sin \omega t |\sin \omega t|, \quad \frac{T}{2} \leq t \leq T \quad (6.10)$$

A time series of the drag force on two cylinders generated in this manner is presented in Figure 6.34. The forces are generated by expressing the velocities by  $u_b = 0.8 \cdot u_a$ , using 0.8 as the wake reduction factor.

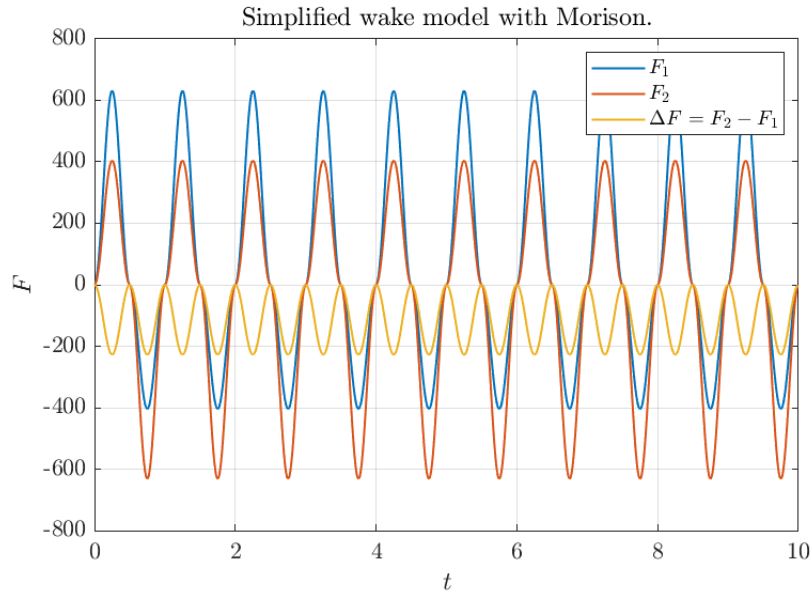


Figure 6.34: Time series of a simplified wake model with the Morison equation. The wake model applies a constant velocity reduction factor of 0.8 on each cylinder during a half period.

Source: [12]

Figure 6.34 shows mainly two takeaway points. Firstly, the wake reduction model proposed by Kristiansen correctly identifies that the  $2\omega$  component dominates  $\Delta F_z$ . Secondly, this model correctly identifies the nonzero mean of this  $\Delta F_z$ . Both of these takeaway points are observed in the experimental investigation, and along with the findings and discussion in Section 6.1.4, seem to strengthen velocity reduction as an explanatory model.

An attempt is made to further elaborate on the explosive nonlinear increase of the  $2\omega$  components shown in Figure 6.5 and Figure 6.12.

Remember, one of the main takeaways from Section 6.1.4 was that the cylinders'  $2\omega$  forces mostly mirror each other around the KC axis in Figure 6.21 and Figure 6.22. As a reference point for further discussion, Figure 6.21c is presented on its own as an example in Figure 6.35.

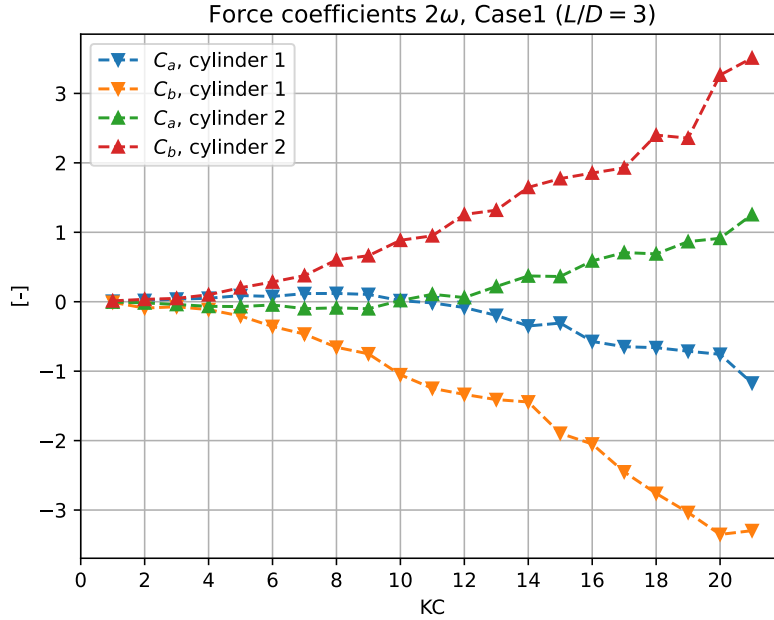


Figure 6.35:  $2\omega$  force coefficients for Case 1 ( $\frac{S}{D} = 1$ ) and  $L = 3D$ .

For simplicity, we assume that the forces on the two cylinders are exactly mirrored. In other words, the absolute value of the  $2\omega$  forces on the two cylinders are assumed to be exactly equal, and the forces act in opposite directions. This can be expressed as

$$F_1^{2\omega} = -F_2^{2\omega}. \quad (6.11)$$

The difference forces are obtained by subtracting the forces of one cylinder from the other. By using Equation (6.11) to calculate the difference forces, one obtains

$$\Delta F^{2\omega} = F_1^{2\omega} - (-F_1^{2\omega}) \quad (6.12)$$

$$\Delta F^{2\omega} = 2F_1^{2\omega}. \quad (6.13)$$

This estimation from Equation (6.13) may seem unremarkable at face value. However, it is evident from Figure 6.35 that  $F_1$  and  $F_2$  individually increase non-linearly as a function of the KC number. This non-linearity is then exacerbated in  $\Delta F$  when the two are summed together, instead of subtracted due to opposite signs. The result is an explosion in the difference force as shown in Figure 6.21 and Figure 6.22.

## 6.4 Qualitative Comparison to 2D CFD

In this section, we aim to bridge the gap between the experimental results presented earlier, and the CFD simulations from Hals. Hals is another MSc prospect who simulated the experimental cases using a 2D RANS model. The primary objective is to assess the agreement and discrepancies between the experimental data and the numerical findings from Hals's 2D RANS simulations. By evaluating and comparing the experimental results and CFD simulations, we aim to provide valuable insight and guidance toward improvements in simulation techniques for future investigations. Subsequently, this section is written in collaboration with Hals in order to combine the results for comparison [8].

The current and previous paradigm for MSc prospects doing CFD on this topic is to use 2D RANS in OpenFOAM with a  $k-\epsilon$  turbulence model. Reiten obtained good correspondence between his CFD simulations and experiments but only considered 2D investigations for both [19]. Its applicability is not yet evaluated for 3D. The experimental and numerical forces acting on Cylinder 1 in the tandem configuration are presented in Figure 6.36 for both  $\frac{S}{D} = 1$  and  $\frac{S}{D} = 2$ .

It quickly becomes apparent that the 2D numerical simulations overestimate the forces on the cylinder compared to the experiments. The numerical results are expected to be conservative, and the  $1\omega$  forces are reasonably approximated compared to the experimental results for higher KC numbers. At smaller KC numbers the numerical and experimental simulations are almost identical. On the flip side,  $F_z^{2\omega}$  seems vastly overestimated compared to the experiments. The point where the numerical and experimental  $F_z^{2\omega}$  diverges seems shifted to higher KC numbers for  $\frac{S}{D} = 2$ , and these points indicate that the RANS model is unable to accurately resolve the wake interaction.

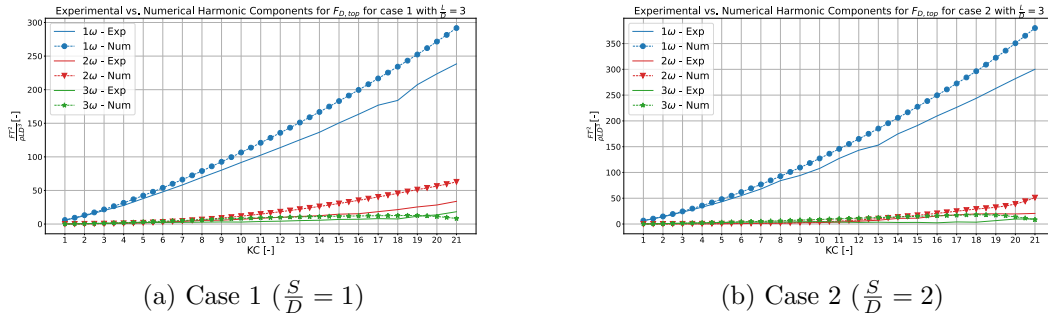


Figure 6.36: Comparison of  $F_z$  between the tandem 3D experiments and 2D CFD simulations.

The  $\Delta F_z^{2\omega}$  forces should reflect the discrepancies in  $F_z^{2\omega}$ , and make them easier to locate. A similar alignment for the difference forces is provided in Figure 6.37. As discussed in Section 6.3, the  $2\omega$  difference force is expected to be approximately  $2F_z^{2\omega}$ . The difference forces can therefore be considered representative of  $2\omega$  differences in numerical and experimental results. From Figure 6.37 it is shown that  $\Delta F_z^{2\omega}$  is about double the experimental results. As mentioned earlier, numerical  $\Delta F_z^{2\omega}$  overestimates the experiments at later KC numbers when spacing is increased.

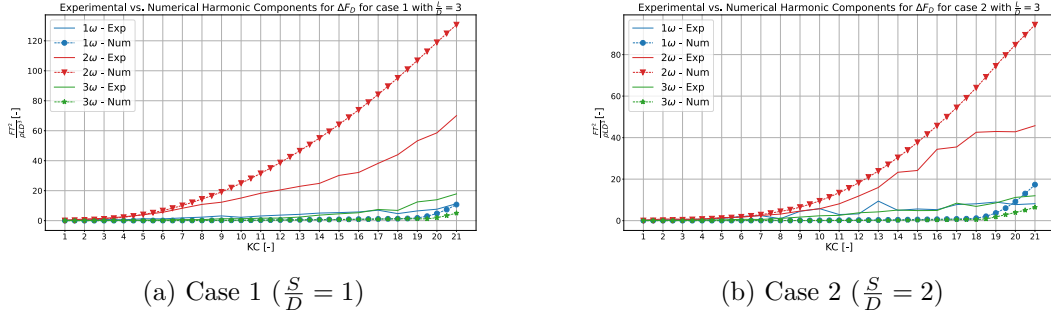


Figure 6.37: Comparison of  $\Delta F_z$  between the tandem 3D experiments and 2D CFD simulations.

It should be noted that the numerical simulations manage to capture the general trends observed for the 3D experiments. Furthermore, it accurately resolves the forces at the lowest KC numbers, although starts to overpredict the forces when increasing the KC number further. This may be explained by the use of the RANS model, which in general does not resolve the wake and vortex shedding properly. Therefore, it is not surprising that the  $2\omega$  forces are not accurately predicted. Furthermore, the use of the  $k - \epsilon$  turbulence model may pose challenges. This is a model that is tuned to near-parallel flow and is consequently not very suitable for bluff body flow. It should therefore be considered an engineering model and not a scientific model when used in the context of this scope of work.

Results for staggered arrangements are also compared. As outlined in Section 6.2, the experimental staggered arrangement results are subject to significant scatter for higher frequency contributions and  $L$  dependencies for  $1\omega$ . A selection of  $F_D^{1\omega}$ ,  $F_L^{1\omega}$ ,  $\Delta F_D^{2\omega}$  and  $\Delta F_L^{2\omega}$  were chosen to compare the two, whereas the first of these are presented in Figure 6.38.

The overall impression from Figure 6.38 is that the numerical simulations manage to capture the  $\theta$  effects fairly well. This is especially true for the lift forces, which surprisingly are almost identical for the two, although this is likely coincidental. They also manage to capture the general trends fairly well. The numerical results still overestimate the drag forces for most of the range and fail to identify its critical inflow angle.

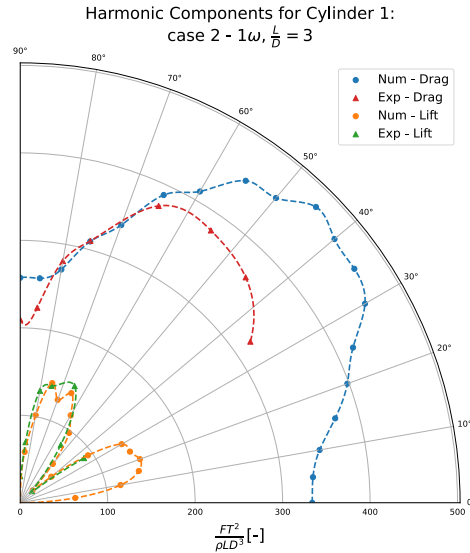


Figure 6.38: Comparison of  $F_D^{1\omega}$  and  $F_L^{1\omega}$  between the staggered 3D experiments and 2D CFD simulations.

The  $2\omega$  contribution has previously been identified as dominating for the difference forces in tandem arrangement. Figure 6.39 shows the comparison of  $\Delta F_D^{2\omega}$  and  $\Delta F_L^{2\omega}$  between the numerical and experiments for staggered arrangement.

It is clear from Figure 6.39a that the numerical results dramatically overestimate the  $\Delta F_L^{2\omega}$  forces. There is no indication from the experiments that this is reasonable. In order to make the drag comparison clear, the lift is neglected in Figure 6.39b. Interestingly the  $\Delta F_D^{2\omega}$  forces from the numerical and experimental results are qualitatively opposite from each other. The maximum drag from the experiments coincides with the minimum value from the RANS model. It is at the moment, unclear whether or not this is due to the large degree of stochasticity and  $L$  dependency in the experimental staggered configuration, or due to mesh and model choices in the numerical modeling. More investigations into this phenomenon are needed to determine this definitely. Overall, the CFD presently seems unfit to properly estimate higher-order force contribution for the staggered arrangement but works reasonably well for  $F_D^{1\omega}$  and  $F_L^{1\omega}$ .



(a) Difference force components

(b) Harmonic force components

Figure 6.39: Comparison of  $\Delta F_D^{1\omega}$  and  $\Delta F_L^{1\omega}$  between the staggered 3D experiments and 2D CFD simulations.

To summarize, the current CFD strategies overestimate the forces and should therefore be treated as conservative estimates. They are capable of providing a reasonable image

of the general trends observed in tandem arrangement and for  $F_D^{1\omega}$  and  $F_L^{1\omega}$  in staggered arrangement. However, higher-order contributions are not accurately predicted by the numerical results, giving large  $2\omega$  forces for tandem and being almost unrecognizable in staggered. As the  $2\omega$  forces and difference forces are a large motivation behind this work, an improved strategy is recommended.

Firstly, the use of the  $k - \epsilon$  turbulence model should probably be reevaluated as it is tuned for near-parallel flow. It is possible to tune the parameters in this model manually in OpenFOAM, but doing so would require a separate study. Alternatively, the  $k - \omega$  (SST) turbulence model can be considered as a substitute for the  $k - \epsilon$  model in future work.

Secondly, a change in the CFD model may be beneficial with regard to resolving the wake. RANS does not resolve the wake accurately and is found to overestimate the  $2\omega$  forces. Switching to a LES model will allow the resolution of large-scale turbulent structures and may improve the overestimation of these forces. This model does however not work well with 2D, warranting 3D CFD instead. Subsequently, this strategy can be computationally expensive and may require a fine mesh resolution. A 3D simulation would be of interest as it can help with the understanding of the 3D end effects of the cylinders. Alternatively, a DES model can be considered. Ultimately, the trade-offs between the different models will need to be evaluated if a model change is relevant.

## 6.5 Comparison to the Morison Equation

The end goal of the investigations is to compare the findings with and evaluate the applicability of the Morison equation. All previous results are presented on a KC number basis, and so the easiest way to compare the experimental results with ordinary Morison equation is to make Equation (2.28) KC number dependent in a similar manner as in Section 5.6. We start with the viscous term in Equation (2.28)

$$F_D = \frac{1}{2}\rho C_D D L u(t) |u(t)|. \quad (6.14)$$

Furthermore, we know from Equation 2.11 that the velocity can be written as  $u = \omega \eta_a \sin(\omega t)$  and that the frequency is equal to  $\omega = \frac{2\pi}{T}$ . The oscillation amplitude  $\eta_a$  can also be expressed by rewriting Equation 2.26 as  $\eta_a = \frac{KC D}{2\pi}$ . We can then rewrite Equation 6.14 as

$$F_D = \frac{1}{2}\rho C_D D L \frac{(2\pi)^2}{T^2} \frac{KC^2 D^2}{(2\pi)^2} \sin(\omega t) |\sin(\omega t)|, \quad (6.15)$$

which can be rewritten to

$$F_D = \frac{1}{2}\rho C_D D^3 L \frac{KC^2}{T^2} \sin(\omega t) |\sin(\omega t)|. \quad (6.16)$$

Using this expression along with the nondimensionalization from Section 4.6, we get the viscous term

$$\frac{F_D T^2}{\rho L D^3} = \frac{1}{2} C_D KC^2 \sin(\omega t) |\sin(\omega t)|. \quad (6.17)$$

This new, nondimensional and KC number-dependent viscous term can be combined with the corresponding inertial term amplitude found in Section 5.6. The result is a nondimensional and KC number-dependent Morison equation. By also accounting for an arbitrary cylinder position  $x$ , this will result in

$$\frac{FT^2}{\rho LD^3} = \frac{1}{2}\pi^2 C_M KC \cos(\omega t - kx) + \frac{1}{2}C_D KC^2 \sin(\omega t - kx)|\sin(\omega t - kx)|, \quad (6.18)$$

where  $k$  is the wave number. Equation (6.18) can be used to generate time series in order to compare between using typical  $C_M$  and  $C_D$  values, and those extracted from the experiments. Furthermore, the velocity reduction principle from Section 6.3 should be implemented. This is done by directly applying the reduction factor to the velocity in the KC number from Equation 2.25. The inertial term can then be written as

$$\frac{F_I T^2}{\rho LD^3} = \frac{1}{2}\pi^2 C_m (f_v KC) \cos(\omega t - kx), \quad (6.19)$$

while the viscous term can be written as

$$\frac{F_D T^2}{\rho LD^3} = \frac{1}{2}C_d (f_v KC)^2 \sin(\omega t - kx)|\sin(\omega t - kx)|, \quad (6.20)$$

where  $f_v$  is a mean velocity factor. Instead of using a constant velocity reduction in accordance with Kristiansen as presented in Section 6.3, a varying  $f_v$  is applied. This  $f_v$  needs to vary in phase with the velocity, and act on the relevant half cycle, depending on the cylinder. Keeping the convention in Section 6.3 with variable reduction, the implementation of  $f_v$  can be expressed as

$$f_v = 1 - (1 - f_r) \sin \omega t, \quad 0 \leq t \leq \frac{T}{2} \quad (6.21)$$

$$f_v = 1, \quad \frac{T}{2} \leq t \leq T \quad (6.22)$$

where  $f_r$  is the reduction factor of the mean velocity. Setting  $f_r = 0.8$  reduces the velocity by 20% at the velocity peak. The implementation of this  $f_r$  is shown in Figure C.5. A visual example of a time series generated using Equation (6.18) is provided in Figure 6.40 for  $KC = 20$  with  $T = 10$ s. Note that  $f_r = 1$  because only one cylinder is presented, and that  $T$  is only used to decide the wave number and time range of the time series.



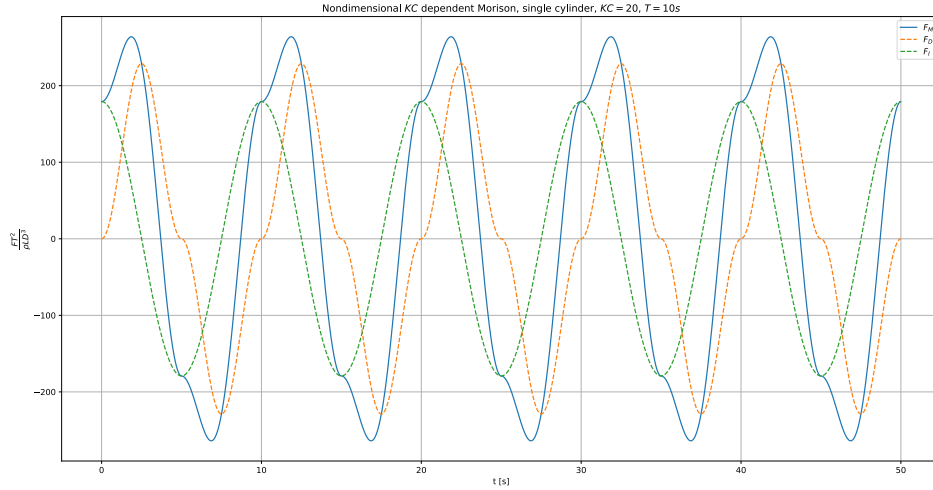
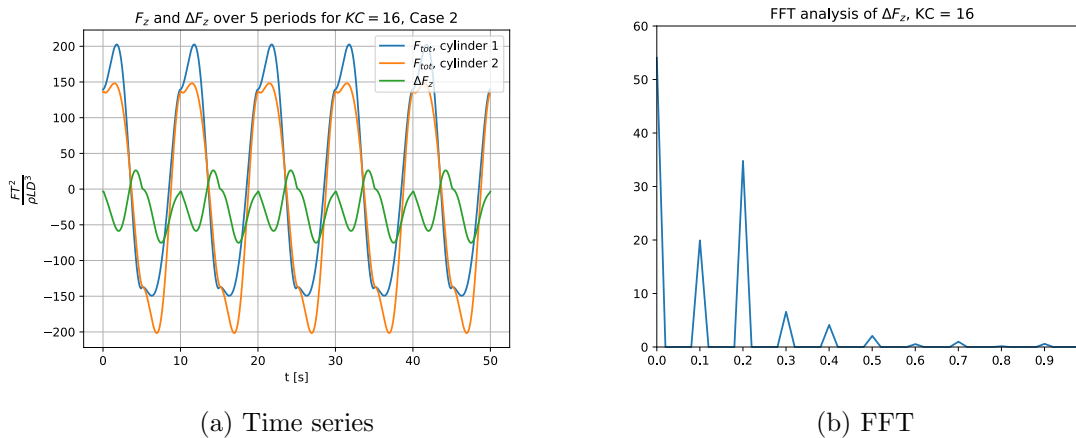


Figure 6.40: Example time series of Equation (6.18) for a single cylinder at  $KC = 20$  and  $T = 10s$ .

The resulting time series in Figure 6.40 retains the form usually associated with the Morison equation. This is more easily recognized for the drag term, which has the same form as in Figure 6.34. In an effort to relate this back to the experiments and ordinary usage of Morison, Case 2 with  $\frac{S}{D} = 2$  is modeled for full-scale. Force coefficients are extracted from the experimental results, and  $C_b$  is converted to  $C_D$  using Equation (2.32). No Froude-Kriloff forces are included, meaning that  $C_M = C_a$ . Figure 6.41 presents the resulting time series and FFT.



(a) Time series

(b) FFT

Figure 6.41: Time series and FFT of  $F_z$  and  $\Delta F_z$  using Equation (6.18),  $KC = 16$  and  $f_r = 0.8$ .

Note the amplitude of the  $2\omega$  force contribution in Figure 6.41b for the difference force. The simplified model using Equation (6.18), Equation (6.19) and Equation (6.20) with  $f_r = 0.8$  predicts  $\Delta F_z^{2\omega} = 35$  for  $KC = 16$ . This is equivalent to the experimental results for  $\frac{S}{D} = 2$  as shown in Figure 6.12, although this is likely coincidental. It also successfully predicts that the  $2\omega$  contribution dominates the difference forces at this  $KC$  number, as well as the formation of a mean difference force.

The time series from Figure 6.41b also displays a similar trend previously viewed in both the experiments and the model from Section 6.3. All positive peaks of Cylinder 1 are taller compared to Cylinder 2, and vice versa for the negative peaks of Cylinder 2. In order to relate this closer to the experiments, a comparison between the time series of the simplified model and the experiments at  $KC = 21$  is shown in Figure 6.42.

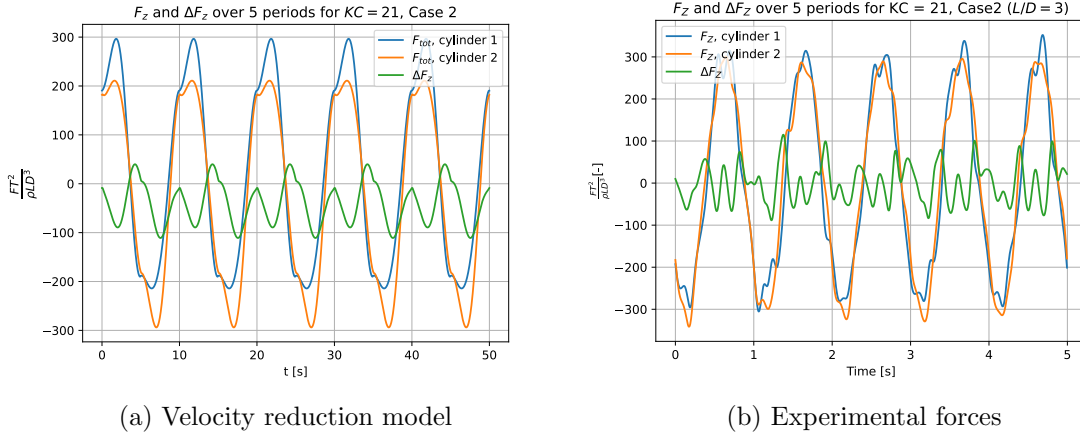


Figure 6.42: Comparison between the simplified model from Equation (6.18) and the corresponding experimental time series

The first thing of note is that the non-reduced peaks from the Morison model in Figure 6.42a match those from the experiments in Figure 6.42b reasonably well. Comparing the two, the Morison model slightly underestimates the experimental peaks, though not by much. An apparent drawback to the model is that it underestimates the cylinders' reduced peaks.

Another observation is that the experimental results also appear to have larger higher-order frequency contributions, as seen by the more frequent and localized peaks in Figure 6.42b. Although not surprising, it is clear that the Morison model is unable to accurately estimate the higher-order frequencies, and that these terms require separate modeling. The presence of higher-order frequencies might also explain the underestimation of the non-reduced peaks, but not the reduced ones.

The simplified wake model should be compared to the regular Morison equation, to see how they compare to each other and to evaluate which of the two approximates the experiments best. Figure 6.43 shows both the regular Morison equation and the wake reduction model plotted together for  $KC = 16$ . The time series for regular Morison is created using  $C_D = 1$  and  $C_a = 1.2$ . Comparing the two shows that regular usage of the Morison equation significantly underestimates the experimental peaks from Figure 6.10b. In contrast, only the reduced peaks for the reduced velocity model significantly miss the experimental values.

Additionally, the difference forces obtained through the use of the ordinary Morison equation are simply wrong, both qualitatively and quantitatively. It is clear that the velocity reduction needs to be accounted for if the difference forces are to be estimated correctly.

Only Case 2 has been presented on this topic. The simple reason is that the exact same observations was made for Case 1, and Case 2 is therefore deemed a good representation of the velocity reduction model. The concluding remarks on the model proposed by Equa-

tion (6.18), Equation (6.19) and Equation (6.20) are that it is capable of estimating the non-reduced peaks reasonably well. By introducing  $f_r$  like in Equation (6.21) it becomes possible to estimate  $\Delta F_z^{2\omega}$  accurately, but with the trade-off of underestimating the reduced peaks. Overall, the velocity reduction model shows promise and should be explored in further work.

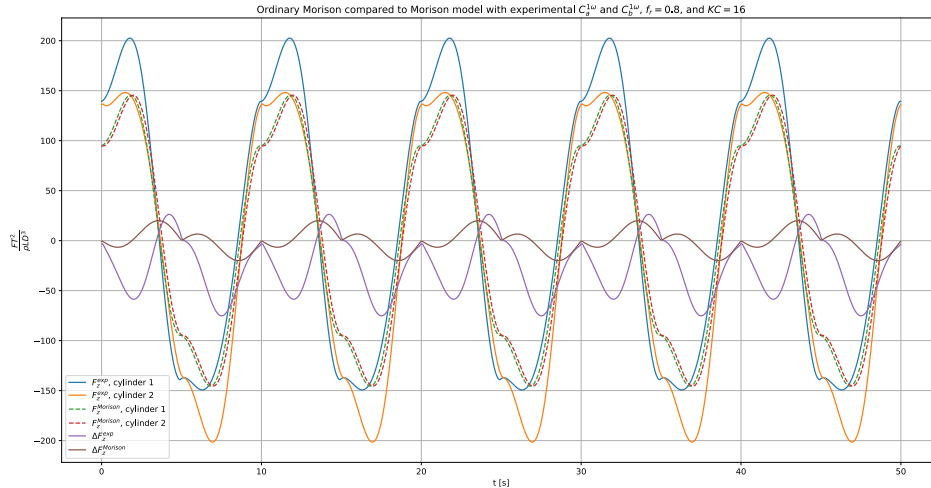


Figure 6.43: Comparison between the simplified wake model and ordinary Morison with  $C_d = 1$  and  $C_a = 1.2$ . The  $C_a$  value is chosen based on the findings from DNV-RP-C205 in Section 5.4.

Although showing a lot of promise, there certainly are major issues with the wake velocity reduction as an explanatory model for the  $2\omega$  force contributions. Firstly, the determination of the reduction factor  $f_r$  is currently guesswork and is assumed to be between  $f_r = 0.7$  and  $f_r = 0.9$ . It is clear that this factor will be highly dependent on both the spacing ratio and the KC number. Determining these dependencies is highly relevant for future investigations. A suggestion for the starting point for this further work may be Stephen Pope’s mean velocity solution for the plane wake. The characteristic velocity difference is

$$U_s(x) = U_c - \langle U(x, 0, 0) \rangle, \quad (6.23)$$

where  $U_c$  is the characteristic convective velocity or free stream velocity. This is, however, stationary and is related to already developed wakes. It is therefore not necessarily directly applicable towards the purposes of this thesis [18], especially for small KC numbers when inertial forces dominate. More investigations are needed to determine the best way to approximate the velocity reduction.

Furthermore, the velocity reduction is insufficient as an explanatory model for the lift forces that occur. It also does not explain some of the forces dependencies of the inflow angle  $\theta$  shown by the staggered arrangement. As a result, it seems somewhat reasonable as an explanatory model for tandem arrangements but insufficient or unjustified for small  $\theta$  contributions. It is clear that more research is required on this topic before a more definite model can be proposed.

## 6.6 Summarizing Comments and Load Formulation

This thesis has considered two experimental studies of 3D square cylinders in harmonic oscillatory flow, tandem, and staggered arrangements. A Wadam simulation has also been conducted to compare experimental and potential theory added mass forces. These endeavors have uncovered hydrodynamic 3D effects and interaction between the closely spaced cylinders.

Cylinders of three different lengths have been tested. A comparison of the different lengths shows that the force signal becomes more high-frequent for smaller cylinders. This indicates that the vortex shedding around 3D ends is more high-frequent compared to longer cylinders, and is supported by Li [13] who noted a broader St number spectra around the 3D ends. Furthermore, force magnitudes for tandem arrangements appeared unaffected by a change in  $L$ , unlike for staggered arrangements where  $1\omega$  amplitudes showed large  $L$  dependency. These effects are not yet understood and more research on the topic is warranted to understand and quantify the  $\theta$  and 3D end effects.

The primary indication of interaction from the experiments between the cylinders is as stated previously by Reiten [19] and confirmed by Hals [8], still the  $2\omega$  force amplitudes. It was seen that the two cylinders experience reduced force peaks when in downstream flow during the oscillation. The current hypothesis has therefore been that a wake velocity reduction works on each half-cycle during the oscillation. The reduced peaks occur at separate half-cycles between the cylinders, meaning that the resulting force is  $2\omega$  and acts on the two cylinders with a  $180^\circ$  phase difference. This gives a sign shift when subtracted and  $\Delta F_z^{2\omega}$  becomes about double  $F_z^{2\omega}$ . Based on this information and the Morison equation, a velocity reduction model was proposed.

$$\frac{FT^2}{\rho LD^3} = \frac{1}{2}\pi^2 C_m(f_v KC) \cos(\omega t - kx) + \frac{1}{2}C_d(f_v KC)^2 \sin(\omega t - kx)|\sin(\omega t - kx)| \quad (6.24)$$

Although showing a lot of promise for tandem arrangements, there are major issues with using the wake velocity reduction as an explanatory model. Firstly, the determination of the reduction factor  $f_r$  is currently guesswork and a proper relation for  $f_r$  is required for proper use. Secondly, velocity reduction is insufficient as an explanatory model for the lift forces observed for staggered arrangement. This is a topic that needs much more research before any definite solution is proposed.

Another proposition may be to evaluate all the harmonic force components separately with individual force coefficients for each harmonic frequency. Remember, the higher-order frequency coefficient in this thesis is evaluated qualitatively using fictitious acceleration and velocity. More experiments are required to determine these coefficients with real accelerations and velocities. Such a tentative formulation proposed by Kristiansen may read as

$$F_D^{n\omega} = \rho D \sum_{n=1}^{\infty} C_D^{n\omega}(S, G, KC, \theta, \text{Re})u_n, \quad (6.25)$$

where  $S$  is spacing or a case-specific parameter,  $G$  is the cross-sectional geometry and  $u_n$  is the velocity component of frequency  $n$ . The Re number is not treated already in the thesis but is expected to change the coefficients if large variations between experiments

and actual use cases occur. In mathematical terms, this sum may go to infinity, but in practical terms, it may be sufficient to use up until  $4\omega$ . An additional important note is that the experimental efforts until now have been forced harmonic studies. It is therefore not sufficient to get a complete and comprehensive understanding of other untested factors such as irregular sea states. The wavelength-diameter ratio is another factor that will be important in practical applications. These same efforts are required for lift forces as well, which was negligible in tandem but increased quickly with  $\theta$ .

It is evident that the current research efforts are still in its early stages. A substantial amount of additional experimental and numerical investigations are required to uncover the needed relationships.

## Conclusions and Further Work

The presented work has uncovered a set of results indicating significant hydrodynamic effects. Of these are hydrodynamic interaction loads particularly treated. Additionally, hydrodynamic 3D end effects and higher order frequency amplitudes stochasticity are also uncovered. This chapter will conclude the main findings of the thesis, and provide suggestions for further work.

### 7.1 Conclusions

The hydrodynamic loads and interaction, and their dependencies on the KC number, spacing ratio, and inflow angle have been explored. Tandem arrangements show that significant wake interactions are present and that this interaction is dependent on the spacing ratio and KC number. The  $1\omega$  forces in drag direction decrease when the cylinders are placed in closer proximity, while the  $2\omega$  forces increase. This results in a higher total force for  $\frac{S}{D} = 2$  compared to  $\frac{S}{D} = 1$ . Evidence that the  $2\omega$  forces of the two cylinders are  $180^\circ$  out of phase is uncovered, indicating that  $\Delta F_z^{2\omega}$  is about twice the size of  $F_z^{2\omega}$ . The current hypothesis is that this is due to a velocity reduction on separate oscillation half-cycles.

Staggered arrangements were tested experimentally, and large  $\theta$  dependencies were uncovered for both lift and drag. Unlike tandem arrangement, where the lift forces were negligible compared to drag, staggered arrangement showed an explosion in the lift forces. The drag forces are also increased when an inflow angle is introduced. Clear trends are seen across both  $L$  and KC number for  $1\omega$ , while no coherent trend for  $2\omega$  forces could be seen, neither as a function of the KC number nor  $L$ . The  $1\omega$  damping forces however displayed good correspondence with maximum drag and lift indicated by Zdravkovich.

The experiments show indications that vortex-shedding frequencies are more broad-banded at the 3D ends. Smaller cylinder lengths exhibited higher-frequency force responses, while the magnitudes remained relatively consistent with increasing  $L$  in tandem arrangements. Staggered arrangements displayed increased force magnitudes across all harmonic components when increasing  $L$ . Further investigations are needed to fully understand and quantify these 3D effects.

Comparisons with 2D computational fluid dynamics (CFD) models showed good agree-

ment with  $1\omega$  forces but overestimated  $2\omega$  and higher frequency components. Recommendations for enhancing future CFD work were provided.

Lastly, the evaluation of load formulations based on the Morison equation and the simplified wake model by Kristiansen indicated the potential of a continuous sine function to capture forces in tandem arrangements. However, these formulations fell short in representing high-frequency force components, lift forces, and certain  $\theta$  dependencies. Further exploration is required to develop an improved load formulation.

## 7.2 Further Work

While the experiments have provided indications of various phenomena, definitive conclusions remain challenging. It is important to emphasize that the research is still in its early stages. Promising results have been observed by using velocity reduction for addressing  $2\omega$  forces for tandem cylinders, but further investigations are necessary to pinpoint these relations more accurately. Furthermore, this formulation does not explain the large  $\theta$  dependency, higher order frequency contributions, and observed lift forces.

Specific suggestions for future research directions are suggested to achieve the long-term objectives of the research. The following suggestions are made based on the observations and shortcomings experienced during this work:

- A large degree of stochasticity is observed for the highest order frequencies in tandem arrangement and for  $2\omega$  or higher in staggered arrangement. Repetition testing is recommended to improve the understanding of these phenomena and dependencies.
- It is possible that a future load formulation needs to be the form of Equation (6.25). This necessitates more studies to uncover quantitatively correct  $2\omega$ ,  $3\omega$ , and  $4\omega$  added mass and damping coefficients. Further experiments where the loads oscillate with these frequencies can be considered for this endeavor.
- The noise from the rig, as outlined in Section 3.4 and Section 4.4, made the testing of the heavier cases difficult. Redesign of the experimental rig to make the system stiffer should be considered. This will make it possible to more accurately evaluate the  $4\omega$  contributions and cases with multiple cylinders such as Case 3.
- More sophisticated CFD strategies should be explored to make the numerical and experimental results more compatible. A more mature CFD strategy may help validate and acquire data for future research. This is also of great value as such simulations can be used to evaluate cases that are not possible experimentally due to rig limitations.
- Lastly, a proper investigation of the velocity reduction is needed. The Morison model with velocity reduction on each half-cycle showed promise to estimate the  $2\omega$  forces, but the exact relationship is not yet known. A specific study on this factor is required to pinpoint its relationships with spacing and the KC number.

# Bibliography

- [1] E. Bachynski-Polić, T. Kristiansen and D. Myrhaug. *Marine Dynamics*. Department of marine technology, NTNU, 2019.
- [2] D. Biermann and W.H.Jr. Herrnstein. ‘The interference between struts in various combinations’. In: *National Advisory Committee for Aeronautics* 41.468 (1933), pp. 515–524.
- [3] DNV. *Energy transition outlook 2022 - a global and regional forecast to 2050*. DNV, 2022.
- [4] RECOMMENDED PRACTICE DNV-RP-C205. *ENVIRONMENTAL CONDITIONS AND ENVIRONMENTAL LOADS*. DNV, 2010.
- [5] A.S. Elminshawy et al. ‘Simulation and experimental performance analysis of partially floating PV system in windy conditions’. In: *Solar Energy* 230 (2021), pp. 1106–1121.
- [6] Equinor. *Will test floating solar off Frøya*. 2021. URL: <https://www.equinor.com/news/archive/20210114-test-offshore-solar>. (accessed: 28.09.2022).
- [7] O.M. Faltinsen. *Sea Loads on Ships and Offshore Structures*. Cambridge University Press, 1993.
- [8] Petter G. Hals. *Numerical Experimental Studies on the Hydrodynamic Loads on Square-shaped and Diamond-shaped Cylinders in Close Proximity Exposed to a Forced Oscillatory Fluid Flow*. Department of Marine Technology, NTNU, 2023.
- [9] G.H. Keulegan and L.H Carpenter. ‘Forces on Cylinders and Plates in an Oscillating Fluid.’ In: *Journal of Research of the National Bureau of Standards* 60 (1958), pp. 423–440.



- [10] T. Kristiansen. *Aspects and theory on multi-modular marine structures*. Presentation. 2022.
- [11] T. Kristiansen et al. ‘A flexible multi-torus solar island concept’. In: *The International Workshop on Water Waves and Floating Bodies* 36 (2021).
- [12] T. Kristiansen et al. ‘Wake interaction in high-KC oscillatory flow’. In: *The International Workshop on Water Waves and Floating Bodies* 38 (2023).
- [13] H. Li. ‘TWO STAGGERED FINITE CIRCULAR CYLINDERS IN CROSS-FLOW’. MA thesis. Department of Mechanical Engineering, University of Saskatchewan, 2008.
- [14] W.A. Mair and D.J. Maull. ‘Aerodynamic Behaviour of Bodies in the Wake of Other Bodies’. In: *Transactions Royal Society* 269 (1971), pp. 425–437.
- [15] F. Mentzoni. ‘Hydrodynamic Loads on Complex Structures in the Wave Zone’. PhD thesis. Department of marine technology, NTNU, 2020.
- [16] K Mikkelsen. *Three-dimensional experimental investigation of hydrodynamic forces and wake interaction between two or more cylinders in large-amplitude oscillatory flow - Pre-project*. Department of marine technology, NTNU, 2022.
- [17] J.R. Morison, J.W Johnson and S.A Schaaf. ‘The Force Exerted by Surface Waves on Piles.’ In: *The Journal of Petroleum Engineering* 2 (1950), pp. 149–154.
- [18] S. Pope. *Turbulent Flows*. Cambridge University Press, 2000.
- [19] H. Reiten. ‘Two-dimensional Numerical and Experimental Investigation of Hydrodynamic Forces and Wake Interaction between Two or more Square Cylinders in Large-amplitude Oscillatory Flow’. MA thesis. Department of marine technology, NTNU, 2022.
- [20] O. Reynolds. ‘An Experimental Investigation of the Circumstances which determine whether the Motion of Water shall be Direct or Sinuous, and of the Law of Resistance in Parallel Channels’. In: *Royal Society Open Science* 174 (1883), pp. 935–982.
- [21] M. Rosa-Clot and G.M Tina. *Floating PV Plants*. Elsevier Science and Technology, 2020.
- [22] T. Sarpkaya. ‘Forces on Cylinders and Spheres in a Sinusoidally Oscillating Fluid’. In: *Journal of Applied Mechanics* 42.1 (Mar. 1975), pp. 32–37. URL: <https://doi.org/10.1115/1.3423549>.

- [23] A. Sommerfeld. ‘Ein beitrag zur hydrodynamischen erklaerung der turbulenten fluessigkeitsbewegungen’. In: *Int. Congr. Math* 3 (1908), pp. 116–124.
- [24] Ocean Sun. *Magat*. 2020. URL: <https://oceansun.no/project/test-project/>. (accessed: 28.09.2022).
- [25] United Nations. *Renewable energy – powering a safer future*. URL: <https://www.un.org/en/climatechange/raising-ambition/renewable-energy>. (accessed: 27.09.2022).
- [26] M.M. Zdrakovich. ‘REVIEW-Review of Flow Interference Between Two Circular Cylinders in Various Arrangements.’ In: *Journal of Fluid Mechanics* 99 (1977), pp. 618–633.

# Appendix A

## DNV-RP-C205

**Table D-2 Analytical added mass coefficient for three-dimensional bodies in infinite fluid (far from boundaries). Added mass is  $m_A = \rho C_A V_R$  [kg] where  $V_R$  [m<sup>3</sup>] is reference volume. (Continued)**

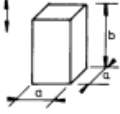
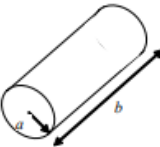
Body shape		Direction of motion	$C_A$		$V_R$
			$b/a$	$C_A$	
Square prisms		Vertical			$a^2 b$
			1.0	0.68	
			2.0	0.36	
			3.0	0.24	
			4.0	0.19	
			5.0	0.15	
			6.0	0.13	
			10.0	0.08	
Right circular cylinder		Vertical	$b/2a$	$C_A$	$\pi a^2 b$
			1.2	0.62	
			2.5	0.78	
			5.0	0.90	
			9.0	0.96	
			$\infty$	1.00	

Figure A.1: Analytical added mass coefficients for three-dimensional bodies in infinite flow.

Source: [4]

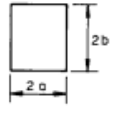
	$a/b = \infty$ $a/b = 10$ $a/b = 5$ $a/b = 2$ $a/b = 1$ $a/b = 0.5$ $a/b = 0.2$ $a/b = 0.1$	Vertical	$\pi a^2$	$\beta_1 \rho \pi a^4$ or $\beta_2 \rho \pi b^4$		
				$a/b$	$\beta_1$	$\beta_2$
				0.1	-	0.147
				0.2	-	0.15
				0.5	-	0.15
				1.0	0.234	0.234
				2.0	0.15	-
				5.0	0.15	-
				$\infty$	0.125	-

Figure A.2: Analytical added mass coefficients for two-dimensional or infinitely long square.

Source: [4]

# Appendix B

## Force Plots and Results

### B.1 Harmonic Forces - Small and Medium

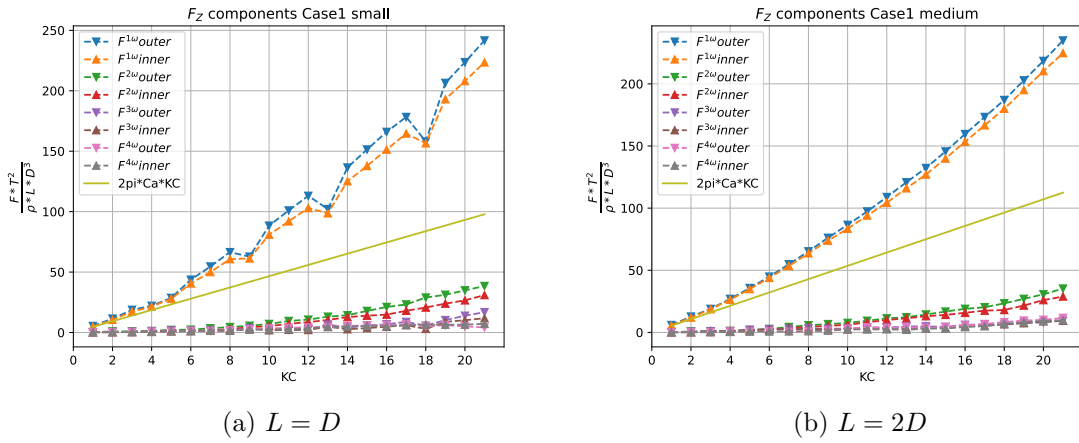


Figure B.1: Harmonic force amplitudes for  $L = D$  and  $L = 2D$ , Case 1 ( $\frac{S}{D} = 1$ )

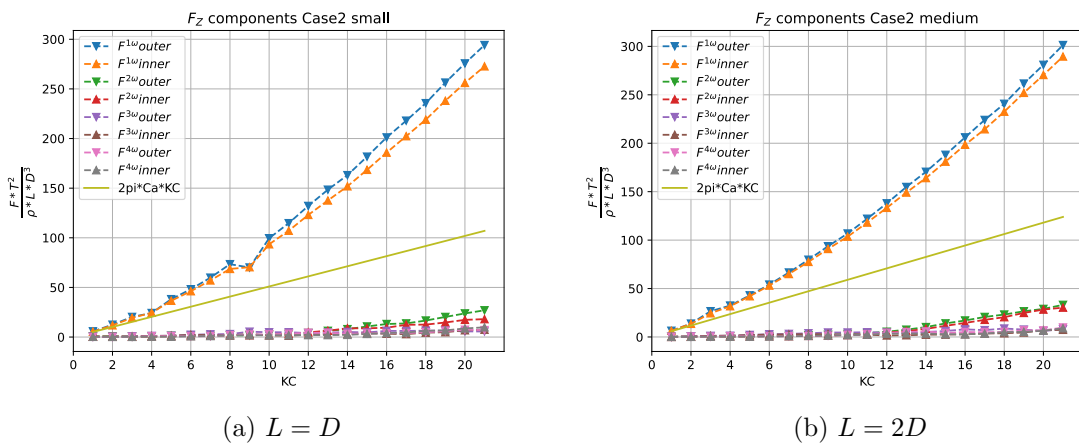
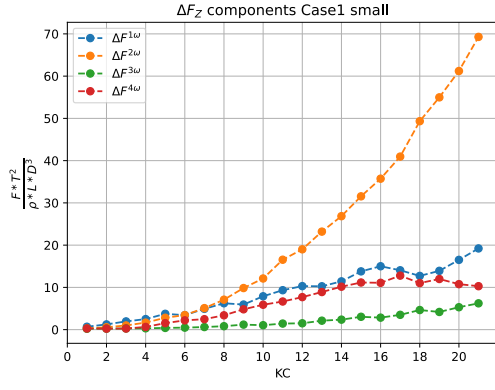
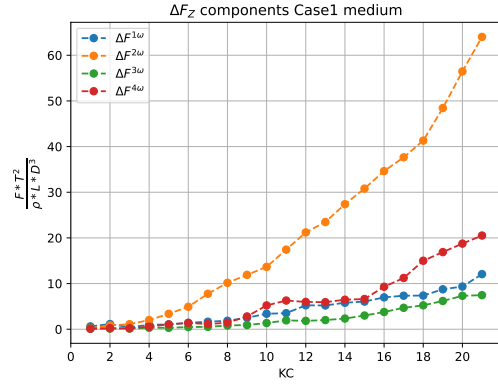
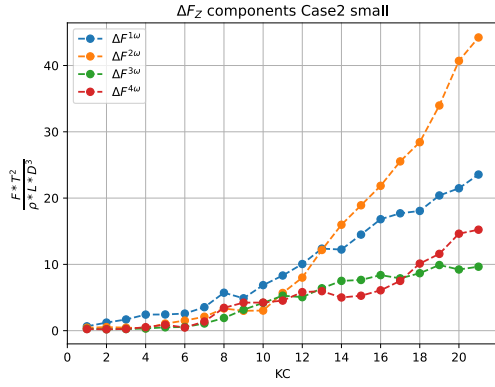
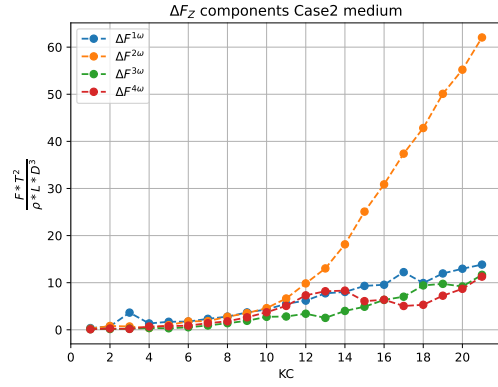
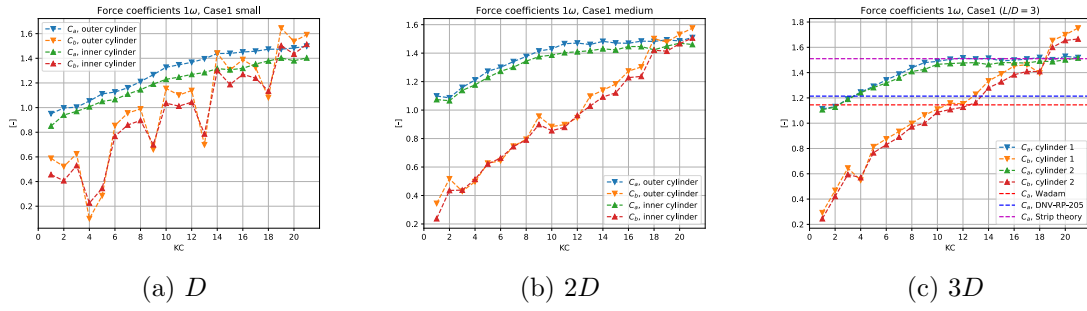
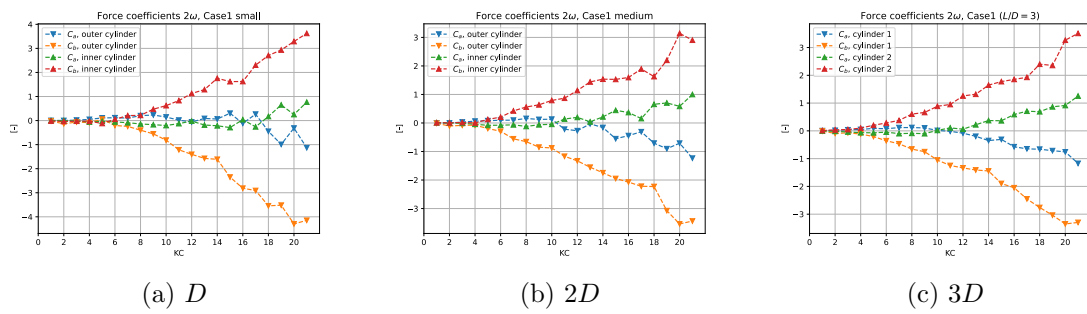
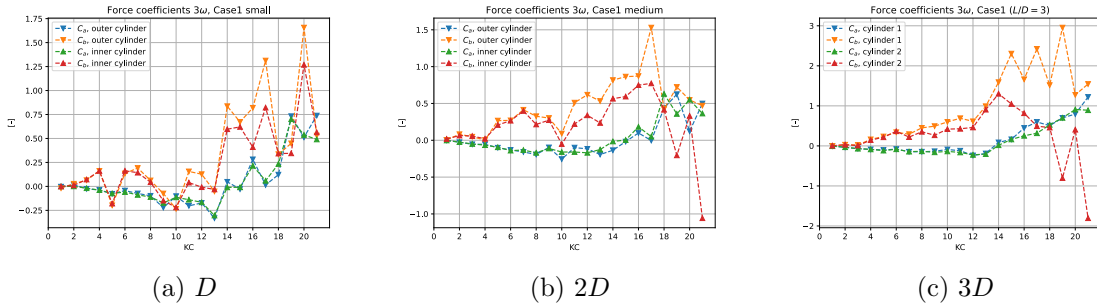
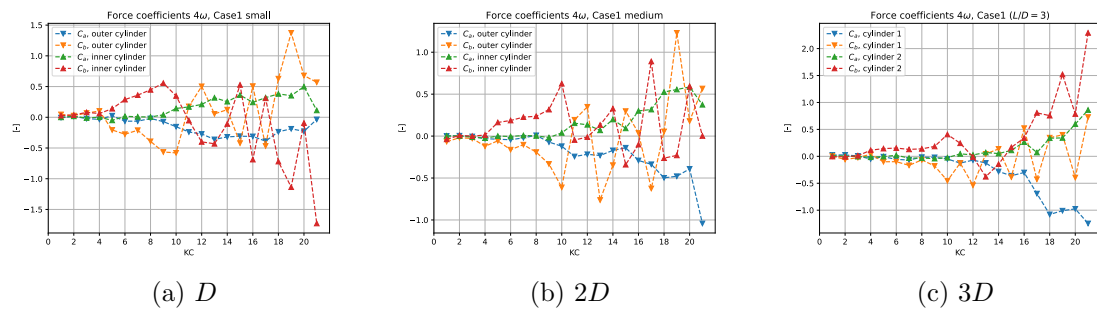


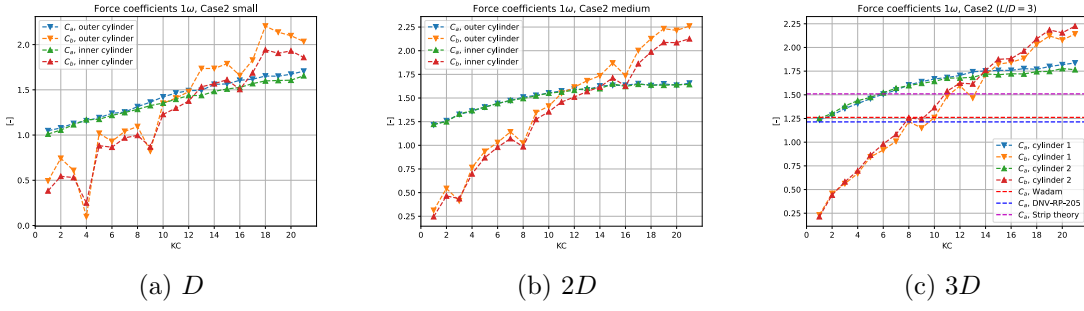
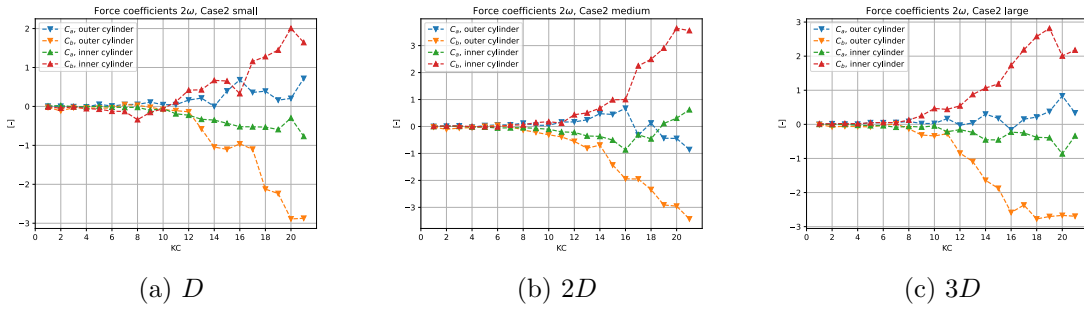
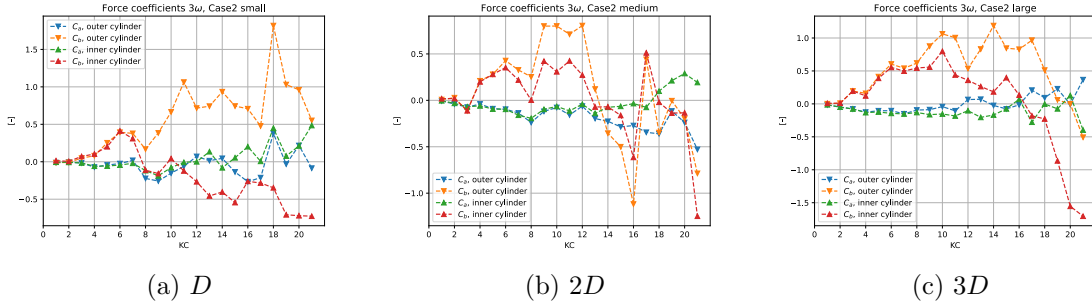
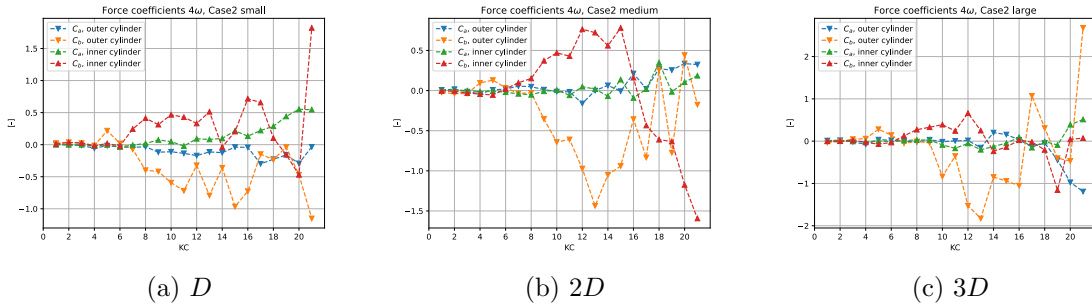
Figure B.2: Harmonic force amplitudes for  $L = D$  and  $L = 2D$ , Case 2 ( $\frac{S}{D} = 2$ )

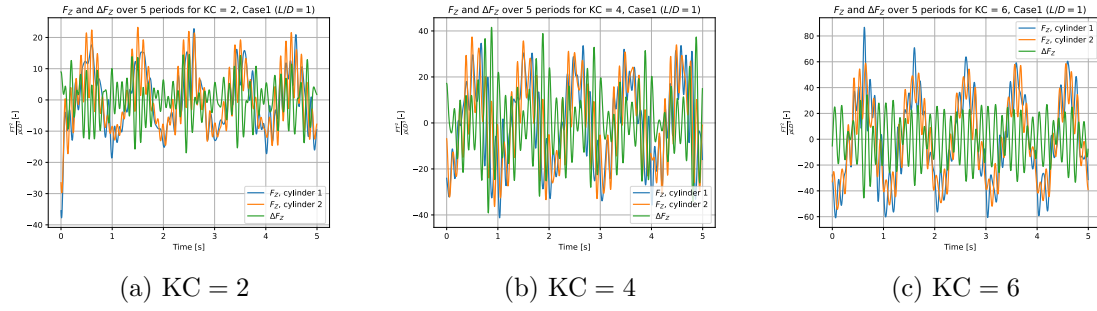
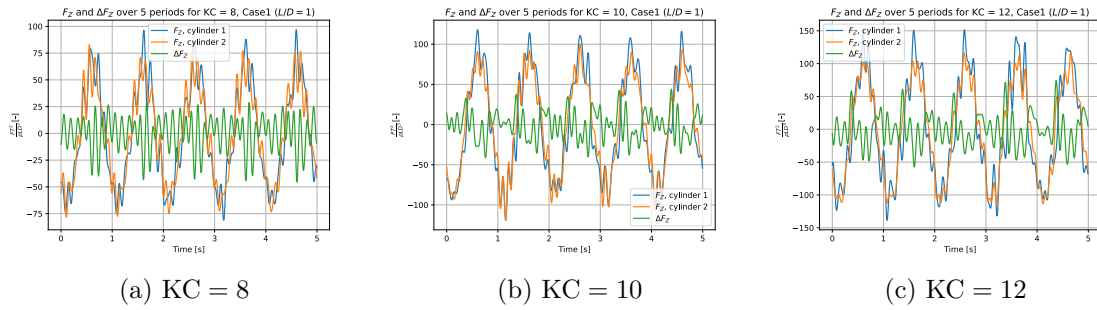
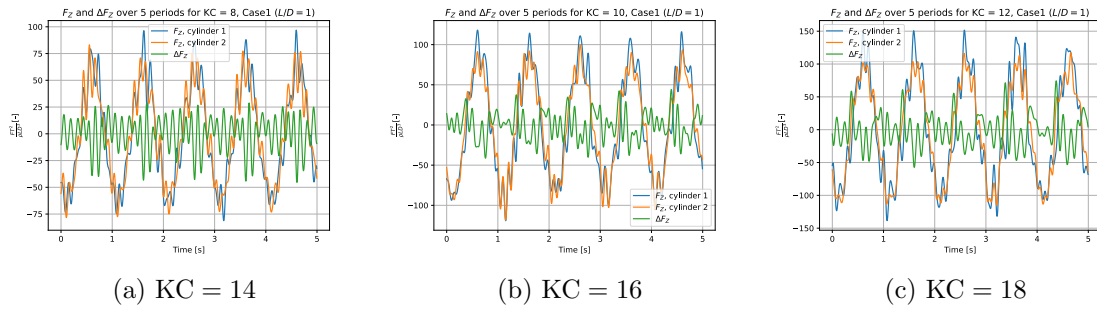
(a)  $L = D$ (b)  $L = 2D$ 
 Figure B.3: Difference force amplitudes for  $L = D$  and  $L = 2D$ , Case 1 ( $\frac{S}{D} = 1$ )
(a)  $L = D$ (b)  $L = 2D$ 
 Figure B.4: Difference force amplitudes for  $L = D$  and  $L = 2D$ , Case 2 ( $\frac{S}{D} = 2$ )

## B.2 Force Coefficients for Case 1


 Figure B.5:  $1\omega$  force coefficients for Case 1 for  $L = D$ ,  $L = 2D$  and  $L = 3D$ .

 Figure B.6:  $2\omega$  force coefficients for Case 1 for  $L = D$ ,  $L = 2D$  and  $L = 3D$ .

 Figure B.7:  $3\omega$  force coefficients for Case 1 for  $L = D$ ,  $L = 2D$  and  $L = 3D$ .

 Figure B.8:  $4\omega$  force coefficients for Case 1 for  $L = D$ ,  $L = 2D$  and  $L = 3D$ .

## B.3 Force Coefficients for Case 2


 Figure B.9:  $1\omega$  force coefficients for Case 2 for  $L = D$ ,  $L = 2D$  and  $L = 3D$ .

 Figure B.10:  $2\omega$  force coefficients for Case 2 for  $L = D$ ,  $L = 2D$  and  $L = 3D$ .

 Figure B.11:  $3\omega$  force coefficients for Case 2 for  $L = D$ ,  $L = 2D$  and  $L = 3D$ .

 Figure B.12:  $4\omega$  force coefficients for Case 2 for  $L = D$ ,  $L = 2D$  and  $L = 3D$ .

B.4 Time Series - Case 1 ( $\frac{S}{D} = 1$ )

 Figure B.13: Force time series of  $F_z$  and  $\Delta F_z$  for Cylinder 1 and Cylinder 2, Case 1 ( $\frac{S}{D} = 1$ )

 Figure B.14: Force time series of  $F_z$  and  $\Delta F_z$  for Cylinder 1 and Cylinder 2, Case 1 ( $\frac{S}{D} = 1$ )

 Figure B.15: Force time series of  $F_z$  and  $\Delta F_z$  for Cylinder 1 and Cylinder 2, Case 1 ( $\frac{S}{D} = 1$ )



## B.5 Time Series - Case 1 ( $\frac{S}{D} = 2$ )

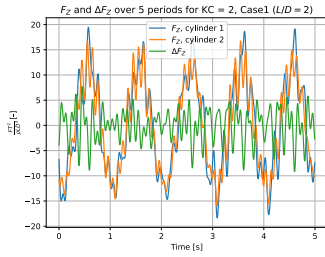
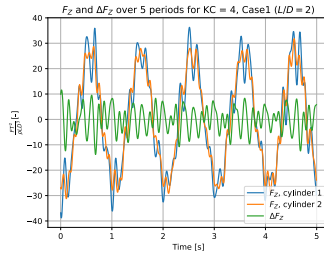
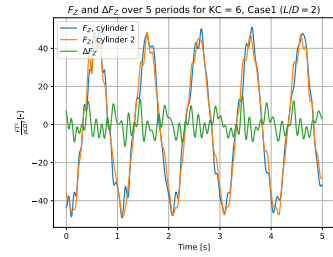

 (a)  $KC = 2$ 

 (b)  $KC = 4$ 

 (c)  $KC = 6$ 

Figure B.16: Force time series of  $F_z$  and  $\Delta F_z$  for Cylinder 1 and Cylinder 2, Case 1 ( $\frac{S}{D} = 2$ )

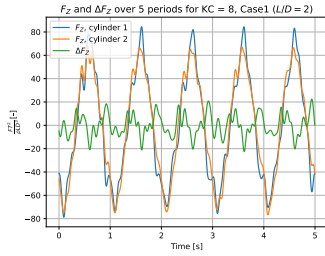
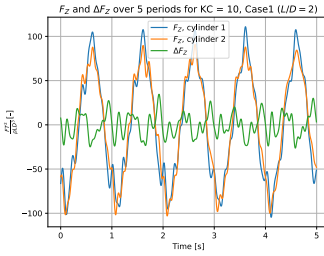
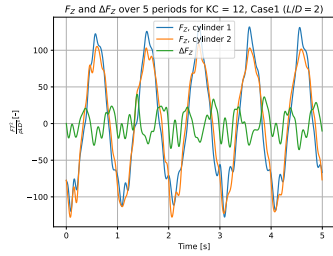

 (a)  $KC = 8$ 

 (b)  $KC = 10$ 

 (c)  $KC = 12$ 

Figure B.17: Force time series of  $F_z$  and  $\Delta F_z$  for Cylinder 1 and Cylinder 2, Case 1 ( $\frac{S}{D} = 2$ )

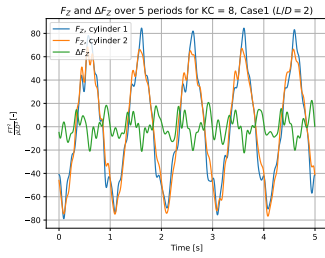
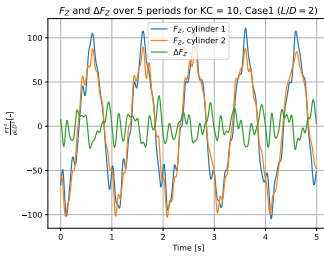
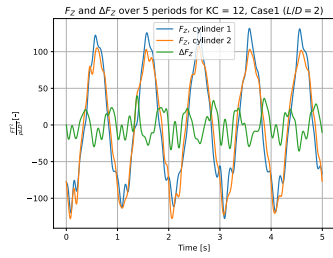

 (a)  $KC = 14$ 

 (b)  $KC = 16$ 

 (c)  $KC = 18$ 

Figure B.18: Force time series of  $F_z$  and  $\Delta F_z$  for Cylinder 1 and Cylinder 2, Case 1 ( $\frac{S}{D} = 2$ )

## B.6 Time Series - Case 1 ( $\frac{S}{D} = 3$ )

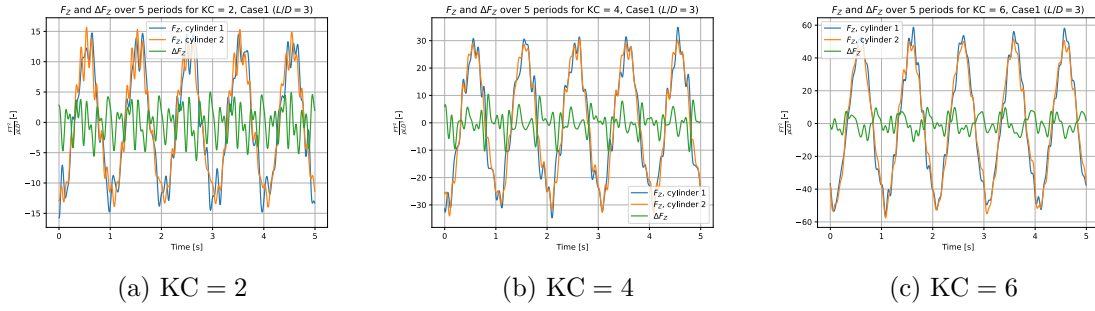


Figure B.19: Force time series of  $F_z$  and  $\Delta F_z$  for Cylinder 1 and Cylinder 2, Case 1 ( $\frac{S}{D} = 3$ )

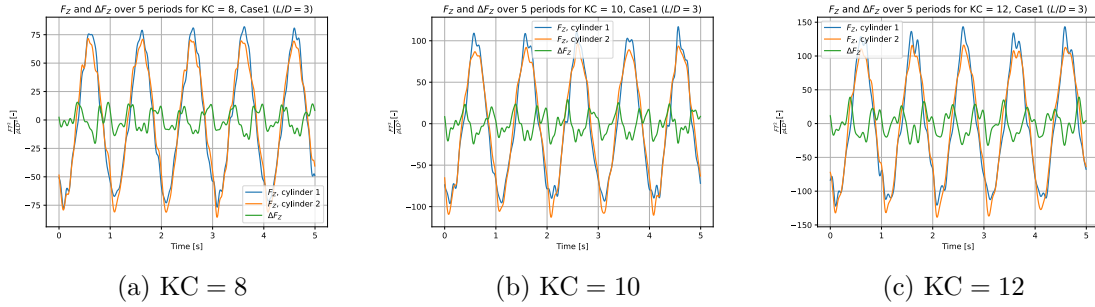


Figure B.20: Force time series of  $F_z$  and  $\Delta F_z$  for Cylinder 1 and Cylinder 2, Case 1 ( $\frac{S}{D} = 3$ )

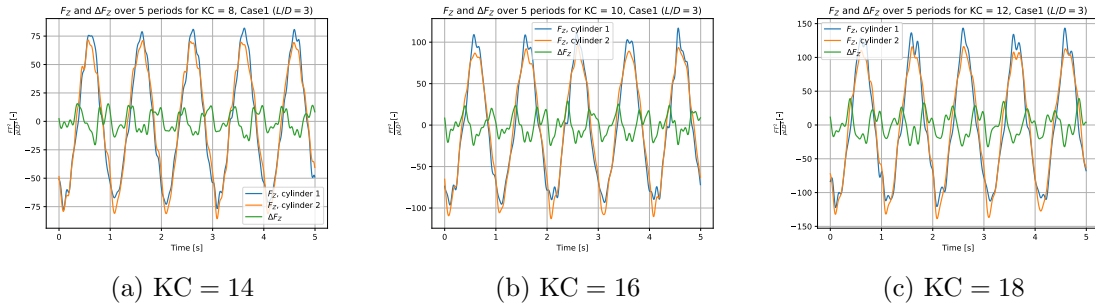
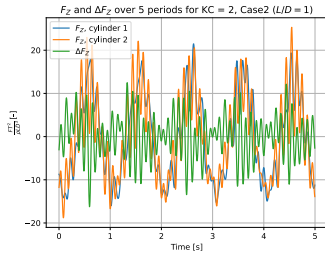
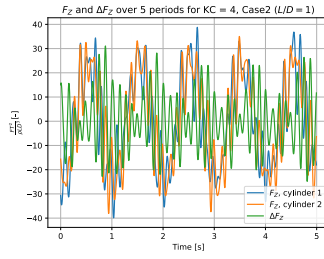
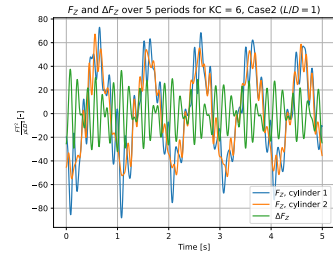
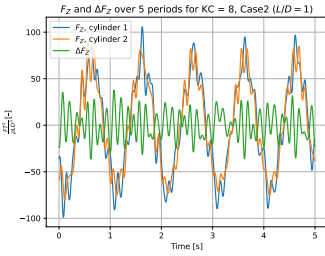
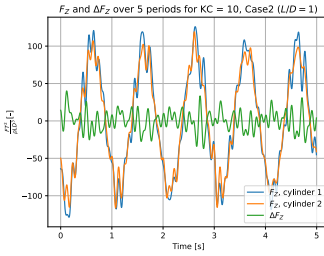
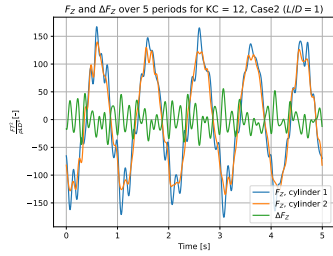
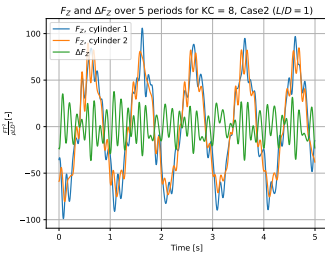
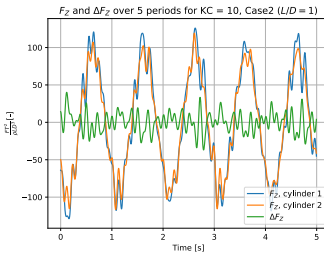
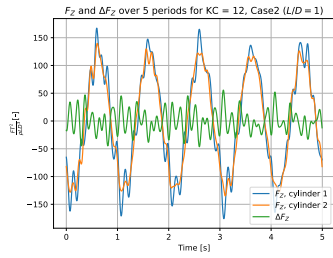


Figure B.21: Force time series of  $F_z$  and  $\Delta F_z$  for Cylinder 1 and Cylinder 2, Case 1 ( $\frac{S}{D} = 3$ )

B.7 Time Series - Case 2 ( $\frac{S}{D} = 1$ )
(a)  $KC = 2$ (b)  $KC = 4$ (c)  $KC = 6$ 
 Figure B.22: Force time series of  $F_z$  and  $\Delta F_z$  for Cylinder 1 and Cylinder 2, Case 2 ( $\frac{S}{D} = 1$ )
(a)  $KC = 8$ (b)  $KC = 10$ (c)  $KC = 12$ 
 Figure B.23: Force time series of  $F_z$  and  $\Delta F_z$  for Cylinder 1 and Cylinder 2, Case 2 ( $\frac{S}{D} = 1$ )
(a)  $KC = 14$ (b)  $KC = 16$ (c)  $KC = 18$ 
 Figure B.24: Force time series of  $F_z$  and  $\Delta F_z$  for Cylinder 1 and Cylinder 2, Case 2 ( $\frac{S}{D} = 1$ )

## B.8 Time Series - Case 2 ( $\frac{S}{D} = 2$ )

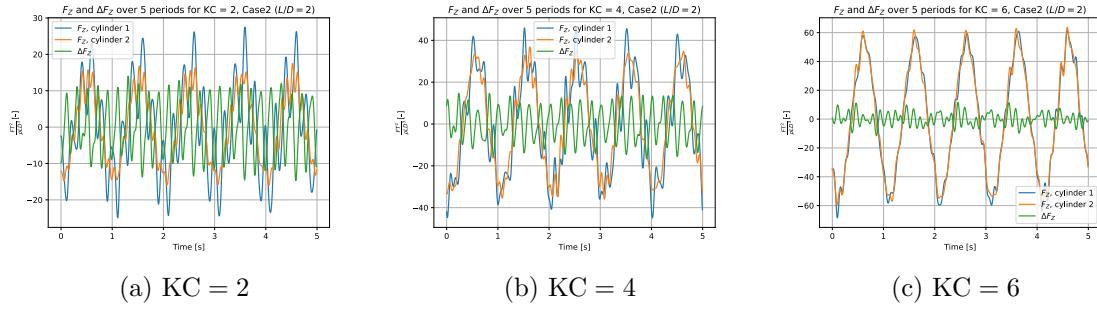


Figure B.25: Force time series of  $F_z$  and  $\Delta F_z$  for Cylinder 1 and Cylinder 2, Case 2 ( $\frac{S}{D} = 2$ )

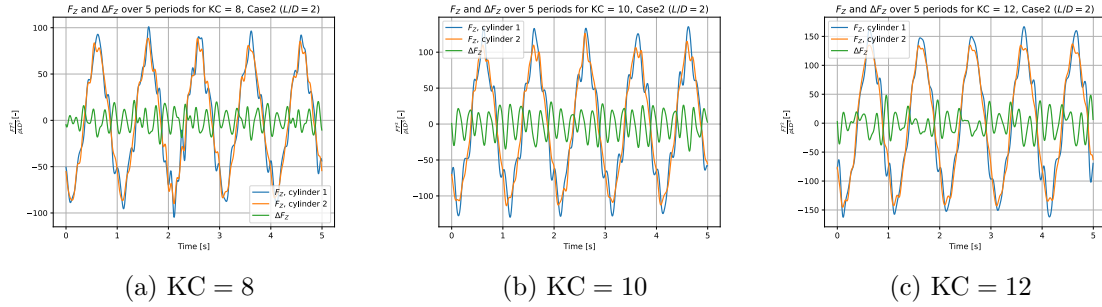


Figure B.26: Force time series of  $F_z$  and  $\Delta F_z$  for Cylinder 1 and Cylinder 2, Case 2 ( $\frac{S}{D} = 2$ )

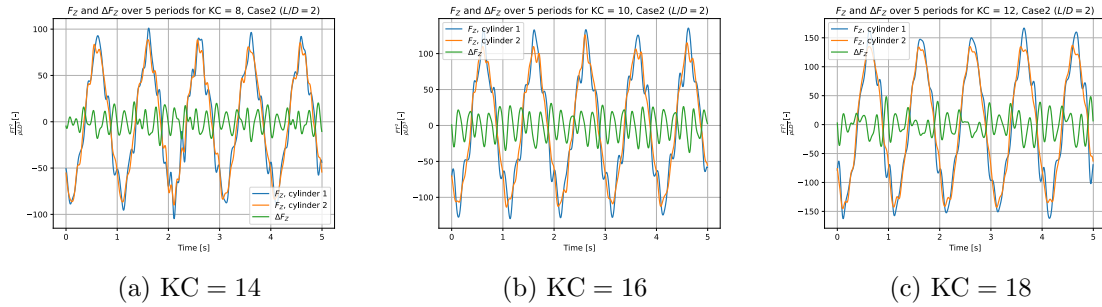


Figure B.27: Force time series of  $F_z$  and  $\Delta F_z$  for Cylinder 1 and Cylinder 2, Case 2 ( $\frac{S}{D} = 2$ )

## B.9 Time Series - Case 2 ( $\frac{S}{D} = 3$ )

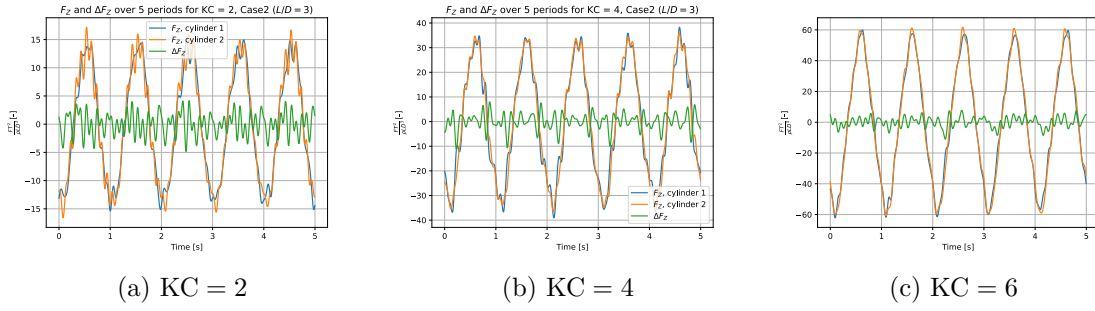


Figure B.28: Force time series of  $F_z$  and  $\Delta F_z$  for Cylinder 1 and Cylinder 2, Case 2 ( $\frac{S}{D} = 3$ )

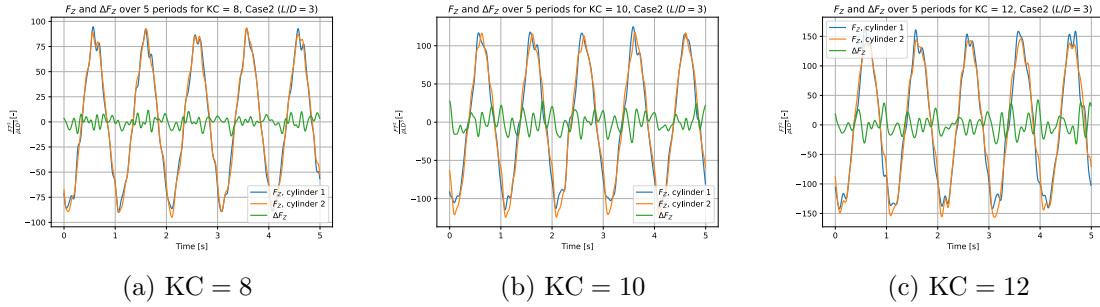


Figure B.29: Force time series of  $F_z$  and  $\Delta F_z$  for Cylinder 1 and Cylinder 2, Case 2 ( $\frac{S}{D} = 3$ )

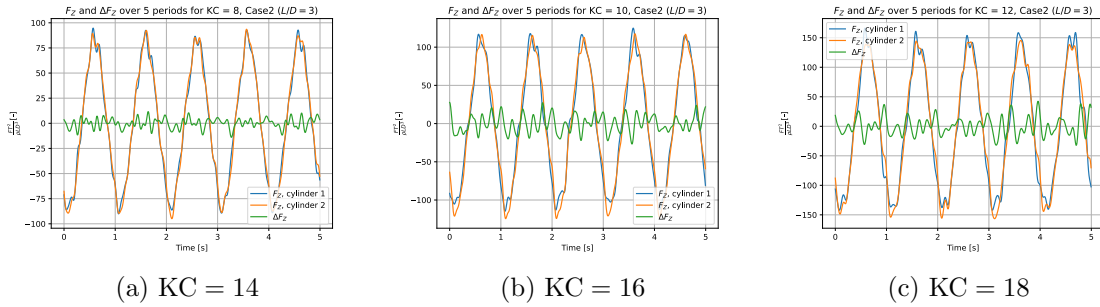


Figure B.30: Force time series of  $F_z$  and  $\Delta F_z$  for Cylinder 1 and Cylinder 2, Case 2 ( $\frac{S}{D} = 3$ )

# Miscellaneous

## C.1 $1\omega$ Viscous Forces for Staggered flow

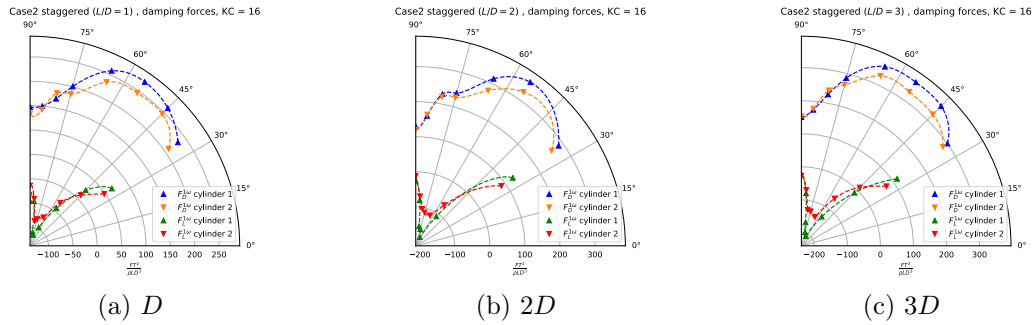


Figure C.1: Illustration of viscous forces at  $KC = 16$  for all three cylinder lengths.

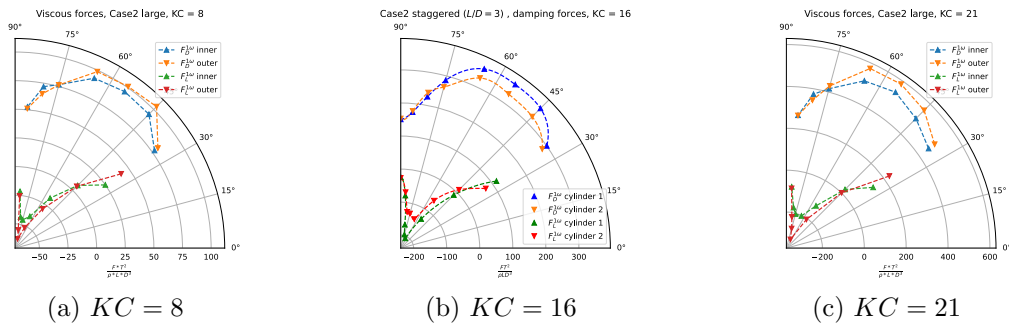


Figure C.2: Illustration of viscous forces at three different  $KC$  numbers for the large cylinder length.

## C.2 Harmonic Forces - Case 3

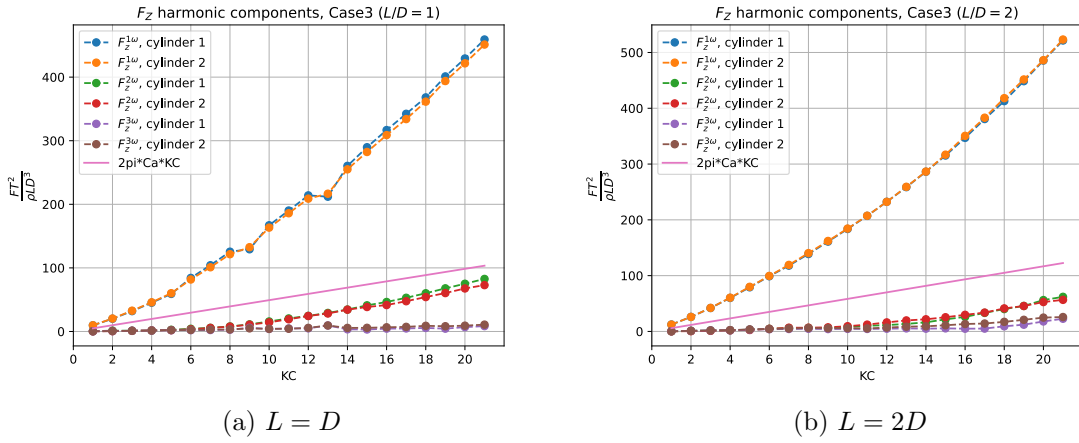


Figure C.3: Harmonic force amplitudes for  $L = D$  and  $L = 2D$

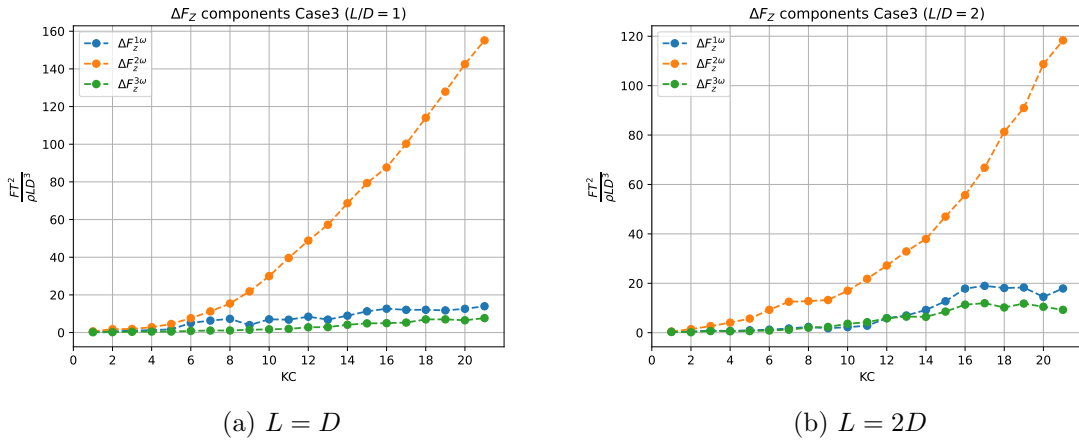


Figure C.4: Difference force amplitudes for  $L = D$  and  $L = 2D$

### C.3 Example of Velocity Reduction Factor Implementation

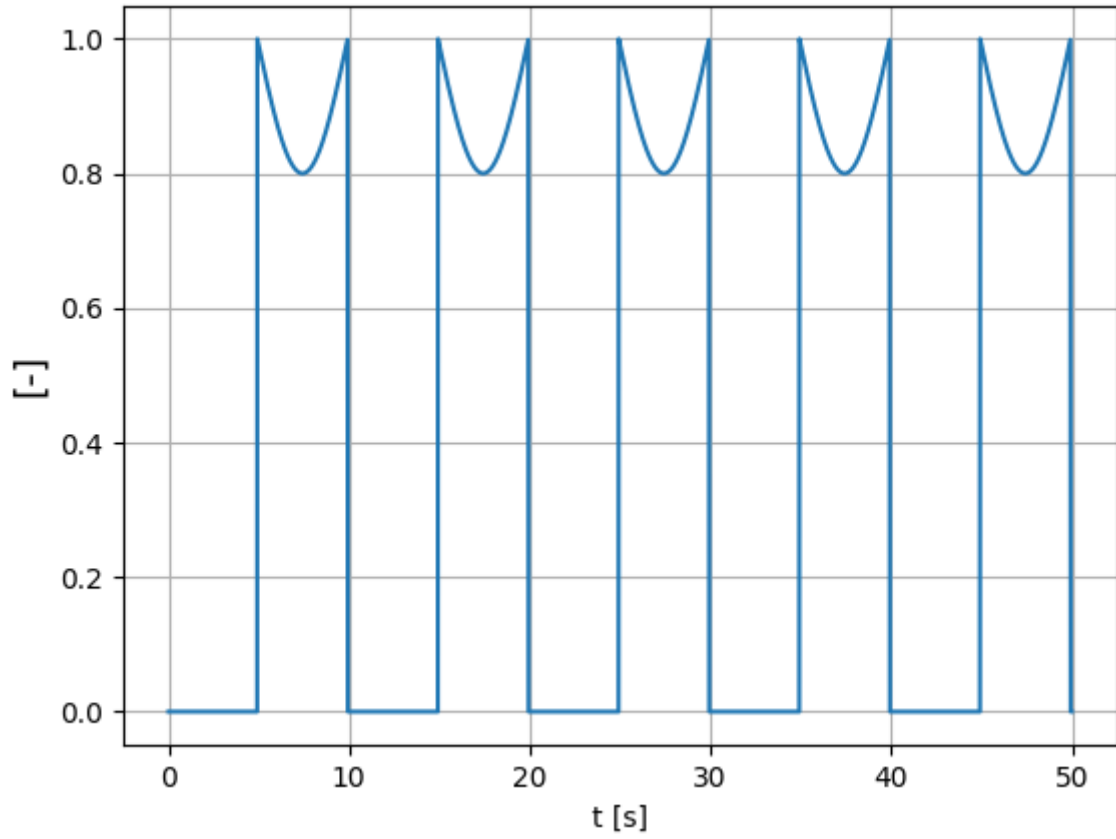


Figure C.5: Example of the implementation of  $f_r$  in the Morison model from Section 6.5.



# Appendix **D**

## Python Routines - Post-Processing

### D.1 Data Extraction from Wadam

```
import numpy as np
import math
import matplotlib.pyplot as plt
import scipy.signal as sp
import scipy.fftpack
import os

def get_data_WADAM(file_dir, new_file):
    file = open(file_dir)
    added_mass_counter = 0
    char_length_counter = 0
    T_set = set()
    a11 = []
    a22 = []
    a33 = []
    F1 = []
    F2 = []
    F1_phases = []
    F2_phases = []

    for line in file:
        if 'WATER DENSITY' in line:
            rho_content = line.split()
            rho = float(rho_content[4])

        if 'CHARACTERISTIC' in line:
            if char_length_counter == 2:
                char_length_content = line.split()
                char_length = float(char_length_content[4])
                char_length_counter += 1
            else:
                char_length_counter += 1
```

```
if 'HYDROSTATIC DATA:' in line:
    hydrostatic_content = []
    for i in range(6):
        hydrostatic_content.append(file.readline())
    disp_volume_row = hydrostatic_content[2].split()
    disp_mass_row = hydrostatic_content[3].split()
    WPLA_row = hydrostatic_content[5].split()

    volume = float(disp_volume_row[4])
    mass = float(disp_mass_row[6])
    WPLA = float(WPLA_row[5])

if 'WAVE PERIOD' in line:
    T_content = line.split()
    T_set.add(float(T_content[3]))
    continue

if 'ADDED MASS MATRIX' in line:
    if added_mass_counter == 0:
        added_mass_counter += 1
        continue

    else:
        added_mass_content = []
        for i in range(6):
            added_mass_content.append(file.readline())
        surge_row = added_mass_content[3].split()
        sway_row = added_mass_content[4].split()
        heave_row = added_mass_content[5].split()
        a11.append(float(surge_row[1]))
        a22.append(float(sway_row[2]))
        a33.append(float(heave_row[3]))
        continue

if 'H E A D I N G   A N G L E   =   0.00' in line:
    excitation1_content = []
    for i in range(16):
        excitation1_content.append(file.readline())
    F1_row = excitation1_content[13].split()
    F1.append(float(F1_row[3]))
    F1_phases.append(float(F1_row[4]))
    continue

if 'H E A D I N G   A N G L E   =   90.00' in line:
    excitation2_content = []
    for i in range(16):
        excitation2_content.append(file.readline())
    F2_row = excitation2_content[15].split()
    F2.append(float(F2_row[3]))
    F2_phases.append(float(F2_row[4]))
```

```
        continue

if new_file == 1:
    f = open("postprocessed_Wadam.txt", "w+")

    for i in range(len(a11)):
        if i == len(a11)-1:
            f.write(str(a11[i]))
        else:
            f.write(str(a11[i]) + ",")
    f.write("\n")

    for i in range(len(a22)):
        if i == len(a22)-1:
            f.write(str(a22[i]))
        else:
            f.write(str(a22[i]) + ",")
    f.write("\n")

    for i in range(len(a33)):
        if i == len(a33)-1:
            f.write(str(a33[i]))
        else:
            f.write(str(a33[i]) + ",")
    f.write("\n")

    for i in range(len(F1)):
        if i == len(F1)-1:
            f.write(str(F1[i]))
        else:
            f.write(str(F1[i]) + ",")
    f.write("\n")

    for i in range(len(F2)):
        if i == len(F2)-1:
            f.write(str(F2[i]))
        else:
            f.write(str(F2[i]) + ",")
    f.close()

T = sorted(list(T_set))
a11 = np.array(a11)
a22 = np.array(a22)
a33 = np.array(a33)
F1 = np.array(F1)
F2 = np.array(F2)
F1_phases = np.array(F1_phases) * math.pi/180
F2_phases = np.array(F2_phases) * math.pi/180

return char_length, rho, volume, mass, WPLA, T, a11, a22, a33, F1, F2,
    ↪ F1_phases, F2_phases
```

```

def plot_data_Wadam(file_dir, save_dir, new_file, save_plot):
    char_length, rho, volume, _, WPLA, T, A11, A22, A33, F1, F2,
    ↪ F1_phases, _ = get_data_WADAM(file_dir, new_file)
    FK, FK_phase = FK_SquareCylinder_prototype(file_dir, new_file)
    FI, FI_phases = FI_SquareCylinder_prototype(file_dir, new_file)

    g = 9.80665
    F_nondim = rho * g * volume * (1/char_length)

    plt.plot(T, A11, label='Surge', linestyle='dashed')
    plt.plot(T, A22, label='Sway')
    plt.plot(T, A33, label='Heave', linestyle='dashdot')
    plt.xlabel('Wave period [s]')
    plt.ylabel('Added mass [-]')
    plt.grid()
    plt.legend()
    plt.title('Added mass for surge and sway')
    if save_plot:
        plt.savefig(save_dir + "\AddedMass.svg", format='svg')
    plt.show()

    plt.plot(T, F1, label='Surge', linestyle='dashed')
    plt.plot(T, F2, label='Sway')
    plt.xlabel('Wave period [s]')
    plt.ylabel('Excitation force [-]')
    plt.grid()
    plt.legend()
    plt.title('Excitation for surge and sway')
    if save_plot:
        plt.savefig(save_dir + "\Excitation.svg", format='svg')
    plt.show()

    KC_list = np.linspace(0, 25, endpoint=True)
    Fm_list = np.zeros(len(KC_list))
    for i in range(len(KC_list)):
        Fm_list[i] = 2*math.pi * A11[-1] * KC_list[i]
    plt.plot(KC_list, Fm_list, label='2pi*Ca*KC')
    plt.xlabel('KC number [-]')
    plt.ylabel(r'$\frac{F_I * T^2}{\rho * L * D^3}$')
    plt.grid()
    plt.legend()
    plt.title('Mass force')
    plt.show()

    plt.plot(T, F1, label='Total Excitation')
    plt.plot(T, FI/F_nondim, label='Diffraction', linestyle='dashed')
    plt.plot(T, abs(FK)/F_nondim, label='Froude Krylov',
    ↪ linestyle='dashed')
    plt.xlabel('Wave period [s]')
    plt.ylabel(r'$\frac{F * L_{char}}{\rho * g * V}$ [-]')

```

```
plt.grid()
plt.legend()
plt.title('Amplitudes Excitation, Diffraction and FK force')
if save_plot:
    plt.savefig(save_dir + "\ExcitationComponents.svg", format='svg')
plt.show()

plt.plot(T, F1_phases, label='Excitation phases')
plt.plot(T, FI_phases, label='Diffraction phases', linestyle='dashed')
plt.xlabel('Wave period [s]')
plt.ylabel(r'$\phi$ [rad]')
plt.grid()
plt.legend()
plt.title('Excitation and Diffraction phases')
if save_plot:
    plt.savefig(save_dir + "\ExcitationComponents.svg", format='svg')
plt.show()
```

## D.2 Synchronization

```
def find_start(timeseries, tolerance, hz):

    N = len(timeseries)
    list = np.zeros(3 * hz)

    for i in range(3 * hz):
        list[i] = timeseries[i]

    timeseries = timeseries - np.mean(list)

    for i in range(N):
        if timeseries[i] < -tolerance:
            shift = np.where(timeseries == timeseries[i])[0][0]
            break
        else:
            continue

    return shift

def getShift_KC(KC, T, hz, N_ramp, N_steady, N_wait):
    time_shift = (2 * N_ramp + N_steady + N_wait) * T
    shift_step = time_shift * hz
    shift = shift_step * (KC - 1)

    return shift

def getShift_L2(timeseries1, timeseries2, hz):
    L2_norm = np.zeros(hz)
```

```
L2_list = []

timeseries1 = timeseries1 - np.mean(timeseries1)
timeseries2 = timeseries2 - np.mean(timeseries2)

for j in range(hz):
    for i in range(hz):
        L2_norm[i] = (timeseries1[int(5*hz+i)] -
            ↪ timeseries2[int(5*hz-0.2*hz+i+j)]) ** 2
        L2_list.append(sum(np.sqrt(L2_norm)))

shift = L2_list.index(min(L2_list)) - 0.2 * hz

return shift
```

### D.3 Experimental Sub-routines

```
def Forward_Euler(start, rate, step):
    result = np.zeros(len(rate))
    result[0] = start

    for i in range(len(rate) - 1):
        result[i + 1] = result[i] + rate[i] * step

    return result

def regular_wave(period, wave_height):
    f = 1/period
    omega = (2 * np.pi)/period
    k = omega ** 2/9.81
    wave_length = (2*np.pi)/k
    velocity_amplitude = omega * wave_height
    x_acceleration = omega ** 2 * wave_height
    z_acceleration = - omega ** 2 * wave_height
    return f, omega, k, wave_length, velocity_amplitude, x_acceleration,
    ↪ z_acceleration

def get_force(force, timeseries, step):
    numerator = np.zeros(len(force))
    denominator = np.zeros(len(timeseries))

    for i in range(len(numerator)):
        numerator[i] = force[i] * timeseries[i] * step
        denominator[i] = timeseries[i] * timeseries[i] * step

    result = - sum(numerator)/sum(denominator)

    return result
```

---

```

def Harmonics(timeseries, hz, T):
    dt = 1 / hz
    df = 1 / T
    frequencies = np.arange(1/T, 11/T, df)
    amplitudes = np.zeros(len(frequencies))
    bp_list = []

    for i in range(len(frequencies)):
        bp_series, _ = bpass_gaussian(timeseries, dt, frequencies[i] -
        ↪ 0.1*df, frequencies[i] + 0.1*df)
        _, maxima = sp.find_peaks(bp_series, height=0)
        _, minima = sp.find_peaks(-bp_series, height=0)

        avg_maxima = np.sum(maxima["peak_heights"]) /
        ↪ len(maxima["peak_heights"])
        avg_minima = - np.sum(minima["peak_heights"]) /
        ↪ len(minima["peak_heights"])
        amplitudes[i] = (avg_maxima - avg_minima) / 2
        bp_list.append(bp_series)

    return amplitudes, frequencies, bp_list

def AccCos2VelSine_timeseries(acc_amp, omega_amp, T, Nperiods, hz, iplot):

    timeseries = np.linspace(0, T * Nperiods, num=Nperiods*hz,
    ↪ endpoint=True)
    acc_series = np.zeros(len(timeseries))
    vel_series = np.zeros(len(timeseries))
    omega = (2 * math.pi) / T

    for i in range(len(timeseries)):
        acc_series[i] = acc_amp * np.cos(omega_amp * omega *
        ↪ timeseries[i])
        vel_series[i] = acc_amp * np.sin(omega_amp * omega *
        ↪ timeseries[i]) / (omega_amp * omega)

    if iplot:
        plt.plot(timeseries, acc_series, label='Acceleration')
        plt.plot(timeseries, vel_series, label='Velocity')
        plt.xlabel('Time [s]')
        plt.ylabel(r'\frac{m}{s^2}, \frac{m}{s}')
        plt.grid()
        plt.legend()
        plt.show()

    return acc_series, vel_series

```

## D.4 Analyze Script for Tandem Arrangement

```

import scipy.io as sio

n = 9          # Case number
KC_list = []   # Desired KC numbers
hz = 200      # Sampling frequency
dt = 1 / hz   # Sampling time step
T = 1.0       # Oscillation period
D = 0.05      # Cylinder diameter
rho = 1000    # Water density

# =====HardCode===== #

mat_files = ["Names of the .mat files, for post-processing"]

small_string = r' $(L / D = 1)$'
medium_string = r' $(L / D = 2)$'
large_string = r' $(L / D = 3)$'

Case_names = ["Names of the .mat files, for plot naming"]

WADAM_cases = ["Names of the .LIS files from Wadam"]

savepath = r"Insert save path for figures"
parent = r"Insert path to Wadam .lis files"
path = parent + WADAM_cases[n] + WADAM_cases[0]
save_dir = parent + WADAM_cases[n]
_, _, _, _, _, _, Ca_wadam, _, _, _, _, _ = get_data_WADAM(path, 0)

length = [0,
          D, 2 * D, 3 * D,
          D, 2 * D, 3 * D,
          D, 2 * D, 3 * D,
          D, 2 * D, 3 * D,
          D, 2 * D, 3 * D,
          D, 2 * D, 3 * D,
          D, 2 * D, 3 * D,
          D, 2 * D, 3 * D]

masses = [0,
          0.69, 1.39, 2.08,
          0.69, 1.39, 2.08,
          1.38, 2.78, 4.16,
          0.69, 1.39, 2.08,
          0.69, 1.39, 2.08,
          0.69, 1.39, 2.08,
          1.38, 2.78, 4.16]

# Lists for Harmonic force components outer/inner cylinder
outer_omegas = [[], [], [], []]
inner_omegas = [[], [], [], []]

```



```

outer_omegas_lift = [[], [], [], []]
inner_omegas_lift = [[], [], [], []]

# Lists for Harmonic force components difference force
delta_omegas = [[], [], [], []]
delta_omegas_lift = [[], [], [], []]

massForce_outer = [[], [], [], []]
dragForce_outer = [[], [], [], []]
massForce_inner = [[], [], [], []]
dragForce_inner = [[], [], [], []]
massForce_outer_lift = [[], [], [], []]
dragForce_outer_lift = [[], [], [], []]
massForce_inner_lift = [[], [], [], []]
dragForce_inner_lift = [[], [], [], []]
mass_coefficients_outer = [[], [], [], []]
drag_coefficients_outer = [[], [], [], []]
mass_coefficients_inner = [[], [], [], []]
drag_coefficients_inner = [[], [], [], []]

# =====ReadData===== #

# Read .mat files
mat0 = sio.loadmat('.\out' + mat_files[0])
mat = sio.loadmat('.\out' + mat_files[n])

# Import data from empty rig - 0 denotes empty rig
Pos_Rig_0 = mat0['Pos_Rig'].flatten()
Acceleration_0 = mat0['ACC_Z_BOTTOM_20497'].flatten()
FZ_OUTER_CALC_0 = mat0['FZ_OUTER_CALC'].flatten()
FZ_INNER_CALC_0 = mat0['FZ_INNER_CALC'].flatten()
FX_OUTER_CALC_0 = mat0['FX_OUTER_CALC'].flatten()
FX_INNER_CALC_0 = mat0['FX_INNER_CALC'].flatten()
FY_OUTER_CALC_0 = mat0['FY_OUTER_CALC'].flatten()
FY_INNER_CALC_0 = mat0['FY_INNER_CALC'].flatten()
t0 = mat0['Time 1 - default sample rate'].flatten()

# Import data from Case n
Pos_Rig = mat['Pos_Rig'].flatten()
Acceleration_n = mat['ACC_Z_BOTTOM_20497'].flatten()
FZ_OUTER_CALC = mat['FZ_OUTER_CALC'].flatten()
FZ_INNER_CALC = mat['FZ_INNER_CALC'].flatten()
FX_OUTER_CALC = mat['FX_OUTER_CALC'].flatten()
FX_INNER_CALC = mat['FX_INNER_CALC'].flatten()
FY_OUTER_CALC = mat['FY_OUTER_CALC'].flatten()
FY_INNER_CALC = mat['FY_INNER_CALC'].flatten()
t = mat['Time 1 - default sample rate'].flatten()

nondim = rho * length[n] * D ** 3 / T ** 2 # Force normalizing
start_amplitude = 0.05/(2*math.pi) # Start time criteria
A0 = rho * (math.pi / 4) * D ** 2 * length[n] # Reference factor

```

---

```

omega = (2 * math.pi) / T                                     # Radial frequency

# =====PreSync===== #

# Start synchronization
start_shift = find_start(Pos_Rig, 0.01 * start_amplitude, hz)
start_shift0 = find_start(Pos_Rig_0, 0.01 * start_amplitude, hz)

shift1 = start_shift + 87 * hz
shift0 = start_shift0 + 87 * hz

intervals = [[int(shift1 + 5 * T * hz), int(shift1 + 33 * T * hz)],
              [int(shift0 + 5 * T * hz), int(shift0 + 33 * T * hz)]]

# Initialize case - for easier reading in console
print("# ===== NewCase ===== #")
print("Case file:", mat_files[n])
print("start amplitude:", start_amplitude)
print("start index:", shift1)
print("start time:", shift1/hz)
print("start index 0:", shift0)
print("start time 0:", shift0/hz)

Pos1 = Pos_Rig[intervals[0][0]:intervals[0][1]]
Pos0 = Pos_Rig_0[intervals[1][0]:intervals[1][1]]
plotPostitions(Pos1, Pos0, 'First oscillation', 0)

# Iteration loop for selective KC numbers
for i in range(len(KC_list)):

    KC = KC_list[i]
    print("# ===== #")
    print("KC number:", KC)

    intervals = [[int(shift1 + 5 * T * hz), int(shift1 + 33 * T * hz)],
                  [int(shift0 + 5 * T * hz), int(shift0 + 33 * T * hz)]]

# =====Synchronize===== #

# Constructing the shift value for empty rig
KC_shift = getShift_KC(KC, T, hz, 150, 5, 5)
intervals[0][0] = intervals[0][0] + int(KC_shift)
intervals[0][1] = intervals[0][1] + int(KC_shift)
intervals[1][0] = intervals[1][0] + int(KC_shift)
intervals[1][1] = intervals[1][1] + int(KC_shift)

L2_shift = getShift_L2(Pos_Rig[intervals[0][0]:intervals[0][1]],
                       ↪ Pos_Rig_0[intervals[1][0]:intervals[1][1]], hz)
print("L2 shift:", L2_shift)
intervals[1][0] = intervals[1][0] + int(L2_shift)

```

---

```

intervals[1][1] = intervals[1][1] + int(L2_shift)

Pos1 = Pos_Rig[intervals[0][0]:intervals[0][1]]
Pos0 = Pos_Rig_0[intervals[1][0]:intervals[1][1]]

plotPostitions(Pos1, Pos0, 'Steady state position KC = %i' % KC, 0)

# =====IsolateForces===== #

# Subtract the rig
FZ_OUTER_raw = FZ_OUTER_CALC[intervals[0][0]:intervals[0][1]] -
↳ FZ_OUTER_CALC_0[intervals[1][0]:intervals[1][1]]
FZ_INNER_raw = FZ_INNER_CALC[intervals[0][0]:intervals[0][1]] -
↳ FZ_INNER_CALC_0[intervals[1][0]:intervals[1][1]]
FX_OUTER_raw = FX_OUTER_CALC[intervals[0][0]:intervals[0][1]] -
↳ FX_OUTER_CALC_0[intervals[1][0]:intervals[1][1]]
FX_INNER_raw = FX_INNER_CALC[intervals[0][0]:intervals[0][1]] -
↳ FX_INNER_CALC_0[intervals[1][0]:intervals[1][1]]
FY_OUTER_raw = FY_OUTER_CALC[intervals[0][0]:intervals[0][1]] -
↳ FY_OUTER_CALC_0[intervals[1][0]:intervals[1][1]]
FY_INNER_raw = FY_INNER_CALC[intervals[0][0]:intervals[0][1]] -
↳ FY_INNER_CALC_0[intervals[1][0]:intervals[1][1]]
Acc = Acceleration_n[intervals[0][0]:intervals[0][1]]

# Subtract the mass
FZ_OUTER_raw = FZ_OUTER_raw + masses[n] *
↳ Acceleration_n[intervals[0][0]:intervals[0][1]]
FZ_INNER_raw = FZ_INNER_raw + masses[n] *
↳ Acceleration_n[intervals[0][0]:intervals[0][1]]

delta_FZ_raw = FZ_INNER_raw - FZ_OUTER_raw
sum_FZ_raw = FZ_INNER_raw + FZ_OUTER_raw

delta_FY_raw = FY_INNER_raw - FY_OUTER_raw
sum_FY_raw = FY_INNER_raw + FY_OUTER_raw

# =====Filtration===== #

FZ_OUTER, _ = bpass_gaussian(FZ_OUTER_raw, dt, 0.8/T, 10/T)
FZ_INNER, _ = bpass_gaussian(FZ_INNER_raw, dt, 0.8/T, 10/T)
FX_OUTER, _ = bpass_gaussian(FX_OUTER_raw, dt, 0.8/T, 10/T)
FX_INNER, _ = bpass_gaussian(FX_INNER_raw, dt, 0.8/T, 10/T)
FY_OUTER, _ = bpass_gaussian(FY_OUTER_raw, dt, 0.8/T, 10/T)
FY_INNER, _ = bpass_gaussian(FY_INNER_raw, dt, 0.8/T, 10/T)
FZ_delta, _ = bpass_gaussian(delta_FZ_raw, dt, 0.8/T, 10/T)
FZ_sum, _ = bpass_gaussian(sum_FZ_raw, dt, 0.8/T, 10/T)
FY_delta, _ = bpass_gaussian(delta_FY_raw, dt, 0.8/T, 10/T)
FY_sum, _ = bpass_gaussian(sum_FY_raw, dt, 0.8/T, 10/T)
Acc_bpass, _ = bpass_gaussian(Acc, dt, 0.8 / T, 10 / T)

FZ_OUTER = FZ_OUTER / 2

```

```

FZ_INNER = FZ_INNER / 2
FX_OUTER = FX_OUTER / 2
FX_INNER = FX_INNER / 2
FY_OUTER = FY_OUTER / 2
FY_INNER = FY_INNER / 2
FZ_delta = FZ_delta / 2
FZ_sum = FZ_sum / 2
FY_delta = FY_delta / 2
FY_sum = FY_sum / 2

# =====Harmonics===== #

# Calculate harmonic force contributions
outer_amp, outer_omega, outer_BP_list = Harmonics(FZ_OUTER, hz, T)
inner_amp, inner_omega, inner_BP_list = Harmonics(FZ_INNER, hz, T)
delta_amp, delta_omega, delta_BP_list = Harmonics(FZ_delta, hz, T)
sum_amp, sum_omega, sum_BP_list = Harmonics(FZ_sum, hz, T)

outer_amp_lift, outer_omega_lift, outer_BP_list_lift =
↳ Harmonics(FY_OUTER, hz, T)
inner_amp_lift, inner_omega_lift, inner_BP_list_lift =
↳ Harmonics(FY_INNER, hz, T)
delta_amp_lift, delta_omega_lift, delta_BP_list_lift =
↳ Harmonics(FY_delta, hz, T)
sum_amp_lift, sum_omega_lift, sum_BP_list_lift = Harmonics(FY_sum, hz,
↳ T)
"""
plotFFT(FZ_OUTER, dt, 0, 10, 0)
plotFFT(FZ_INNER, dt, 0, 10, 0)
plotFFT(FY_OUTER, dt, 0, 10, 0)
plotFFT(FY_INNER, dt, 0, 10, 0)
"""

# Append harmonic forces to previous lists
outer_omegas[0].append(outer_amp[0])
outer_omegas[1].append(outer_amp[1])
outer_omegas[2].append(outer_amp[2])
outer_omegas[3].append(outer_amp[3])

inner_omegas[0].append(inner_amp[0])
inner_omegas[1].append(inner_amp[1])
inner_omegas[2].append(inner_amp[2])
inner_omegas[3].append(inner_amp[3])

delta_omegas[0].append(delta_amp[0])
delta_omegas[1].append(delta_amp[1])
delta_omegas[2].append(delta_amp[2])
delta_omegas[3].append(delta_amp[3])

outer_omegas_lift[0].append(outer_amp_lift[0])
outer_omegas_lift[1].append(outer_amp_lift[1])
outer_omegas_lift[2].append(outer_amp_lift[2])

```

```

outer_omegas_lift[3].append(outer_amp_lift[3])

inner_omegas_lift[0].append(inner_amp_lift[0])
inner_omegas_lift[1].append(inner_amp_lift[1])
inner_omegas_lift[2].append(inner_amp_lift[2])
inner_omegas_lift[3].append(inner_amp_lift[3])

delta_omegas_lift[0].append(delta_amp_lift[0])
delta_omegas_lift[1].append(delta_amp_lift[1])
delta_omegas_lift[2].append(delta_amp_lift[2])
delta_omegas_lift[3].append(delta_amp_lift[3])

# =====Velocity===== #

Acc_vec = Acc_bpass[0:int(T * hz)]
Acc_shift = np.where(Acc_vec == max(Acc_vec))[0][0]

# Acceleration intervals for force calculation - MUST be a whole
#   ↪ number of periods
Acc_intervals = [[int(Acc_shift), int(Acc_shift + 5 * T * hz)],
                 [int(Acc_shift), int(Acc_shift + 5 * T * hz)]]

Acceleration = Acc_bpass[Acc_intervals[0][0]:Acc_intervals[0][1]]
Velocity = Forward_Euler(0, Acceleration, dt)

FZ_AVF_OUTER = FZ_OUTER[round(Acc_shift):round(Acc_shift + 5 * T *
#   ↪ hz)]
FZ_AVF_INNER = FZ_INNER[round(Acc_shift):round(Acc_shift + 5 * T *
#   ↪ hz)]

# =====MassDrag===== #

for i in range(len(mass_coefficients_outer)):
    if i == 0:
        acc = Acceleration
        velocity = Forward_Euler(0, Acceleration, dt)
    else:
        acc, velocity = AccCos2VelSine_timeseries(1, i + 1, T, 5, hz,
#   ↪ 0)

    force_FZ_outer = outer_BP_list[i][round(Acc_shift):round(Acc_shift
#   ↪ + 5 * T * hz)]
    force_FZ_inner = inner_BP_list[i][round(Acc_shift):round(Acc_shift
#   ↪ + 5 * T * hz)]
    force_FZ_outer_lift =
#   ↪ outer_BP_list_lift[i][round(Acc_shift):round(Acc_shift + 5 * T
#   ↪ * hz)]
    force_FZ_inner_lift =
#   ↪ inner_BP_list_lift[i][round(Acc_shift):round(Acc_shift + 5 * T
#   ↪ * hz)]
    mass_force_outer = get_force(force_FZ_outer, acc, dt)

```

```

mass_force_inner = get_force(force_FZ_inner, acc, dt)
drag_force_outer = get_force(force_FZ_outer, velocity, dt)
drag_force_inner = get_force(force_FZ_inner, velocity, dt)
mass_force_outer_lift = get_force(force_FZ_outer_lift, acc, dt)
mass_force_inner_lift = get_force(force_FZ_inner_lift, acc, dt)
drag_force_outer_lift = get_force(force_FZ_outer_lift, velocity,
    ↪ dt)
drag_force_inner_lift = get_force(force_FZ_inner_lift, velocity,
    ↪ dt)

mass_coefficient_outer = mass_force_outer / A0
mass_coefficient_inner = mass_force_inner / A0
drag_coefficient_outer = drag_force_outer / (omega * A0)
drag_coefficient_inner = drag_force_inner / (omega * A0)

massForce_outer[i].append(mass_force_outer * ((2 * math.pi * KC *
    ↪ D) / T**2))
massForce_inner[i].append(mass_force_inner * ((2 * math.pi * KC *
    ↪ D) / T**2))
dragForce_outer[i].append(drag_force_outer * ((KC * D) / T))
dragForce_inner[i].append(drag_force_inner * ((KC * D) / T))
massForce_outer_lift[i].append(mass_force_outer_lift * ((2 *
    ↪ math.pi * KC * D) / T**2))
massForce_inner_lift[i].append(mass_force_inner_lift * ((2 *
    ↪ math.pi * KC * D) / T**2))
dragForce_outer_lift[i].append(drag_force_outer_lift * ((KC * D) /
    ↪ T))
dragForce_inner_lift[i].append(drag_force_inner_lift * ((KC * D) /
    ↪ T))
mass_coefficients_outer[i].append(mass_coefficient_outer)
mass_coefficients_inner[i].append(mass_coefficient_inner)
drag_coefficients_outer[i].append(drag_coefficient_outer)
drag_coefficients_inner[i].append(drag_coefficient_inner)

```

## D.5 Analyze Script for Staggered Arrangement

```

import scipy.io as sio
import scipy.fftpack
import re

n = 9                # Case number
KC_list = []        # Desired KC numbers
hz = 200            # Sampling frequency
dt = 1 / hz         # Sampling time step
T = 1.0             # Oscillation period
D = 0.05           # Cylinder diameter
rho = 1000          # Water density

```

```

iplot = 1

# =====HardCode===== #

mat_files = ["Names of the .mat files, for post-processing"]

data = ["lengths"], ["masses"], ["plot names"] # Aiding data
A0 = rho * (math.pi / 4) * D ** 2 * data[0][n] # Reference factor
omega = (2 * math.pi) / T # Radial frequency

# Lists for Harmonic force components outer/inner cylinder
IL_outer_omegas = [[], [], [], []]
IL_inner_omegas = [[], [], [], []]

CF_outer_omegas = [[], [], [], []]
CF_inner_omegas = [[], [], [], []]

delta_CF_omegas = [[], [], [], []]
delta_IL_omegas = [[], [], [], []]

viscous_IL_outer = [[], [], [], []]
viscous_CF_outer = [[], [], [], []]
viscous_IL_inner = [[], [], [], []]
viscous_CF_inner = [[], [], [], []]

inertial_IL_outer = [[], [], [], []]
inertial_CF_outer = [[], [], [], []]
inertial_IL_inner = [[], [], [], []]
inertial_CF_inner = [[], [], [], []]

thetas = []

print(mat_files[n])
print("length:", data[0][n])
print("mass:", data[1][n])

for i in range(len(KC_list)):

    KC = KC_list[i]
    print("# ===== #")
    print("KC number:", KC)

    for j in range(len(mat_files[n])):

        print("Case:", mat_files[n][j])

# =====ReadData===== #

theta = int(re.findall(r'\d+', mat_files[n][j])[0])
thetas.append(theta*(math.pi/180))

```

---

```

# Read .mat files
mat0 = sio.loadmat('.\out' + mat_files[0][0])
mat = sio.loadmat('.\out' + mat_files[n][j])

# Import data from empty rig - 0 denotes empty rig
Pos_Rig_0 = mat0['6047 Position'].flatten()
Acceleration_0 = mat0['Acc_20497'].flatten()
FZ_OUTER_CALC_0 = mat0['FZ_CALC_OUT'].flatten()
FZ_INNER_CALC_0 = mat0['FZ_CALC_IN'].flatten()
FX_OUTER_CALC_0 = mat0['FX_CALC_OUT'].flatten()
FX_INNER_CALC_0 = mat0['FX_CALC_IN'].flatten()
FY_OUTER_CALC_0 = mat0['FY_CALC_OUT'].flatten()
FY_INNER_CALC_0 = mat0['FY_CALC_IN'].flatten()
t0 = mat0['Time 1 - default sample rate'].flatten()

# Import data from Case n
Pos_Rig = mat['6047 Position'].flatten()
Acceleration_n = mat['Acc_20497'].flatten()
FZ_OUTER_CALC = mat['FZ_CALC_OUT'].flatten()
FZ_INNER_CALC = mat['FZ_CALC_IN'].flatten()
FX_OUTER_CALC = mat['FX_CALC_OUT'].flatten()
FX_INNER_CALC = mat['FX_CALC_IN'].flatten()
FY_OUTER_CALC = mat['FY_CALC_OUT'].flatten()
FY_INNER_CALC = mat['FY_CALC_IN'].flatten()
t = mat['Time 1 - default sample rate'].flatten()

nondim = rho * data[0][n] * D ** 3 / T ** 2
start_amplitude = 0.05/(2*math.pi)

# =====Synchronize===== #

# Start synchronization
start_shift = find_start(Pos_Rig, 0.01 * start_amplitude, hz)
start_shift0 = find_start(Pos_Rig_0, 0.01 * start_amplitude, hz)

intervals = [[int(start_shift + 5 * T * hz), int(start_shift + 33
↪ * T * hz)],
              [int(start_shift0 + 5 * T * hz), int(start_shift0 +
↪ 33 * T * hz)]]

# Constructing the shift value for empty rig
KC_shift = getShift_KC(KC, T, hz, 4, 30, 30)
intervals[0][0] = intervals[0][0] + int(KC_shift)
intervals[0][1] = intervals[0][1] + int(KC_shift)
intervals[1][0] = intervals[1][0] + int(KC_shift)
intervals[1][1] = intervals[1][1] + int(KC_shift)

L2_shift = getShift_L2(Pos_Rig[intervals[0][0]:intervals[0][1]],
↪ Pos_Rig_0[intervals[1][0]:intervals[1][1]], hz)

intervals[1][0] = intervals[1][0] + int(L2_shift)

```

---



```

intervals[1][1] = intervals[1][1] + int(L2_shift)

mean = np.mean(Pos_Rig[intervals[0][0]:intervals[0][1]])
mean0 = np.mean(Pos_Rig_0[intervals[1][0]:intervals[1][1]])

Pos1 = Pos_Rig[intervals[0][0]:intervals[0][1]]
Pos0 = Pos_Rig_0[intervals[1][0]:intervals[1][1]]
plotPositions(Pos1, Pos0, 'Steady state position KC = %i' % KC,
↳ 0)

# =====IsolateForces=====
↳ #

# Subtract the rig
FZ_OUTER_raw = FZ_OUTER_CALC[intervals[0][0]:intervals[0][1]] -
↳ FZ_OUTER_CALC_0[intervals[1][0]:intervals[1][1]]
FZ_INNER_raw = FZ_INNER_CALC[intervals[0][0]:intervals[0][1]] -
↳ FZ_INNER_CALC_0[intervals[1][0]:intervals[1][1]]
FX_OUTER_raw = FX_OUTER_CALC[intervals[0][0]:intervals[0][1]] -
↳ FX_OUTER_CALC_0[intervals[1][0]:intervals[1][1]]
FX_INNER_raw = FX_INNER_CALC[intervals[0][0]:intervals[0][1]] -
↳ FX_INNER_CALC_0[intervals[1][0]:intervals[1][1]]
FY_OUTER_raw = FY_OUTER_CALC[intervals[0][0]:intervals[0][1]] -
↳ FY_OUTER_CALC_0[intervals[1][0]:intervals[1][1]]
FY_INNER_raw = FY_INNER_CALC[intervals[0][0]:intervals[0][1]] -
↳ FY_INNER_CALC_0[intervals[1][0]:intervals[1][1]]
Acc = Acceleration_n[intervals[0][0]:intervals[0][1]]

# Subtract the mass
FZ_OUTER_raw = FZ_OUTER_raw + data[1][n] *
↳ Acceleration_n[intervals[0][0]:intervals[0][1]]
FZ_INNER_raw = FZ_INNER_raw + data[1][n] *
↳ Acceleration_n[intervals[0][0]:intervals[0][1]]

delta_IL_raw = FZ_INNER_raw - FZ_OUTER_raw
delta_CF_raw = FY_INNER_raw - FY_OUTER_raw
sum_FZ_raw = FZ_INNER_raw + FZ_OUTER_raw

# =====Filtration===== #

FZ_OUTER, _ = bpass_gaussian(FZ_OUTER_raw, dt, 0, 10)
FZ_INNER, _ = bpass_gaussian(FZ_INNER_raw, dt, 0, 10)
FX_OUTER, _ = bpass_gaussian(FX_OUTER_raw, dt, 0, 10)
FX_INNER, _ = bpass_gaussian(FX_INNER_raw, dt, 0, 10)
FY_OUTER, _ = bpass_gaussian(FY_OUTER_raw, dt, 0, 10)
FY_INNER, _ = bpass_gaussian(FY_INNER_raw, dt, 0, 10)
IL_delta, _ = bpass_gaussian(delta_IL_raw, dt, 0, 10)
CF_delta, _ = bpass_gaussian(delta_CF_raw, dt, 0, 10)
FZ_sum, _ = bpass_gaussian(sum_FZ_raw, dt, 0, 10)
Acc_bpass, _ = bpass_gaussian(Acc, dt, 0, 10)

```

```

FZ_OUTER = FZ_OUTER / 2
FZ_INNER = FZ_INNER / 2
FX_OUTER = FX_OUTER / 2
FX_INNER = FX_INNER / 2
FY_OUTER = FY_OUTER / 2
FY_INNER = FY_INNER / 2
IL_delta = IL_delta / 2
CF_delta = CF_delta / 2
FZ_sum = FZ_sum / 2

```

```
# =====Harmonics===== #
```

```
# Calculate harmonic force contributions
```

```

IL_outer_amp, IL_outer_omega, IL_outer_BP_list =
↳ Harmonics(FZ_OUTER, hz, T)
IL_inner_amp, IL_inner_omega, IL_inner_BP_list =
↳ Harmonics(FZ_INNER, hz, T)

```

```

CF_outer_amp, CF_outer_omega, CF_outer_BP_list =
↳ Harmonics(FY_OUTER, hz, T)
CF_inner_amp, CF_inner_omega, CF_inner_BP_list =
↳ Harmonics(FY_INNER, hz, T)

```

```

delta_IL_amp, delta_IL_omega, _ = Harmonics(IL_delta, hz, T)
delta_CF_amp, delta_CF_omega, _ = Harmonics(CF_delta, hz, T)

```

```

delta_CF_omegas[0].append(delta_CF_amp[0])
delta_CF_omegas[1].append(delta_CF_amp[1])
delta_CF_omegas[2].append(delta_CF_amp[2])
delta_CF_omegas[3].append(delta_CF_amp[3])

```

```

delta_IL_omegas[0].append(delta_IL_amp[0])
delta_IL_omegas[1].append(delta_IL_amp[1])
delta_IL_omegas[2].append(delta_IL_amp[2])
delta_IL_omegas[3].append(delta_IL_amp[3])

```

```

IL_outer_omegas[0].append(IL_outer_amp[0])
IL_outer_omegas[1].append(IL_outer_amp[1])
IL_outer_omegas[2].append(IL_outer_amp[2])
IL_outer_omegas[3].append(IL_outer_amp[3])

```

```

IL_inner_omegas[0].append(IL_inner_amp[0])
IL_inner_omegas[1].append(IL_inner_amp[1])
IL_inner_omegas[2].append(IL_inner_amp[2])
IL_inner_omegas[3].append(IL_inner_amp[3])

```

```

CF_outer_omegas[0].append(CF_outer_amp[0])
CF_outer_omegas[1].append(CF_outer_amp[1])
CF_outer_omegas[2].append(CF_outer_amp[2])
CF_outer_omegas[3].append(CF_outer_amp[3])

```

```

CF_inner_omegas[0].append(CF_inner_amp[0])
CF_inner_omegas[1].append(CF_inner_amp[1])
CF_inner_omegas[2].append(CF_inner_amp[2])
CF_inner_omegas[3].append(CF_inner_amp[3])

# =====Velocity===== #

Acc_vec = Acc_bpass[0:int(T * hz)]
Acc_shift = np.where(Acc_vec == max(Acc_vec))[0][0]

# Acceleration intervals for force calculation - MUST be a whole
↪ number of periods
Acc_intervals = [[int(Acc_shift), int(Acc_shift + 5 * T * hz)],
                 [int(Acc_shift), int(Acc_shift + 5 * T * hz)]]

Acceleration = Acc_bpass[Acc_intervals[0][0]:Acc_intervals[0][1]]
Velocity = Forward_Euler(0, Acceleration, dt)

FZ_AVF_OUTER = FZ_OUTER[round(Acc_shift):round(Acc_shift + 5 * T *
↪ hz)]
FZ_AVF_INNER = FZ_INNER[round(Acc_shift):round(Acc_shift + 5 * T *
↪ hz)]
FY_AVF_OUTER = FY_OUTER[round(Acc_shift):round(Acc_shift + 5 * T *
↪ hz)]
FY_AVF_INNER = FY_INNER[round(Acc_shift):round(Acc_shift + 5 * T *
↪ hz)]

plotAVF(Acceleration, Velocity, FZ_AVF_OUTER, FZ_AVF_INNER, KC, 0)
plotAVF(Acceleration, Velocity, FY_AVF_OUTER, FY_AVF_INNER, KC, 0)

# =====Velocity===== #

for i in range(len(viscous_IL_outer)):
    if i == 0:
        acc = Acceleration
        velocity = Forward_Euler(0, Acceleration, dt)
    else:
        acc, velocity = AccCos2VelSine_timeseries(1, i + 1, T, 5,
↪ hz, 0)

    force_IL_outer =
↪ IL_outer_BP_list[i][round(Acc_shift):round(Acc_shift + 5 *
↪ T * hz)]
    force_IL_inner =
↪ IL_inner_BP_list[i][round(Acc_shift):round(Acc_shift + 5 *
↪ T * hz)]
    force_CF_outer =
↪ CF_outer_BP_list[i][round(Acc_shift):round(Acc_shift + 5 *
↪ T * hz)]

```

```
force_CF_inner =  
    ↪ CF_inner_BP_list[i][round(Acc_shift):round(Acc_shift + 5 *  
    ↪ T * hz)]  
  
drag_CF_outer = get_force(force_CF_outer, velocity, dt)  
mass_CF_outer = get_force(force_CF_outer, acc, dt)  
mass_IL_outer = get_force(force_IL_outer, acc, dt)  
drag_IL_outer = get_force(force_IL_outer, velocity, dt)  
  
drag_CF_inner = get_force(force_CF_inner, velocity, dt)  
mass_CF_inner = get_force(force_CF_inner, acc, dt)  
mass_IL_inner = get_force(force_IL_inner, acc, dt)  
drag_IL_inner = get_force(force_IL_inner, velocity, dt)  
  
viscous_IL_inner[i].append(drag_IL_inner * ((KC * D) / T))  
viscous_CF_inner[i].append(drag_CF_inner * ((KC * D) / T))  
inertial_IL_inner[i].append(mass_IL_inner * ((2 * math.pi * KC  
    ↪ * D) / T**2))  
inertial_CF_inner[i].append(mass_CF_inner * ((2 * math.pi * KC  
    ↪ * D) / T**2))  
  
viscous_IL_outer[i].append(drag_IL_outer * ((KC * D) / T))  
viscous_CF_outer[i].append(drag_CF_outer * ((KC * D) / T))  
inertial_IL_outer[i].append(mass_IL_outer * ((2 * math.pi * KC  
    ↪ * D) / T**2))  
inertial_CF_outer[i].append(mass_CF_outer * ((2 * math.pi * KC  
    ↪ * D) / T**2))
```



 **NTNU**

Norwegian University of  
Science and Technology